Progress of Polymer Materials in Mining and Petroleum Engineering

Lead Guest Editor: Hetang Wang
Guest Editors: Taraknath Mandal, Shengyong Hu, Zhen Li, and Ruiyu Jiang
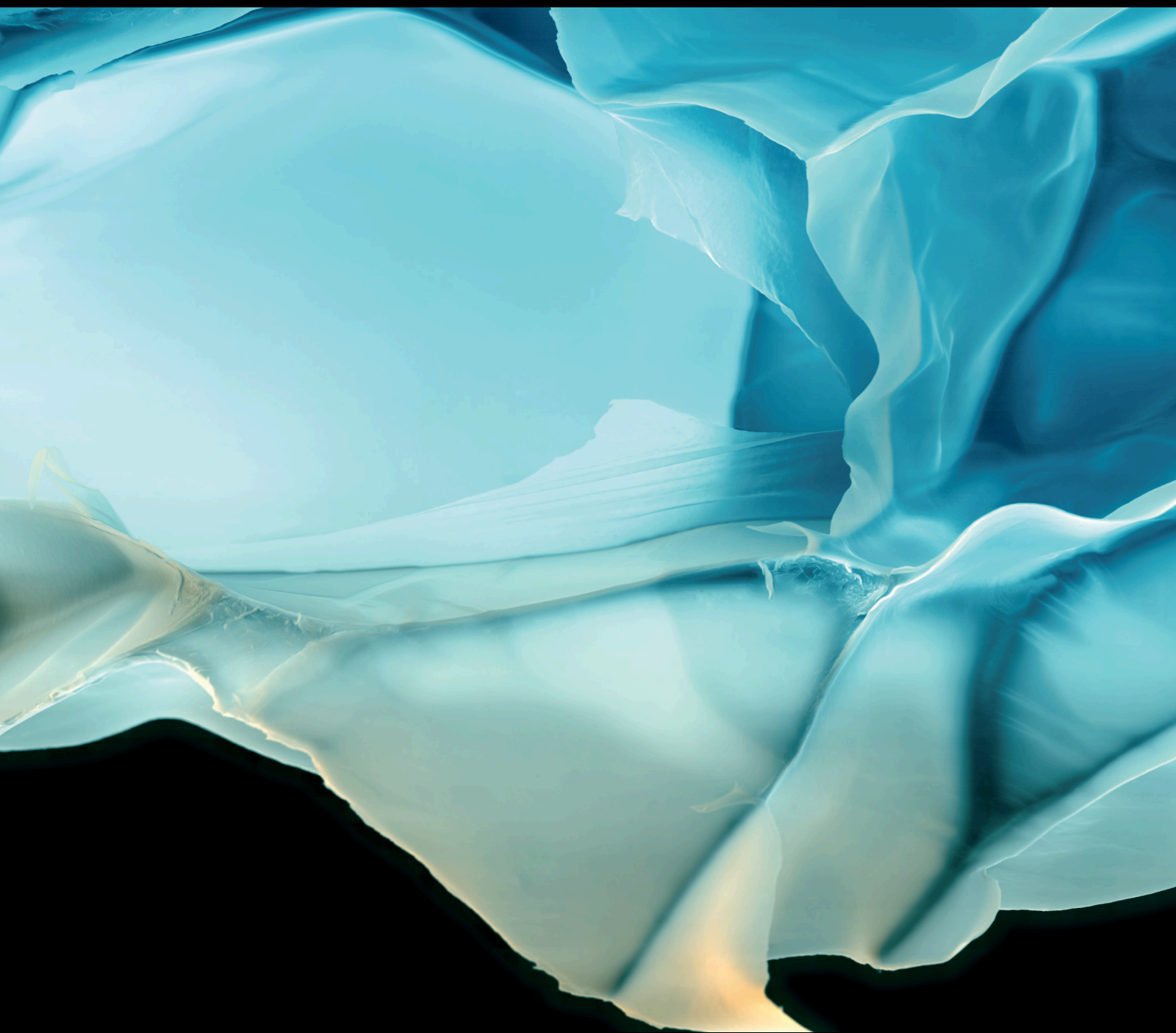
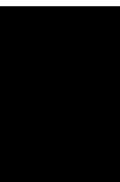# Progress of Polymer Materials in Mining and Petroleum Engineering

Progress of Polymer Materials in Mining and Petroleum Engineering

Lead Guest Editor: Hetang Wang
Guest Editors: Taraknath Mandal, Shengyong Hu, Zhen Li, and Ruiyu Jiang

Editorial Board

Contents

WILEY | Hindawi

Editorial

Progress of Polymer Materials in Mining and Petroleum Engineering

Hetang Wang [iD],[1] **Shengyong Hu,**[2] **and Ruiyu Jiang** [iD][3]

[1]School of Safety Engineering, China University of Mining and Technology, Xuzhou 221116, China
[2]College of Safety and Emergency Management Engineering, Taiyuan University of Technology, Taiyuan 030024, China
[3]School of Chemistry and Chemical Engineering, Yancheng Institute of Technology, Yancheng 224051, China

Correspondence should be addressed to Hetang Wang; wanghetang@cumt.edu.cn

Polymer materials are widely used in mining and petroleum engineering, which play an important role in mine and oilfield production. Due to the availability of a variety of polymeric materials, many parameters, such as molecular structure and molecular weight, have substantial effects on their properties. The design and selection of suitable polymers based on the intended specific applications can be challenging. The research into polymeric materials has attracted considerable interest from scientists and engineers in the fields of mining and petroleum. Studies focusing on polymer materials have a wide range of interest and applications in the mining and petroleum industries. This special issue aims to present recent research progress, developments, and applications of polymer materials and technology within mining and petroleum engineering, including theoretical studies, experimental investigations, and research into polymeric applications.

The paper by X. Liu et al. investigated the effect of temperature and accelerator on gel time and compressive strength of the resin anchoring agent. With increasing ambient temperature, the gelation time of the anchorage agent decreased. The peak exothermic value of the anchoring agent grew with the increasing ambient temperature. The compressive strength of resin anchoring agent dropped significantly with the increase in temperature.

K. Gao et al. established a cable combustion experiment platform to study the regularities of the cable fire spread speed and smoke temperature as well as the flame change and molten dripping behaviour. The flame-retardant cable can be ignited and continuously burnt at a certain wind speed, but combustion can be restrained at high wind speed. The combustion speed of the flame-retardant cable is affected by the fire load and ventilation speed. The combustion droplets can change the shape of the flame, which can consequently ignite other combustible materials.

The paper by J. Li et al. proposed that the average formation pressure and its location are changing all the time during alkali-surfactant-polymer (ASP) flooding. In addition, the influence of heterogeneity and viscosity on recovery and pressure is also probed in this paper. A numerical simulation model to match the experiment data considering the physical and chemical alternation in ASP flooding is also developed. Also, the response surface methodology (RSM) is adopted to obtain the formula between pressure functions and influencing factors.

W. Zou et al. investigated the adhesion and adsorption of a hydrophobically modified polyacrylamide (HMPAM) on silica and asphaltene using surface force measurements, thermodynamic analysis, and quartz crystal microbalance with dissipation (QCM-D) measurement. The adhesion force with an HMPAM-modified probe was greater on silica than on the asphaltene surface. Adsorption of HMPAM on the silica surface was greater than that on the asphaltene surface, and the adsorbed layer was more rigid on the silica surface. Hydrophobic interactions between the asphaltene surface and the long hydrocarbon chains of HMPAM may dominate the attraction and adhesion.

Y. Chen et al. proposed a flame retardant with bio-based benzoxazine (Boz-F), red phosphorus, and melamine with a mass ratio of $2:1:2$, which then underwent mechanical

modification by hollow glass bubbles. The pregrouting material with low viscosity and high permeability was compounded, and its interaction with coal was experimentally studied. The new material increases the effective consolidation distance in the coal seam by 40% on an average compared with traditional polyurethane. Its permeation radius is larger than the calculated radius of the plastic softening zone of a borehole. In addition, the strengths of coal-new material consolidated products with different ratios fully surpass those of coal-polyurethane material consolidated products.

The paper by C. Zhang et al. proposed a new solidified sealing material with better strain-bearing capacity and volumetric expansion capacity. The axial strain and volume increment of the new solidified material is higher than those of the traditional concrete solidified material at the peak stress. Meanwhile, the confining pressure has a certain hysteresis effect on the postpeak stress attenuation. The relative content of seepage pore and fracture in the new solidified material is less than that of coal and concrete samples, and the stress sensitivity of the new solidified materials is weaker than that of coal and concrete materials; hence, new solidified material will have better performance in borehole sealing.

Conflicts of Interest

The editors declare that they have no conflicts of interest regarding the publication of this special issue.

Acknowledgments

Hetang Wang
Shengyong Hu
Ruiyu Jiang

WILEY | Hindawi

Research Article

Study on the Interaction between Low-Viscosity High-Permeability Pregrouting Sealing Material and Coal and Its Application

Yujia Chen,[1,2,3] **Ao Li** (ID),[4,5] **Dingding Yang** (ID),[6] **Tianyu Liu,**[1,2,3] **Xiaowei Li** (ID),[1,2,3] **Jun Tang,**[1,2,3] **and Chenglin Jiang**[1,2,3]

[1]Key Laboratory of Gas and Fire Control for Coal Mines, Xuzhou 221116, Jiangsu, China
[2]National Engineering Research Center of Coal Gas Control, Xuzhou 221116, Jiangsu, China
[3]School of Safety Engineering, China University of Mining & Technology, Xuzhou 221116, Jiangsu, China
[4]College of Safety and Emergency Management Engineering, Taiyuan University of Technology, Taiyuan 030024, Shanxi, China
[5]Jiangsu Vocational Institute of Architectural Technology, Xuzhou 221000, Jiangsu, China
[6]School of Petrochemical and Energy Engineering, Zhejiang Ocean University, Zhoushan 316022, Zhejiang, China

Correspondence should be addressed to Ao Li; everliao@gmail.com

In order to ensure the intactness of pressure-measuring boreholes and the accuracy of gas pressure determination, pregrouting treatment with polymer materials is frequently applied to bedding drilling in coal mines. However, the existing polyurethane materials are of high viscosity, low permeability, and poor safety, bringing great difficulties to their field promotion and application. In view of this problem, after optimization and experiments, polylactide polyol/polyether polyol 4110/isocyanate was determined as the target system. Bio-based benzoxazine (Boz-F), red phosphorus, and melamine with a mass ratio of 2 : 1 : 2 were used as the flame retardant, which then underwent mechanical modification by hollow glass bubbles. Finally, the pregrouting material with low viscosity and high permeability was compounded, and its interaction with coal was experimentally studied. The results show that compared with traditional polyurethane, the new material increases the effective consolidation distance in the coal seam by 40% on average. Its permeation radius is also larger than the calculated radius of the plastic softening zone of a borehole. In addition, the strengths of coal-new material consolidated products with different ratios fully surpass those of coal-polyurethane material consolidated products. The enhancement of compressive strength and bending strength is up to 153% and 161%, respectively. The field application indicates that after pregrouting treatment of boreholes in the coal seam with the new material, the borehole formation rate reaches 100%. Therefore, the new material is safe and practical for gas pressure measurement through bedding drilling on site.

1. Introduction

With the development of national economy, more and more polymer materials have been applied to the coal industry [1–6]. As far as gas prevention and control is concerned, polymer materials are more and more frequently applied to mine gas pressure measurement. The utilization of polyurethane as a sealing material for bedding drilling during gas pressure measurement is a practical method developed in recent years. On the one hand, polyurethane materials can consolidate the loose coal layers around bedding boreholes

[7–10]. On the other hand, it can seal coal fractures [11–14], thus creating good conditions for the pressure measurement [15–17]. However, practical applications have revealed that the raw polyurethane material is of high viscosity and poor permeability into coal. If a high injection pressure is applied, it will migrate along cracks of a loose layer to a rather far place so that it cannot effectively reinforce the loose layer surrounding a borehole. In addition, it has poor safety performance characterized by problems such as high temperature in the consolidation process and poor flame retardancy. Mine fires caused by polymer materials occur

from time to time, which severely limits the application of polyurethane materials to mines. Hence, it is necessary to develop a new type of low-viscosity and high-permeability sealing material. First, the new material should feature low viscosity. That is, it should have better permeability than polyurethane materials under normal or lower pressures, because high permeability enables it to bond with coal in a large range to consolidate loose layers. Second, it should feature a suitable consolidation time for the material to be injected into the coal seam. Finally, it should boast good safety performance, namely low consolidation temperature and high flame-retardant grade, so as to guarantee its safe application to the coal industry. A new material with these characteristics can better permeate fractures in a coal seam, seal cracks, and bond the coal, thus meeting the practical need of gas pressure measurement through bedding drilling.

To achieve the aforesaid objectives, polylactide polyol/polyethylene/glycol 200/polyethylene glycol 600, polyether polyol 4110, and isocyanate were used as main raw materials to compound three kinds of composites. After optimization, polylactide polyol/polyether polyol 4110/isocyanate was determined to be the target system (basic formula). It was found that with the addition of polylactide polyol, the peak temperature of the new material in the consolidation process declined, and the consolidation time was prolonged. Without affecting foaming performance of the material, the optimal mass ratio of polylactide polyol : polyether polyol 4110 : isocyanate was finally determined to be 4 : 6 : 10 (i.e., 2 : 3 : 5). The basic formula was used for the subsequent research. Furthermore, an analysis was conducted on the low-temperature consolidation mechanism of the new material, pointing out the important effect of hydroxyl concentration on the consolidation process [18].

Based on the work, in view of poor flame retardancy of the new material, a new type of self-made charring agent, Boz-F, was adopted to compound an intumescent flame retardant for the experimental study on the new material. Thermogravimetric experiments, thermal degradation kinetics, and the differential scanning calorimetry (DSC) analysis indicate that Boz-F has a high charring rate and proper decomposition activation energy, and thus it is a suitable charring agent of the intumescent flame retardant. Through a vertical firing test, a thermogravimetric analysis, Raman spectral and X-ray diffraction spectral analyses, it is proven that the composite achieves the best flame retardancy when the mass ratio of charring agent : red phosphorus : melamine is 2 : 1 : 2. Besides, to avoid degradation of mechanical properties of the material induced by the application of intumescent flame retardant, hollow glass bubbles (HGB) were utilized for a mechanical modification experiment of the flame-retardant material. Related experiments show that the addition of HGB improves the compressive resistance and bending resistance of the new material [18].

After the above work, a green and safe sealing material with low viscosity and high permeability was developed for pressure measurement. Moreover, the interaction between the material and coal was experimentally studied to further investigate their interaction, the permeability of the material in coal, and the mechanical properties of coal-new material

consolidated product (CNMCP). Besides, the sealing effect of the new material was also compared and investigated on site.

2. Analysis of Stress Distribution of Coal around Bedding Drilling and the Failure Mechanism of Boreholes

2.1. Stress Distribution Model and Zone Division of the Borehole along the Drilling Direction. When a drill bit is drilling a borehole along a coal seam, it will cause damage to the original coal. Due to the drilling operation, strain stress will redistribute in the whole coal. In the direction of drilling, some areas experience stress concentration; some areas undergo pressure relief; and others suffer little drilling-induced disturbance and basically maintain the original stress distribution. According to changes in stress, coal along the drilling direction can be divided into three zones [19], namely, the stress unloading zone (the pressure relief zone), the stress concentration zone (the concentration zone), and the original stress zone (the primary zone).

After a borehole is formed in coal, the stress redistributes. The maximum and minimum principal stresses around the borehole are the tangential and radial stresses, respectively. Based on the state of stress around a borehole, the area along the diameter direction can be divided into three zones, namely, plastic softening zone, plastic hardening zone, and elastic zone (the former two are collectively referred to plastic failure zone), as shown in Figure 1.

Like stress distribution in coal along the drilling direction, coal in the plastic failure zone features fracture development and low strength. Specifically, the plastic hardening zone and the elastic zone share similar fracture development and stress state, and the permeability and stress state of the two zones can even be regarded as the same. In the plastic softening zone, coal is loosened and damaged, with fracture development. The zone is in the stage of complete plastic deformation. It is a primary area that needs to be solidified and sealed in engineering practices such as gas pressure measurement. In the elastic zone, stress and pores are in their original state, or the coal is compacted due to stress concentration. The porosity and permeability are low in this zone. Thereby, the minimum permeation distance of the plugging material should be greater than the radius of the plastic softening zone, for ensuring the effectiveness of plugging. Besides, the larger the permeation radius is, the better the plugging effect becomes.

According to the relevant literature, the range of plastic softening zone of drilled coal and rock mass can be determined by equation (1) [20]:

$$R_s = R_0 \left[\frac{2 \left[\sigma_0 \left(K_p - 1 \right) + \left(2c \cos \varphi / \left(1 - \sin \varphi \right) \right) \right]}{\left(K_p + 1 \right) \left(2c \cos \varphi / \left(1 - \sin \varphi \right) \right)} \right]^{1/\left(K_p - 1 \right)},$$

(1)

where R_s is the radius of the plastic softening zone, R_0 is the radius of the borehole, σ_0 is the original stress of the coal, ϕ is the internal friction angle of the coal, and $K_p = (1 + \sin \varphi) / (1 - \sin \varphi)$.
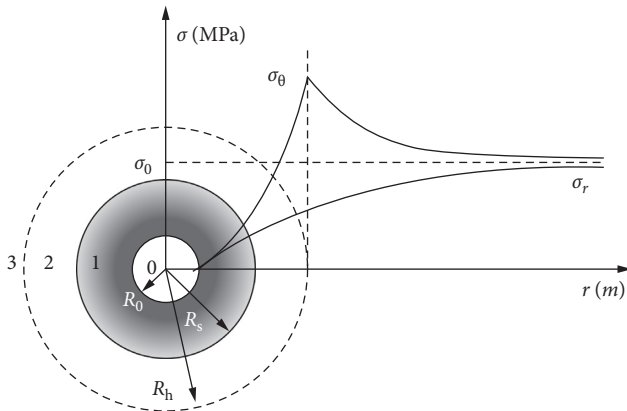
FIGURE 1: Stress distribution diagram of elastic-plastic zones of a borehole. R_0 is the radius of the borehole, R_s is the radius of the plastic softening zone, and R_h is the radius of the plastic hardening zone; 1 is the plastic softening zone, 2 is the plastic hardening zone, and 3 is the elastic zone.

2.2. Three Failure Modes of Bedding Drilling. The failure (instability) of bedding drilling is related to the structural failure of a bedding borehole itself and the stress state of surrounding coal. According to the failure (instability) areas, damage of a bedding borehole can be divided into two modes: (1) mechanical failure of the borehole structure and (2) the borehole structure instability and borehole collapse induced by the internal structural damage of coal around the borehole, which is frequently accompanied by jamming of drilling tools and spewing. The first mode can be subdivided into borehole-bottom failure (instability) and borehole-wall failure (instability), according to the failure location. Various modes, forms, and criteria for failure of bedding drilling are illustrated in Figure 2 [21–25].

After the new material is injected into a coal seam, it will exert an impact on the aforesaid three failure modes. For the sake of simplicity, studies are mainly conducted on the permeation and distribution of the material along the direction of borehole diameter. The new material, which permeates along the diameter direction, will change the mechanical properties of coal around the pore wall. Besides, it can interact with coal to form a coal-composite consolidated product with a certain strength, hence improving the mechanical properties of coal around the borehole wall and strengthening the coal seam.

The new material should permeate the plastic softening zone and bond well with coal to form a consolidated product, thereby reinforcing the plastic zone and achieving the purpose of sealing and strengthening. Hence, the permeability and consolidation effect of the plugging material need to be investigated.

3. Experimental Study on Permeability of the New Material in Coal

3.1. Experimental Study. The experiment was carried out via a simulation experimental device of coal seam outburst developed by China University of Mining and Technology. The device mainly consists of a press, an obround cylinder, a compression column, and a plug. It has the maximum test load of 10,000 kN. The obround has two semicircular ends with a radius of 110 mm and two parallel lines with a length of 900 mm. The depth of the cylinder is 330 mm. With the maximum test load, the formation pressure of a coal seam can reach 42.37 MPa, and the outburst coal such as Grade IV coal and Grade V coal can be prepared on site [26]. In the permeability experiment, coal samples from Wangzhuang Coal Mine were first crushed in the laboratory and then sieved to obtain coal particles with a size of below 1 mm. Next, an appropriate volume of water was added to the particles and the mixture was stirred evenly before they were sealed in a tank. To fully compact coal samples, the coal seam pressing was carried out five times. The thickness of a coal seam was about 45 mm each time. The coal seam was kept for 30 min under the formation pressure of 35 MPa to discharge gas from it, which was beneficial to the combination between samples.

After the layered pressing, the confining pressure was maintained at 10 MPa by the press for 12 h, in order to make properties of the briquette uniform and stable. Then, a pipe with a diameter of 42 mm driven by a coal electric drill drilled into the simulated coal seam from the plug side. After the formation of a borehole, sealing materials with the same mass (1 kg) were injected in them for a material permeability test. After the materials were solidified and molded for 12 h, superfluous coal was removed to obtain coal-material consolidated product. Next, 5 sections were cut from the consolidated material at an equal distance, and the maximum radial dimensions of sections were measured. According to the corresponding physical meaning, the difference between the maximum radial dimension and the borehole diameter (42 mm) is defined as the effective consolidation distance of the material into a coal seam, for investigating the permeability of the material. Specific steps are illustrated in Figure 3. Comparison of effective consolidation distances of two different materials after they permeate the coal seam is given in Table 1.

It can be observed from Table 1 that the effective consolidation distances of the new material are all larger than those of polyurethane. The maximum, minimum, and average values of the effective consolidation distance of the new material in the coal matrix are 33 mm, 27 mm, and 29.4 mm, respectively, while those of polyurethane are 22 mm, 20 mm, and 21 mm, respectively. The average value of the new material is 40.0% higher than that of polyurethane.

3.2. Investigation on Permeation Effect. In order to further quantify the permeability of the new material, relevant parameters of coal samples collected from Wangzhuang Coal Mine were combined with equation (1) to calculate the radius R_s of the plastic softening zone. In addition, half of the average of the maximum radial dimension of consolidated products was defined as the permeation radius of the material. The comparison between the permeation radii of materials and the radius of plastic softening zone is shown in Table 2.

Failure mode 1 → ① Borehole-bottom in the stress unloading zone (1) $\sigma_r + \alpha p_r \delta_{ij} \geq c + f$
② Borehole-bottom in the postpeak stress concentration zone (2) $\sigma_r + \alpha p_r \delta_{ij} \geq \sigma_s^x (\varepsilon_1^P)$
③ Borehole-bottom in the prepeak stress concentration zone (3) $\sigma_r + \alpha p_r \delta_{ij} \geq \sigma_t$

Failure mode 2 $\sigma_\theta \geq \sigma_c + \sigma_r (\sigma_c/\sigma_r)$ Mohr–Coulomb failure criterion

Failure mode 3 → ① Initial generation of critical cracks $\cos 2\beta = (1/2)[((\sigma_1 - \sigma_3)/(\sigma_1 + \sigma_3)) \times ((l + n)/(l - n)) - ((\sigma_1 + \sigma_3)/(\sigma_1 - \sigma_3)) \times ((4 \times l \times n)/(l^2 - n^2))]$
② Extension and connection of critical cracks $P - \sigma_r \geq K_{Ic}/(q\sqrt{r})$

FIGURE 2: Three failure modes of bedding drilling.
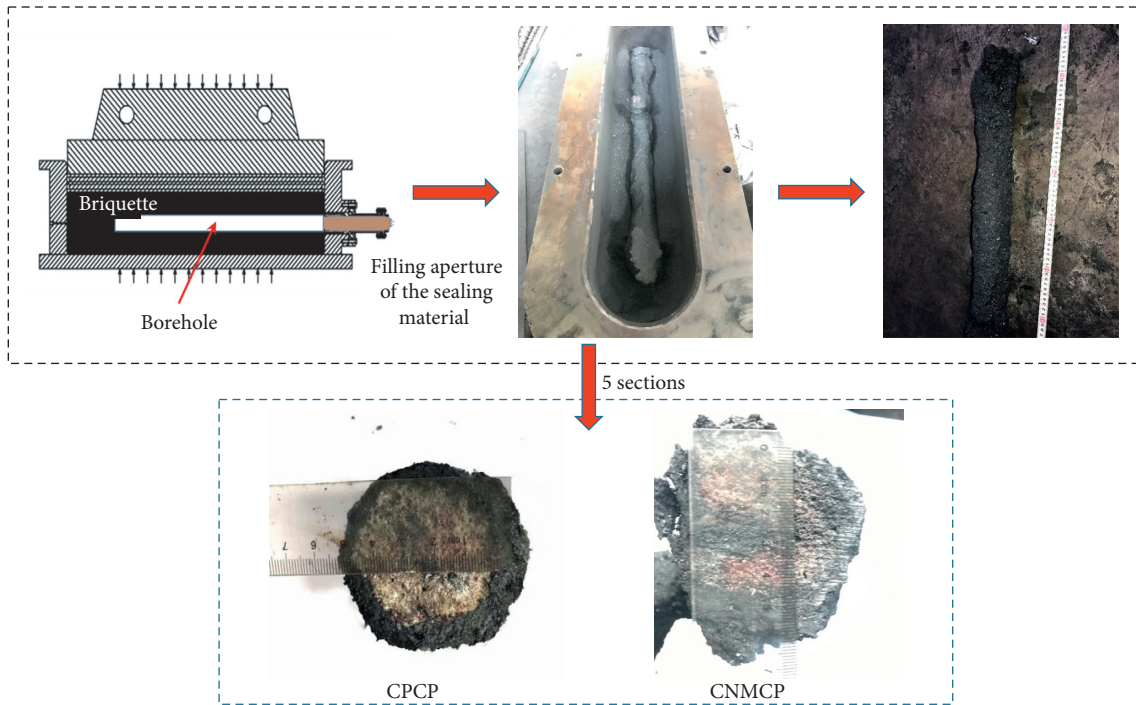
FIGURE 3: Schematic diagram of the experimental process of material permeability in coal.

TABLE 1: Comparison of effective consolidation distances of materials in coal.

Indexes	Material type	Section 1 (mm)	Section 2 (mm)	Section 3 (mm)	Section 4	Section 5 (mm)	Average (mm)
Effective consolidation distance	Polyurethane	22	21	22	20	20	21
	New material	29	27	30	28	33	29.4

TABLE 2: Comparison between the experimentally obtained permeation radii of materials and the calculated radius of plastic softening zone (A refers to polyurethane and B represents the new material).

Coal sample source	Borehole radius (mm)	Original stress (MPa)	Internal friction angle (°)	Cohesion (MPa)	Calculated value of R_s (mm)	Permeation radius of A (mm)	Permeation radius of B (mm)
Wangzhuang coal mine	21	10	28	1.4	35.6	31.5	35.7

Table 2 reflects that the experimentally obtained permeation radius of the new material is larger than the radius of the plastic softening zone. In other words, the new material can not only completely permeate the plastic softening zone to play a better role in sealing and bonding, but also effectively strengthen the broken coal. Besides, it has obvious better permeation effect in coal than polyurethane, a kind of traditional sealing material. Furthermore, it can consolidate loose coal in plastic softening zone, boasting good application effect on sealing fracture and

solidifying coal seams. Due to the limited experimental conditions, the injection was only performed under atmospheric pressure, while the pressed injection test was not carried out. If the injection had been performed under a low pressure, the permeation effect of the material could have been better.

4. Study on Mechanical Properties of Coal-Composite Consolidated Products

During gas pressure measurement through bedding drilling, a consolidated product will be formed by the injected material and the coal particles. Mechanical properties of the consolidated product, which directly affect the reinforcement and sealing effect of boreholes, are mainly reflected by the compressive strength and bending strength of sample. When the consolidated product is subjected to compressive and bending stresses, the greater the compressive and bending strengths are, the stronger the antideformation ability of borehole is, and thus the more integrated the borehole wall will be. Therefore, the study on mechanical properties of coal-composite consolidated products, especially the comparison of compressive and bending strengths between the coal-polyurethane consolidated product CPCP and the CNMCP, can facilitate the understanding of how to improve the performance of new material. In this section, a test was conducted on mechanical properties of the CPCP and the CNMCP. Experimental samples were prepared according to the formulation in Tables 3 and 4, respectively, to obtain two types of consolidated products. Then, test samples were cut by a press cutter, as displayed in Figure 4.

4.1. Experimental Material. Isocyanate is produced by Wanhua Chemical Group Co., Ltd., Yantai, Shandong Province. Polylactide polyol (including foaming agent) is made by Shenzhen Esun Industrial Co., Ltd. Boz-F, a new kind of charring agent, is self-made. Red phosphorus is manufactured by Guangdong Fantian Technology Co., Ltd. Melamine is provided by Sinopharm Chemical Reagent Co., Ltd. VS5500 HGB comes from the 3M Company (China). Pulverized coal is the broken coal with a diameter of 1 mm or less after screening, from Xinyuan Coal Mine, Shanxi province.

4.2. Experimental Material Preparation. The prepared samples of coal-composite consolidated products for the mechanical property test are shown in Figure 4.

4.3. Mechanical Property Test

4.3.1. Compression Test. Figure 5 demonstrates compressive stress-strain curves for six different formulations of CPCP at a loading speed of 1 mm/min.

It can be seen from curves in Figure 5 that when the consolidated product with the addition of pulverized coal is subjected to compressive stress, it shows complex compression fracture behaviors as the addition amount changes. In J-4, the curve exhibits certain characteristics of ductile

fracture. The CPCP yields without obvious fractures when the compressive stress reaches 4.5 MPa. Instead, its compressive stress decreases slightly with the increase of compressive strain. As compressive deformation reaches 0.38, compressive stress continues to grow to the maximum value of 4.64 MPa. At this point, the CPCP breaks. The CPCPs with the rest formulations have typical brittle fracture behaviors, that is, when the compressive stress they bear reaches the maximum, they will find the formation of obvious cracks and will be destroyed. As a kind of filler like inorganic particles, pulverized coal can mix with polyurethane to form a consolidated product. When the consolidated product is subjected to compressive stress, abundant crazes are induced in a direction perpendicular to the compressive stress. These crazes are a kind of viscoelastic medium with a certain mechanical strength, so they can induce the ductile fracture of the consolidated product. However, under the action of continuous external force, crazes will break and turns into cracks, which destroys the consolidated product. A small amount of pulverized coal can be uniformly mixed with polyurethane to produce few crazes, causing fracture damage to the composite when the overall material reaches the limit of compressive yield (J-5 and J-6). With a high content of pulverized coal (J-1, J-2, and J-3), mechanical properties of the overall composite degrade because of the incompatibility between pulverized coal and polyurethane and the poor strength of pulverized coal itself. Only with an appropriate volume of pulverized coal can crazes be generated (J-4), which enhances the compressive strength of the coal-polyurethane composite.

Figure 6 presents compressive stress-strain curves for six different formulations of CNMCP at a loading speed of 1 mm/min.

Different from CPCPs, all the CNMCPs are characterized by brittle fracture. In addition, except for some individual points, compressive strength of CNMCP rises from 4.36 MPa to 7.14 MPa, with the declining addition of pulverized coal and the growing content of the new material. When more pulverized coal and less new material are added, the consolidated product has low compressive resistance because it cannot be effectively reinforced by the insufficiently added new material and the low-strength pulverized coal. Instead, when less pulverized coal and more new material are added, HGB in the new material can effectively enhance the rigidity. As a result, the consolidated product possesses high compressive resistance and improved compressive strength.

Table 5 gives a comparison between compressive strengths of CPCP and CNMCP. On the premise of the same mass ratio, the CNMCP has a greater compressive strength than the CPCP. To quantitatively compare compressive strengths of the two, (the compressive strength of CPCP–the compressive strength of CNMCP)/the compressive strength of CPCP is defined as the percentage of enhancement. The result shows that compressive strength of CNMCP is 153% higher than that of CPCP. In other words, the new material interacts more strongly with coal and boasts better performance of permeating coal and bonding loose coal seam than traditional polyurethane.

TABLE 3: Composition of CPCP.

No.	Polyether polyol 4110 (g)	Isocyanate (g)	Catalyst (g)	Pulverized coal (g)
J-1	40	40	0.4	100
J-2	40	40	0.4	90
J-3	40	40	0.4	80
J-4	40	40	0.4	70
J-5	40	40	0.4	60
J-6	40	40	0.4	50

TABLE 4: Composition of CNMCP.

No.	Polylactide polyol (g)	Polyether polyol 4110 (g)	Isocyanate (g)	Charring agent (g)	Red phosphorus (g)	Melamine (g)	Catalyst (g)	HGB (g)	Pulverized coal (g)
X-1	16	24	40	8	4	8	0.4	12	100
X-2	16	24	40	8	4	8	0.4	12	90
X-3	16	24	40	8	4	8	0.4	12	80
X-4	16	24	40	8	4	8	0.4	12	70
X-5	16	24	40	8	4	8	0.4	12	60
X-6	16	24	40	8	4	8	0.4	12	50
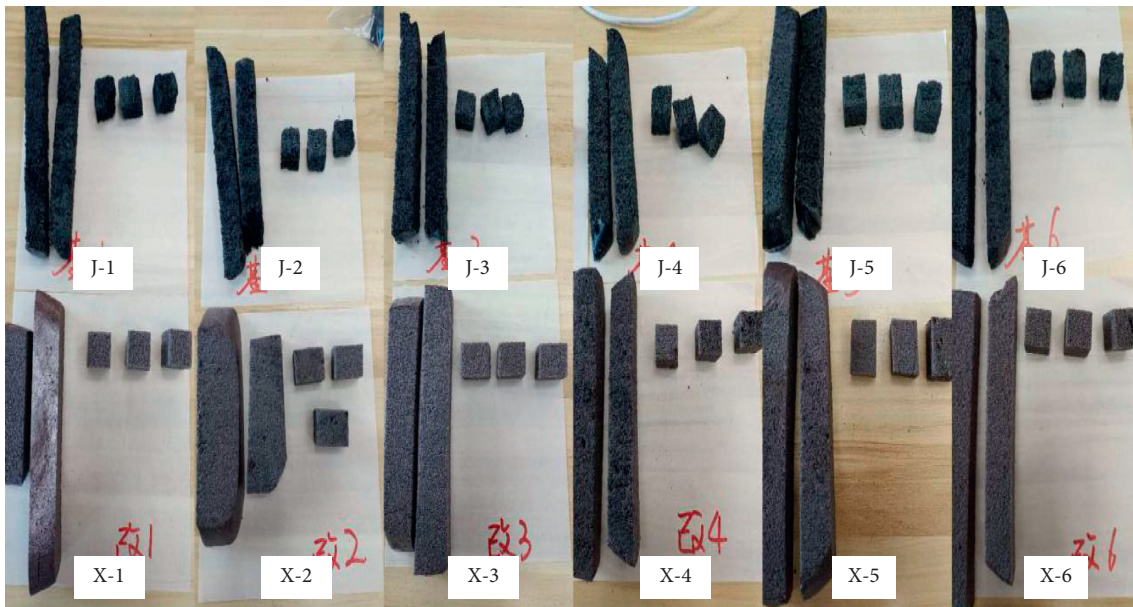
FIGURE 4: Samples of coal-composite consolidated products for the mechanical property test.

4.3.2. Bending Test. Bending stress-strain curves for six different formulations of CPCP at a loading speed of 1 mm/min are displayed in Figure 7.

After the addition of pulverized coal, all the CPCPs show obvious brittle fracture behaviors. An optimal ratio of pulverized coal to polyurethane exists for the improvement of bending performance. It is obvious that when a large amount of pulverized coal is added, both the bonding effect of polyurethane on pulverized coal and the strength of CPCP are weakened. This is because pulverized coal, which is not a kind of polymer material, shares no compatibility with polyurethane. The continuity of the organic system of polyurethane is destroyed with the addition of a great amount of pulverized coal. Besides, pulverized coal itself has low strength, thus lowering the bending performance of the whole composite. When a small amount of pulverized coal is

added, the prepared polyurethane, a kind of rigid foam material, will see the acceleration of destruction due to the breakage of cells under a bending force. When an intermediate optimal amount of pulverized coal is added, the added coal will effectively fill cells of rigid polyurethane foams, without causing damage to the continuous structure of cell walls of polyurethane. During the bending failure process, the coal will effectively absorb the shock of external load. As a result, the bending strength of composite reaches the maximum value.

Figure 8 illustrates bending stress-strain curves for six different formulations of CNMCP at a loading speed of 1 mm/min.

As can be seen from Figure 8, the addition of pulverized coal has a great influence on the brittle-ductile fracture behaviors of CNMCPs. As the addition of pulverized coal
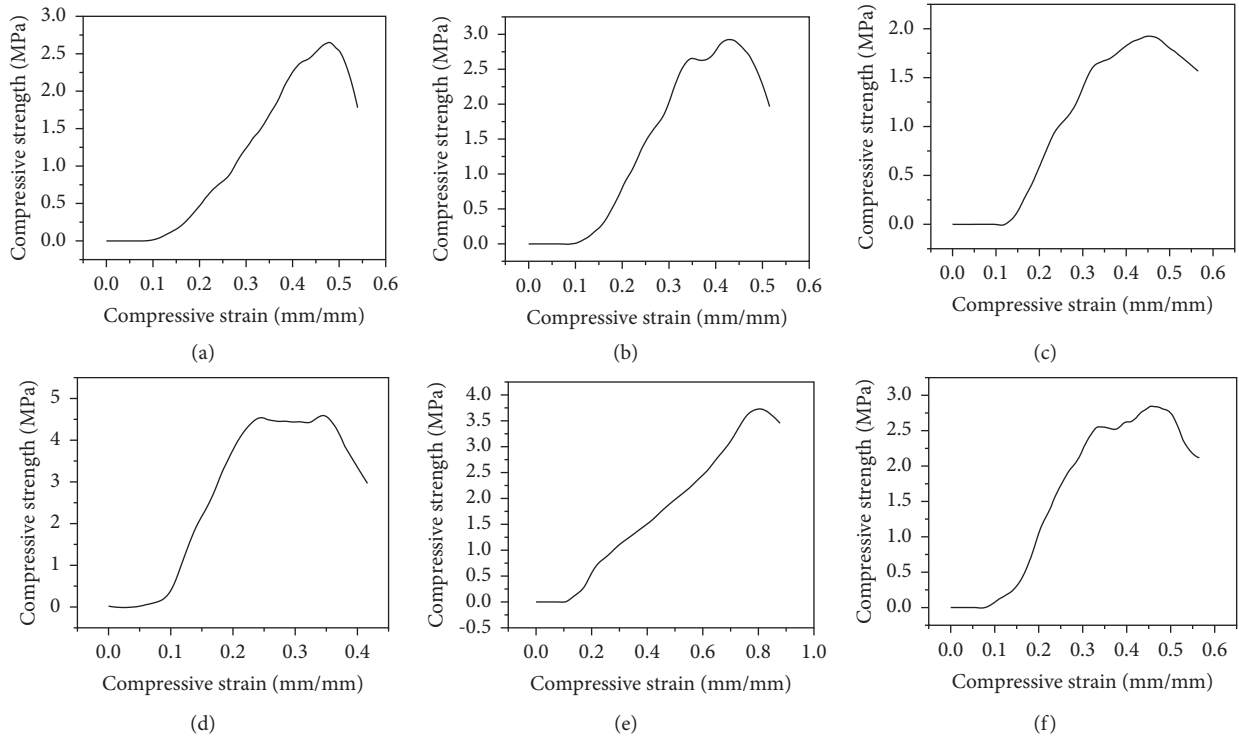
Figure 5: Compressive stress-strain curves of CPCP. (a). J-1. (b). J-2. (c). J-3. (d). J-4. (e). J-5. (f). J-6.
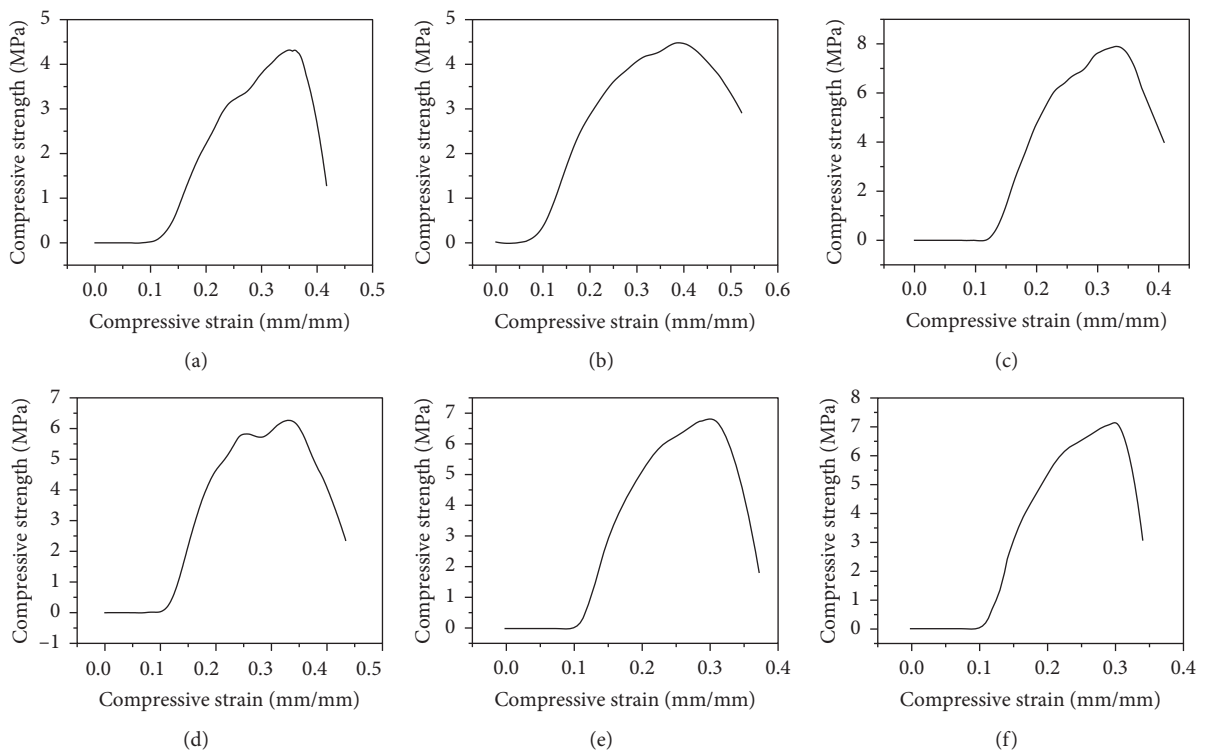
Figure 6: Compressive stress-strain curves of CNMCP. (a). X-1 (b). X-2 (c). X-3 (d). X-4 (e). X-5 (f). X-6.

increases, the fracture behavior of CNMCP gradually changes from hard and brittle (X-6 and X-5) to soft and weak (X-1). Table 6 shows the comparison between the bending strengths of CPCP and CNMCP.

Except for some individual points, the compressive strength of CNMCP grows as the addition of pulverized coal decreases. With low content of pulverized coal, HGB in the composite can enhance the rigidity. Besides, the small

TABLE 5: Comparison between compressive strengths of CPCP and CNMCP.

Mass of the added pulverized coal (g)		100	90	80	70	60	50
Compressive strength (MPa)	Coal-polyurethane	2.65	3.01	1.94	4.64	3.73	2.92
	Coal-new material	4.36	4.50	4.90	6.38	6.81	7.14
Percent of enhancement (%)		64.5	49.5	153	37.5	82.5	145
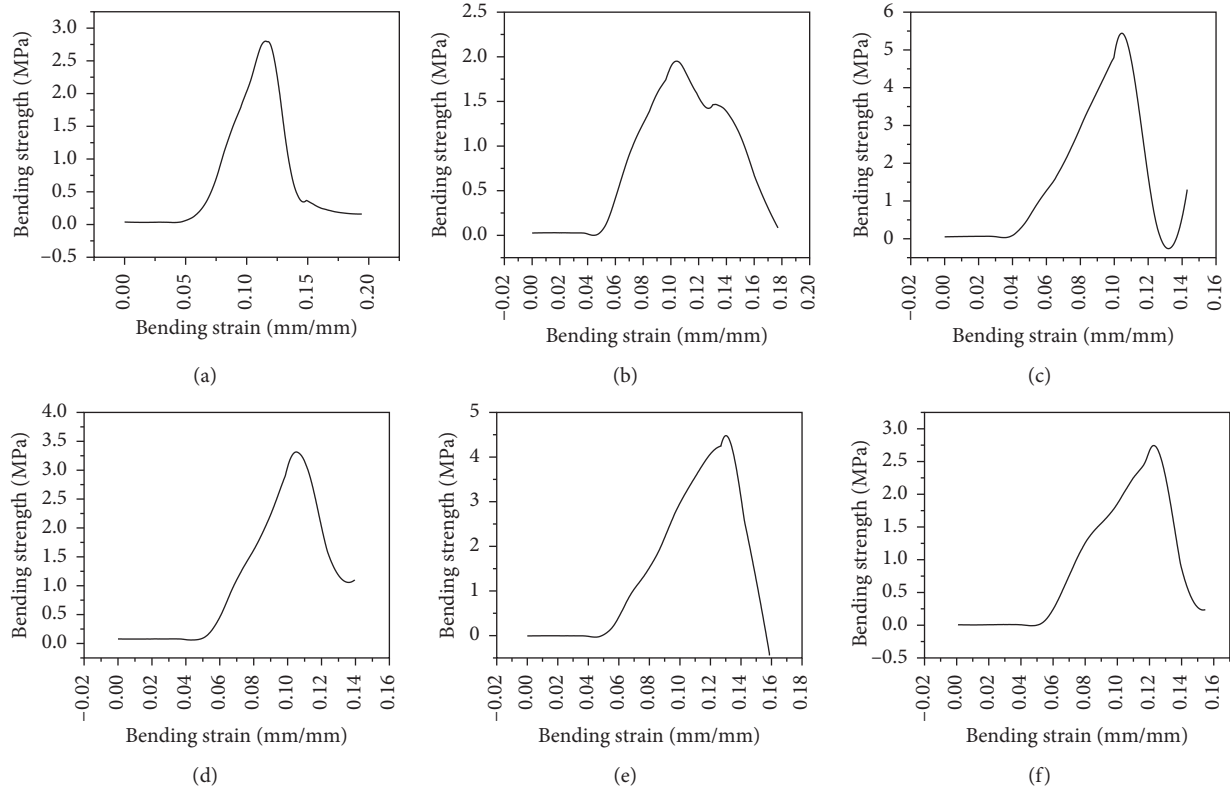
FIGURE 7: Bending stress-strain curves of CPCP. (a). J-1. (b). J-2. (c). J-3. (d). J-4. (e). J-5. (f). J-6.

amount of pulverized coal can uniformly disperse in the cells formed during the foaming process of the material, which makes foaming of the new material more difficult. Accordingly, the density of CNMCP is further improved, and its mechanical strength is enhanced.

On the premise of the same mass ratio, the bending strength of CNMCP is larger than that of CPCP (excluding X-3) and is up to 161% greater than the compressive strength of CPCP. The new material exhibits stronger interaction with coal and better performance of permeating coal and bonding loose coal seam than traditional polyurethane.

5. Industrial Test

The test was conducted in Xinyuan Coal Mine, Shanxi Province, China. The actual application effect of pressure measurement with the new material was verified by measuring the original gas pressure in No. 3 coal seam of the mine. No. 3 coal seam is about 23 m away from the upper K_8 sandstone and is in the middle of Shanxi Group. According to the drilling data of exploration and construction, most of the coal seam is recoverable, except No. 1, No. 2, and No. P30

boreholes near the western boundary and No. P75 borehole near the northeast boundary of the minefield. The thickness of the coal seam lies in the range of 0.40–4.75 m and averages 2.58 m. The coal seam is mostly recoverable and stable with a recoverable area of 128.787 km², a thickness variation coefficient of 24%, and a recoverability index of 0.97. Besides, it contains 0–3 layers of stone and partially 6 layers. It has a simple structure. The coal seam roof generally consists of mudstone, sandy mudstone, siltstone, fine/medium/coarse sandstone, and partially carbon mudstone, while its floor is mainly composed of mudstone, sandy mudstone, fine sandstone, siltstone, carbon mudstone, and partially coarse sandstone. The coal seam has now formed a certain area of goaf in the north central part of the minefield.

Four groups of boreholes were drilled in No. 3 coal seam. Each group included two pressure-measuring boreholes arranged in the coal seam. After the drilling was completed, polyurethane and the new material were applied to pregrouting. The former was used for No. 2, No. 4, No. 6, and No. 8 boreholes, while the latter was adopted for No. 1, No. 3, No. 5, and No. 7 boreholes. Specific technical parameters and measurement results are listed in Table 7.
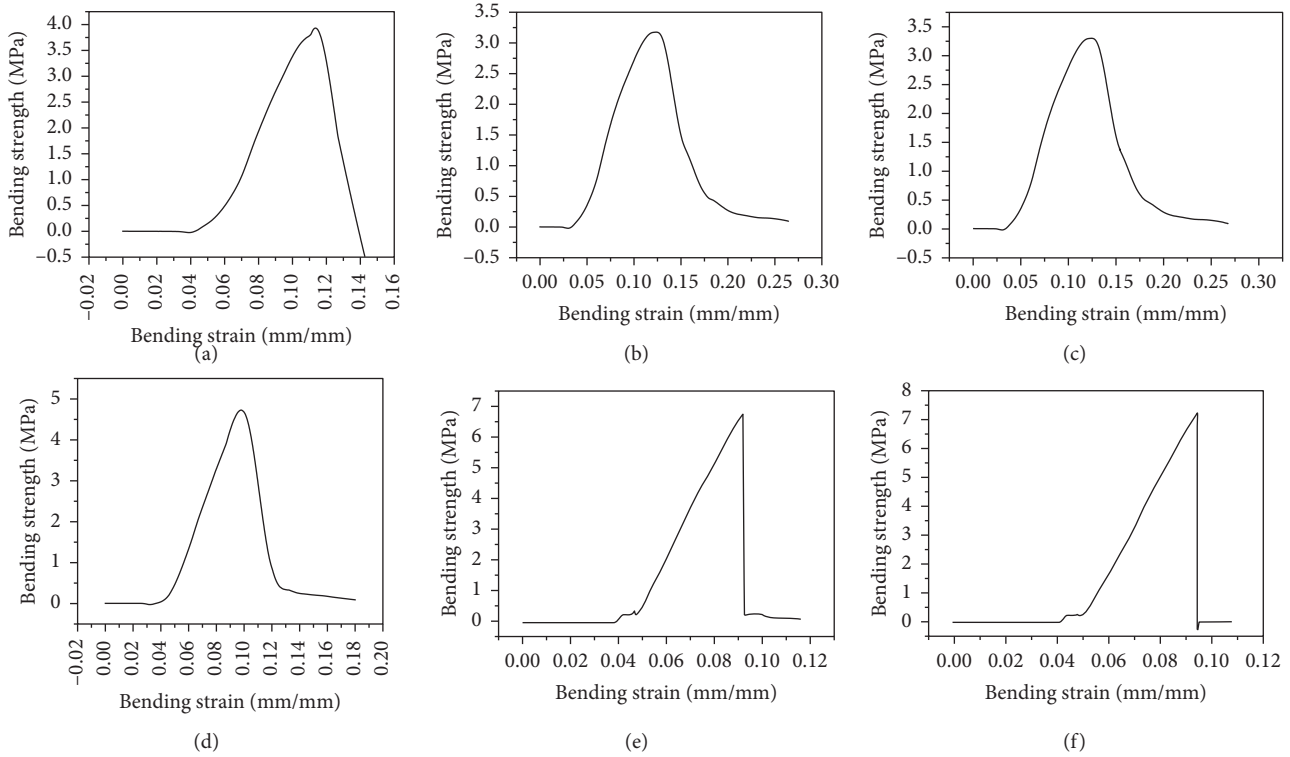
FIGURE 8: Bending stress-strain curves of CNMCP. (a). X-1 (b). X-2 (c). X-3 (d). X-4 (e). X-5 (f). X-6.

TABLE 6: Comparison between bending strengths of CPCP and CNMCP.

Mass of the added pulverized coal (g)		100	90	80	70	60	50
Bending strength (MPa)	Coal-polyurethane	2.94	2.13	5.32	3.50	4.34	2.77
	Coal-new material	3.86	3.17	3.31	5.00	6.76	7.25
Percent of enhancement (%)		31.3	48.8	−37.8	42.9	55.8	161

TABLE 7: Technical parameters of pressure-measuring boreholes.

	No.	Location	Elevation (m)	Buried depth (m)	Dip (°)	Actual hole length (m)	Measured pressure (MPa)
Comparative group 1	1#	1,471 m from no. 3108 return roadway	636	463	2	55.2	0.39
	2#	1,491 m from no. 3108 return roadway	636	463	2	55.7	0.38
Comparative group 2	3#	1,223 m from no. 3108 return roadway	627	472	2	53.7	0.41
	4#	1,203 m from no. 3108 working face	628	471	2	53.6	0.41
Comparative group 3	5#	1,100 m from no. 3412 return roadway	594	505	2	55.8	0.52
	6#	1,125 m from no. 3412 return roadway	596	503	2	55.4	0.50
Comparative group 4	7#	290 m from no. 3412 return roadway	579	520	2	53.2	0.67
	8#	310 m from no. 3412 return roadway	576	523	1	53.3	—

The construction of pressure-measuring boreholes by bedding drilling and the analyses on measurement results of gas pressure in Table 7 demonstrate that during the secondary borehole formation by bedding drilling, the new material can permeate the loose layer deep and interact with coal due to its excellent low-pressure permeability. The

pregrouting by the new material for reinforcement and sealing can better strengthen the coal and seal cracks, and the pressure-measuring boreholes are hard to collapse after formation. In the field practice of pressure measurement, boreholes with the new material can be constructed normally, and the sealing capsule can be smoothly put into the predetermined position, ensuring the success of pressure measurement via bedding drilling. However, of the four boreholes plugged and reinforced by polyurethane, one (No. 8) collapses in the secondary borehole formation process. The capsule fails to be put in the right position, which results in failure of pressure measurement.

6. Conclusions

(1) Based on analyses of stress distribution of coal around bedding drilling, there are three failure modes of bedding drilling, namely, partial borehole-bottom failure, partial borehole-wall failure, and structural instability of coal surrounding the borehole.

(2) The interaction between the new material and coal was studied to investigate the permeability of the new material in coal. The experimental results prove that the new material possesses better properties than the traditional polyurethane. The maximum and minimum effective consolidation distances (33 mm and 27 mm, respectively) of the new material in coal are higher than those (22 mm and 20 mm, respectively) of polyurethane. Besides, the average effective consolidation distance increases from 21 mm to 29.4 mm, with an increase of 40%. Furthermore, under the original coal stress of 10 MPa, the relationship between the experimental value of permeation radius of the new material and the theoretical value of radius of the plastic softening zone is also explored. The results reveal that the new material can better permeate the plastic softening zone than polyurethane and can thus more effectively consolidate the broken coal.

(3) To research the bonding effect between the new material and coal, a test was performed on mechanical properties of CNMCP. The results indicate that the CNMCP has better mechanical properties than CPCP. With the same mass ratio, the enhancement of compressive and bending strength of CNMCP is up to 153% and 161%, respectively, and the lowest enhancement can also reach 37.5% and 31.3%, respectively.

Data Availability

The original data used to support the findings of this study are available from the corresponding author upon request.

Conflicts of Interest

The authors declare that there are no conflicts of interest regarding the publication of this paper.

References

[1] V. Václavík, J. Daxner, J. Valíček et al., "Utilization of sludge from mine water treatment plant in the segment of thermal insulation mortars," *Archives of Environmental Protection*, vol. 40, no. 1, pp. 51–59, 2014.

[2] A. Tosun, "Development of a technology to prevent spontaneous combustion of coal in underground coal mining," *Journal of the Southern African Institute of Mining and Metallurgy*, vol. 117, no. 12, pp. 1133–1138, 2017.

[3] A. Verma, G. Chauhan, and K. Ojha, "Synergistic effects of polymer and bentonite clay on rheology and thermal stability of foam fluid developed for hydraulic fracturing," *Asia-Pacific Journal of Chemical Engineering*, vol. 12, no. 6, pp. 872–883, 2017.

[4] Z. Ge, X. Mei, Y. Lu, J. Tang, and B. Xia, "Optimization and application of sealing material and sealing length for hydraulic fracturing borehole in underground coal mines," *Arabian Journal of Geosciences*, vol. 8, no. 6, pp. 3477–3490, 2015.

[5] F.-b. Zhou, B.-b. Shi, Y.-k. Liu, X.-l. Song, J.-w. Cheng, and S.-y. Hu, "Coating material of air sealing in coal mine: clay composite slurry (CCS)," *Applied Clay Science*, vol. 80-81, no. 4, pp. 299–304, 2013.

[6] X.-m. Guan, Z.-p. Yang, and C.-j. Zhang, "Bonding mechanism between waterglass/polyurethane adhesive and coal," *The Journal of Adhesion*, vol. 88, no. 9, pp. 802–811, 2012.

[7] R. Yang, S. Fan, Q. Liu et al., "Research of mine polymer reinforcement materials of low toxicity smoke," *Guangdong Chemical Industry*, vol. 43, no. 8, pp. 63-64, 2016.

[8] J. Zhao, "Research on PET used for mine reinforcement material of polyurethane," *China Plastics Industry*, vol. 38, pp. 144–146, 2010.

[9] H. Wu, D. Han, and H. Wu, "New research progress and application of the silicate modified grouting consolidation materials," *Coal Science and Technology*, vol. 43, pp. 29–31, 2015.

[10] S. Zhu, R. Xia, Y. Tang et al., "Influence of antistatic agent on the comprehensive performance of polyurethane grouting material for coal mine," *New Chemical Materials*, vol. 43, no. 5, pp. 232–236, 2015.

[11] C. Jia and B. Zheng, "The application of polymer double liquid chemical materials in the reinforcement of the large fault plugging water injection," *Shandong Coal Science and Technology*, vol. 23, no. 11, pp. 91–95, 2017.

[12] Z. Feng and H. Kang, "Development and application of new waterproof grouting materials of polyurethane," *Chinese Journal of Geotechnical Engineering*, vol. 32, no. 3, pp. 375–380, 2010.

[13] Y. Song and Q. Gao, "Mechanism of grouting for waterproof using organic material with high water content," *Journal of Mining & Safety Engineering*, vol. 23, no. 3, pp. 320–323, 2006.

[14] D. Guo, Z. Cheng, J. Yunqi et al., "Performance test of the composite polyurethane of water glass-nano-silica as grouting material," *Modern Mining*, vol. 23, no. 4, pp. 157–160, 2018.

[15] C. Jiang, J. Cao, H. Jiang et al., "Polyurethane-pre-grouting-high pressure grouting sealing technology of coal seam gas pressure measurement," *Coal Technology*, vol. 33, no. 9, pp. 315–317, 2014.

[16] L. Zhang, G. Chang, B. Lin et al., "Application of new PD material in gas drainage and hole sealing," *Coal Engineering*, no. 1, pp. 43–45, 2013.

[17] L. Ning, Q. Zhao, Z. Xin et al., "A new type of polyurethane polyurea gas extraction sealing material," *Modern Chemical Industry*, vol. 35, no. 10, pp. 81–83, 2015.

[18] A. Li, *Preparation and Study on Safety Performance of Pre-Grouting Material and Its Application in Coal Seam Gas Pressure Measurement Method*, China University of Mining and Technology, Xuzhou, China, 2018.

[19] Y. Han, F. Zhang, and Z. Yang, "Analysis of stability of coalbed borehole wall," *China Safety Science Journal*, vol. 24, no. 6, pp. 80–85, 2014.

[20] L. Xu, *Experiment Study on Method of Initial Gas Emission from Borehole for Outburst Prediction in Cross-Cut Coal Uncovering*, China University of Mining and Technology, Xuzhou, China, 2015.

[21] X. Ding, Y. Ding, and S. Yu, "Incipient fracture of coal under one dimension gas seepage," *Chinese Journal of Theoretical and Applied Mechanics*, vol. 22, no. 2, pp. 154–162, 1990.

[22] Z. Wang, Y. Liang, and H. Jin, "Analysis of mechanics conditions for instability of outburst-preventing borehole," *Journal of Mining and Safety Engineering*, vol. 25, no. 4, pp. 444–448, 2008.

[23] Q Fan, *Stability Analysis Pf Horizontal Directional Drilling Hole-Wall and Application in Engineering*, Xi'an University of Science and Technology, Xi'an, China, 2010.

[24] C. Jiang and Q. Yu, *The Spherical Shell Instability Mechanism and Prevention Technology of Coal and Gas Outburst*, China University of Mining and Technology Press, Xuzhou, China, 1998.

[25] H. Li, G. Yin, J. Xu et al., *Rock Fracture Mechanics*, Chongqing University Press, Chongqing, China, 1988.

[26] Q. Deng, Y. Luan, and Y. Wang, "Coal and gas outburst simulation test," *Safety in Coal Mines*, vol. 11, pp. 5–10, 1989.

WILEY | Hindawi

Research Article

Sealing Performance of New Solidified Materials: Mechanical Properties and Stress Sensitivity Characterization of Pores

Chao Zhang ⓘ**,[1,2] Gaohan Jin** ⓘ**,[1,2] Chao Liu** ⓘ**,[1,2] Shugang Li** ⓘ**,[1,2] Junhua Xue** ⓘ**,[1,2] Renhui Cheng** ⓘ**,[1,2] and Hua Liu** ⓘ**[1,2]**

[1]*College of Safety Science and Engineering, Xi'an University of Science and Technology, Xi'an, Shanxi 710054, China*
[2]*Key Laboratory of Western Mine Exploitation and Hazard Prevention of the Ministry of Education, Xi'an 710054, China*

Correspondence should be addressed to Chao Zhang; zc@xust.edu.cn

Borehole-sealing solidified material plays a significant role in improving sealing quality and enhancing gas drainage performance. In this study, the MTS815 electro-hydraulic triaxial servo test system and MR-60 NMR test system were adopted to conduct triaxial compression control experiment on the coal sample material, concrete material, and new solidified sealing material, respectively. This paper aims to analyze the difference of support effects, porosity, and stress sensitivity between those materials. Experimental results show that under the same stress condition, the stiffness of traditional concrete solidified material is the largest, while the new solidified material is the second, and the coal sample material is the smallest. Compared with the traditional concrete solidified material, the new solidified sealing material has better strain-bearing capacity and volumetric expansion capacity under each confining pressure in the experiment. The axial strain and volume increment of new solidified material is higher than those of the traditional concrete solidified material at the peak stress. Meanwhile, the confining pressure has a certain hysteresis effect on the postpeak stress attenuation. Fracture has the strongest stress sensitivity in three pore types, and its T_2 map relaxation area has a larger compression than adsorption pore and seepage pore under the same pressure. The relative content of seepage pore and fracture in the new solidified material is less than that of coal and concrete samples, and the stress sensitivity of the new solidified materials is weaker than that of coal and concrete materials, thence, new solidified material will have better performance in borehole sealing. Outcomes of this study could provide guidance on the selection of the most effective sealing materials for sealing-quality improvement.

1. Introduction

Coal is the main energy source in China, accounting for over 70% of the primary energy [1]. However, most coal seams in China have complex and variable conditions, and the proportion of high gas coalmines is large [2]. Gas-related incident is always one of the most serious disasters during coal mining. Therefore, prevention and control of gas disasters is particularly significant. Many scholars have conducted a large amount of research in this area [3–6]. Some studies focused on sealing materials [7–9], while others concentrated on the sealing process [10–13]. Quanle Zou et al. established an improved coalbed methane combined mining model and proposed a combination method of borehole-grooving-separation-blocking to improve coalbed methane permeability and coalbed methane recovery [14]. Zhou et al. developed a new sealing material and analyzed the effects of various factors on material

properties [9]. Zheng et al. studied the sealing performance of a cement-based capillary crystalline material [15]. Baiquan Lin et al. proposed a borehole hydraulic grooving technology to eliminate coal and gas outburst threats that are more likely to occur during roadway excavation [16].

Currently, the primary method of controlling methane incidents is gas extraction, which has been vital and been generalized in China [17, 18]. Furthermore, borehole sealing is a vital factor to the gas extraction efficiency. The borehole-sealing quality is closely related to the solidified sealing material [19]. The mining team of coal and methane has developed a new type of solidified material for sealing (Figure 1), it can optimize the deficiencies of traditional materials in terms of initial setting time, fluidity, and expansion, however, the porosity and mechanical properties of the material during sealing are still to be studied. Hence, investigation on strength, stiffness, and elasticity modulus of sealing solidified materials after

(a)   (b)

Figure 1: Photographs of the new solidified sealing material. (a) Flow condition. (b) Solidification state.

swelling and solidification could have a positive impact on the stability of borehole sealing section, the avoidance of stress concentration and increase in gas-extraction efficiency.

The rock stratum around borehole is usually in three-dimensional stress state, it is necessary to study on the stress-strain characteristics of new solidified materials to further understand the properties of the material. The triaxial compression test is a common method for studying the transformation and strength characteristic of wall rock in three-dimensional stress state. Many remarkable signs of progress have been made by conducting numerous experiments in the triaxial compression condition [20, 21]. Morgan Chabannes et al. evaluated the shear behavior of two different biobased concretes using triaxial compression [22]. Meanwhile, other researchers also made some advances in mechanical properties of coal rock, especially for the strength and deformation behaviors [23–25].

As an important material for borehole sealing, the change of porosity and stress sensitivity under pressure are also several important characteristics for characterizing material properties. Some researchers have discussed the stress sensitivity and porosity under different stress state based on a series of experiments of coal and rock samples [26–28]; Li used the transverse relaxation time (T_2) spectrum of nuclear magnetic resonance to conduct quantitative study of the compression characteristics of pore-fracture system [29]; Meng studied the differences of gas adsorption-diffusion and adsorption deformation of low and high rank coal and its permeability evolution in isothermal adsorption experiment and desorption-seepage testing system [30]; Wang revealed the characteristics of micropore, mesopores, and fractal dimensions of bituminous coal during the process of cyclic gas adsorption/desorption by combining N_2 and CO_2 adsorption experiments from microscopic aspect [31]. However, the methods commonly used such as mercury intrusion porosimetry (MIP), N_2 adsorption desorption [32], and small angle scattering may cause some damage to the sample matrix. Compared with other methods, nuclear magnetic resonance (NMR) technology has a faster and more accurate representation of the pore distribution in the sample without damaging it, it has been widely used by some researchers to study the size, content, and distribution of pores [33–40].

In this study, the advanced electro-hydraulic triaxial servo test system (MTS815) and the MR-60 NMR test system were applied to conduct the triaxial compression experiments and NMR scanning experiment of coal sample materials, concrete materials, and solidified materials. The variation of stress-strain and elastic modulus under different confine pressure were analyzed, meanwhile, the variation of strength and the effects of confining pressure on them between three specimens were comparatively analyzed. Based on T_2 spectrum, the relaxation area change was used to calculate the compressive capacity of the three pores, the variation of relative content of the different pore types in different samples was discussed. Additionally, the stress sensitivity of the different types of pores was compared by the calculation of dimensionless constants, and the sealing performance of different sealing materials was compared. It is considered that the achievements of the study will be one of the better guidance for advancement of borehole sealing process and improvement of drilling efficiency of gas drainage.

2. Experimental

2.1. Geological Setting and Sample Information. The coal samples were taken from the Yuwu Coal Mine of the Lu'an Group in Changzhi City, Shanxi Province, China, as shown in Figure 2. New solidified sealing materials and concrete materials were formed in the laboratory according to the actual mix ratio, the new solidified material is based on ultra-fine Portland cement, other additives are: reagent grade aluminum powder, CaO, and gypsum, and the partial proportions are shown in Table 1. The content of aluminum powder and CaO is 0.56%, the gypsum content is 2%, and the water–cement ratio is 0.6%.

2.2. Experimental Methods. The triaxial loading experiment used the three-dimensional compression MTS815 experiment system. This machine is mainly composed of a loading system, measuring system, and controlling system. The maximum axial load, confining pressure, and the applied range of the strain rate are 4600 KN, 25 MPa, and 10^{-7}–10^{-2}/s, respectively.
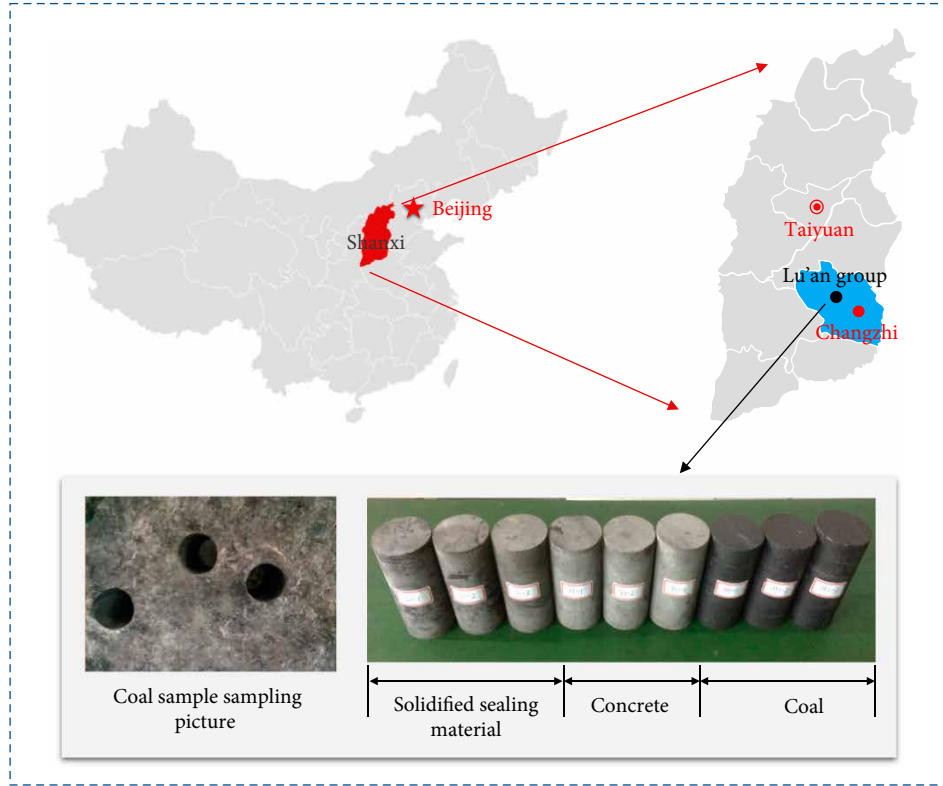
FIGURE 2: Basic information of the sampling area sampling process.

TABLE 1: New solidified material composition content.

	Concrete ratio							Additives ratio		
Ingredient	SiO_2	Al_2O_3	Fe_2O_3	CaO	MgO	SO_3	Loss	CaO	Gypsum	Al
Content	23.23%	6.58%	3.51%	58.41%	2.43%	2.96%	2.88%	0.56%	2%	0.56%

Meanwhile, all test parameters in the experimental process are obtained using high-accuracy sensors. All operations are controlled by axial displacement at the rate of 0.0015 mm/s. Meanwhile, three confining pressures of 7, 5, and 3 MPa are adopted. In the experimental process, put confining pressure to a scheduled time firstly, then add axial displacement to the samples. It should be pointed out that all samples would be covered up using electrical adhesive tape for avoiding the impact of oil on the samples strength and results.

For NMR testing, each sample was placed in a vacuum and saturated with distilled water unit for 48 h to its complete saturation, the core holder has a double-layer structure. The main magnetic field of the device is 0.51 T, the RF pulse frequency is 1.0~49.9 MHz, and the RF power is 300 W, the NMR testing parameters are set as flowing: echo interval time is 0.233 ms, the number of echoes is 6000, number of scans is 32, and the ambient temperature is 34°C. The T_2 spectral of each sample can be used to analyze the variation of content with various types of pore.

As shown in Figure 3. The experiment was conducted in three stages, in which each sample was initially tested by NMR and triaxial loading experiment, and these samples were then combined and fixed. In the last stage, the assembled samples were tested by the second round NMR experiment.

2.3. *Experimental Theory*. In the triaxial compression experiment, the maximum carrying capacity of coal, i.e., the axial peak strength σ_s under axial compression can be determined by:

$$\sigma_s = \frac{P_{max}}{A}, \tag{1}$$

where σ_s is the peak strength under different confining pressures, P_{max} is the axial failure load of samples, and A is the cross-sectional area.

The elasticity modulus of samples can be calculated using the Hooke laws as follows:

$$E\varepsilon_1 = \sigma_1 - 2\mu\sigma_3, \tag{2}$$

where μ is the Poisson ratio. Due to the invariability of confining pressure in the loading process, the formula could be changed into the following expression:

$$E = \frac{d\sigma_1}{d\varepsilon_1}. \tag{3}$$

Thus, the elasticity modulus could be obtained via the equation of $E = d(\sigma_1 - \sigma_3)/d\varepsilon_1$.

For NMR experiments, the distribution, connectivity, and various physical parameters of various types of pores in coal

FIGURE 3: Schematic of the experimental instrument and experimental procedure.

and rock mass are obtained based on the T_2 spectrum. The relationship between the transverse relaxation time T_2 of NMR and the aperture (r) can be expressed as [41]:
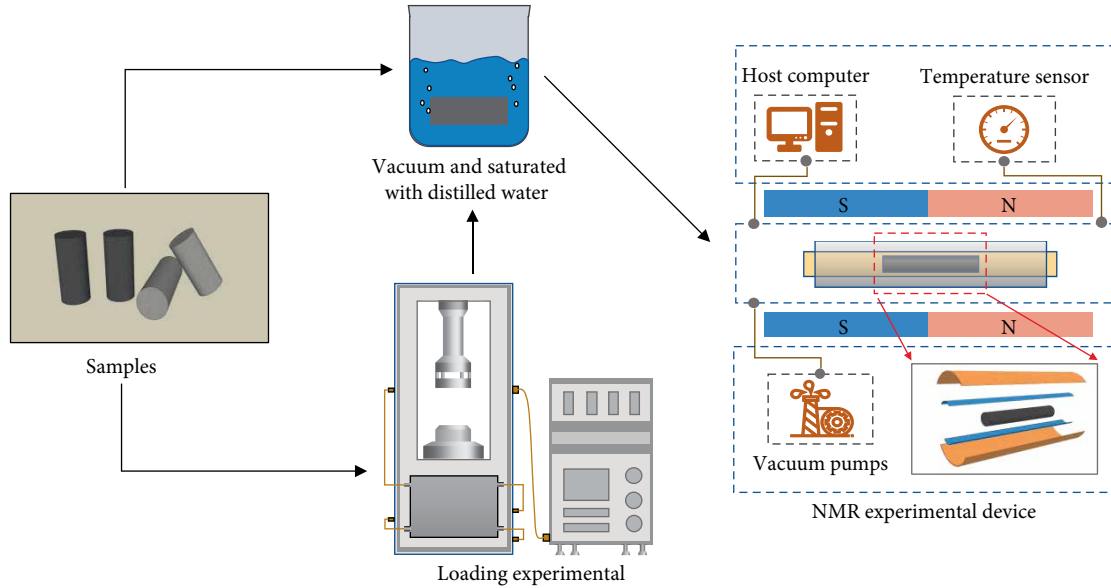
$$\frac{1}{T_2} = \rho \times \frac{S}{V} = F_S \times \frac{\rho}{r}, \tag{4}$$

where T_2 is the transverse relaxation time, ms, ρ is the transverse surface relaxation strength, μm/ms, S is the pore surface area, cm^2, V is the pore volume, cm^3, F_S is the pore shape factor, and r is the aperture.

To better characterize the effect of pressure on various pores in the samples, a parameter of S_i/S_0 is defined to characterize stress sensitivity of various pores. A dimensionless parameter of S_{pfi} is defined as [29, 42]:

$$S_{pfi} = \frac{S_i}{S_0}, \tag{5}$$

where S_i and S_0 is the relaxation area of the T_2 spectrum after three-axis compression at a confining pressure of P_i and P_0. In this paper, P_0 represents that the confine pressure equals to 0 (no confine pressure), and when i equals to 1, 2, 3, the confine pressure moves from 0 MPa to 3, 5, 7, respectively.

3. Experimental Results

Three-dimensional compression experiments of three samples (coal, concrete, and solidified materials) are conducted by the MST815 system until the complete failure of the samples. The axial load and displacement have been used to determine the stress and strain changes in the experimental process. The curves of three samples under different confining pressures are shown in Figure 4. The peak strength and strain can be calculated via those curves. Furthermore, the elasticity modulus (E) is also determined by the linear regression of stress and strain curves, which is shown in Table 2. NMR scanning

experiments were performed on all samples before and after the loading of experiments using the MR-60 NMR test system, the T_2 spectra of all samples were obtained by experiment (Figures 5–7). The relative content of different types of pores in the sample can be obtained by calculating the peak relaxation area in the T_2 spectrum [43].

4. Discussion

4.1. Analysis of T_2 Spectrum and Stress Sensitivity. It can be clearly seen from Figures 5–7 that there are three distinct peaks in the NMR spectra of the three samples, on the basis of previous studies, this paper divides the pore types into adsorption pore, seepage pore, and fracture according to the relaxation time of each peak in the T_2 spectrum [42, 44]. It also can be seen in the T_2 spectrum of the three samples that the main peak area is much larger than the two subpeak areas, which indicates that the absorption pore content of the three samples is the largest. It also can be seen that the relaxation area of the T_2 spectrum of this type of pore decreases to some extent after the triaxial load, and the relaxation area of the crack changes most obviously, indicating that it absorbs the pores of all samples after triaxial loading. The seepage porosity and fracture content decreased, and the fracture change was the largest.

It is worth noting that all the samples are conjugated and then subjected to NMR experiments after triaxial loading until the samples are completely destroyed, but the large-size cracks caused by the compression experiment are not within the detection range of the NMR experiment. Therefore, the NMR results of the samples after compression indicate the changes in the pore content of each sample under extreme stress, the experimental results can better reflect the characteristics of the new solidified sealing material, so the content of the fracture in the sample both before and after the experiment varies

(a)

(b)

(c)
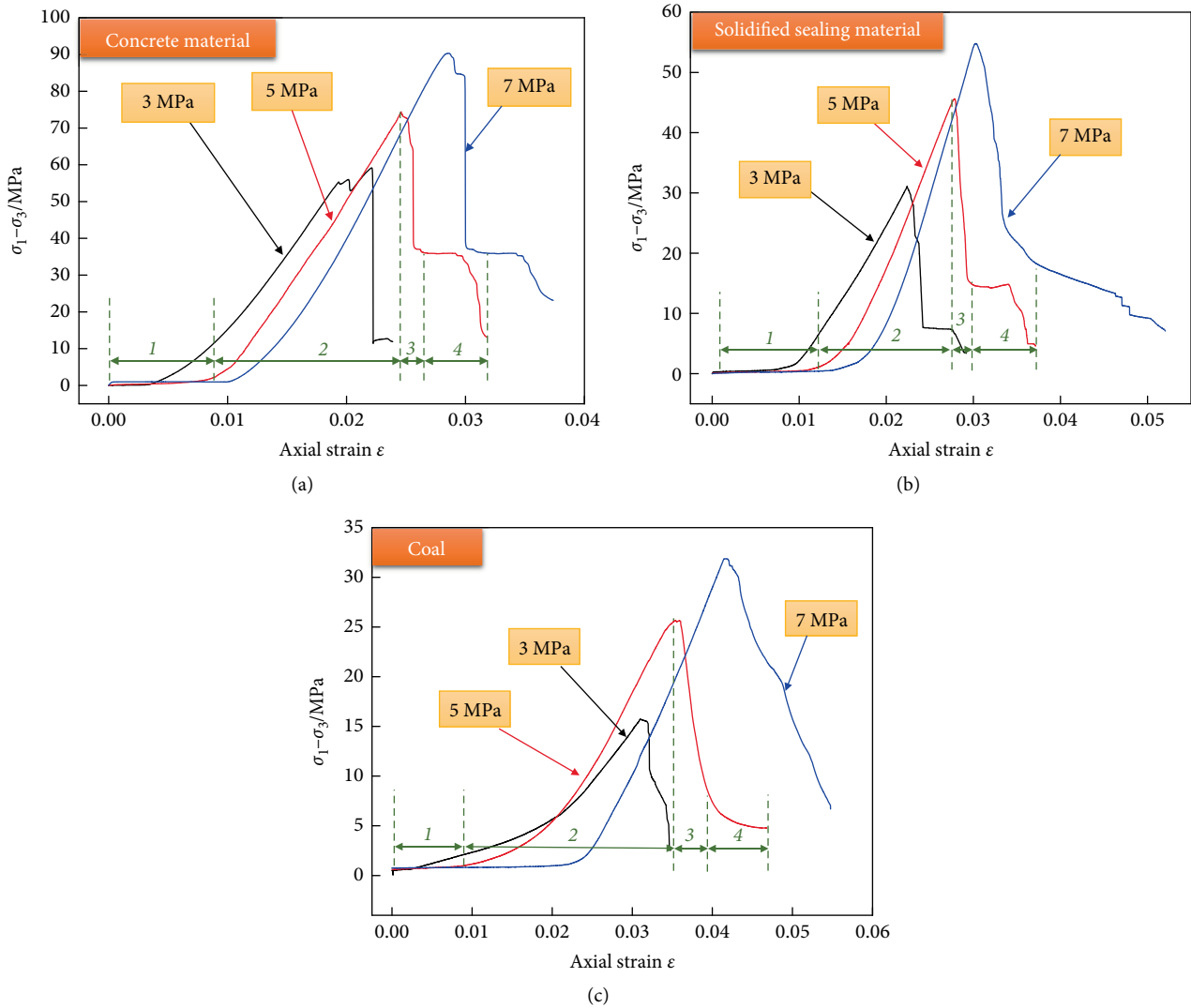
FIGURE 4: Stress–strain curves of three specimens under different confining pressures. (a) Stress–strain curves of concrete material. (b) Stress–strain curves of solidified sealing material. (c) Stress–strain curves of coal sample.

TABLE 2: Test results and parameters of three samples under different confining pressures.

Sample properties	Sample no.	Confining pressure σ_3/MPa	Peak intensity σ_s/MPa	Peak strain ε/mm·mm^{-1}	Elastic modulus E/GPa
Concrete material	HN1	3.0	59.13	0.02208	3.892
	HN2	5.0	74.41	0.02457	4.944
	HN3	7.0	90.34	0.02861	5.233
Solidified sealing material	GH1	3.0	31.09	0.02239	2.211
	GH2	5.0	45.61	0.02781	3.852
	GH3	7.0	54.78	0.03028	4.248
Coal sample	MY1	3.0	15.72	0.03096	0.545
	MY2	5.0	25.66	0.03541	1.330
	MY3	7.0	31.84	0.04157	2.083

greatly, and the change of the coal sample is the most significant. In Figures 5(b), 6(b), and 7(b), the dimensionless coefficient (S_{pfi}) of different pore types in each sample shows different degrees of change, and the trend generally shows an increasing trend with the increase of pressure, and the variation trend of S_{pfi} value of each pore type gradually become larger according to the order of adsorption pore, seepage pore, and fracture.
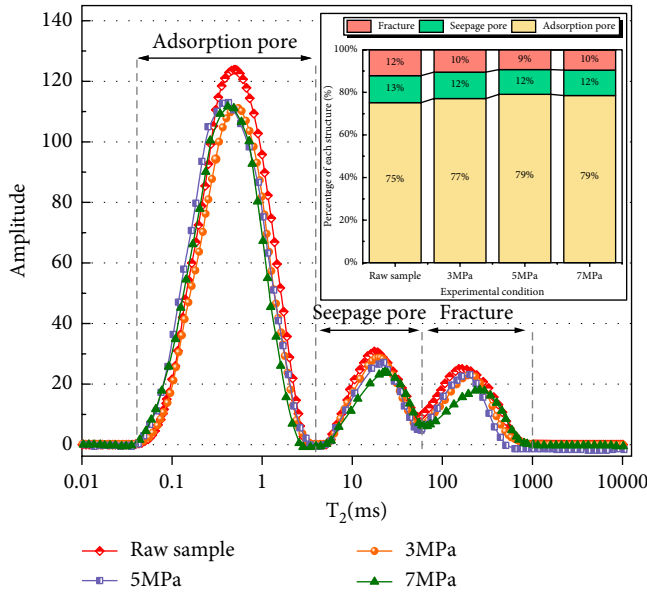
(a)
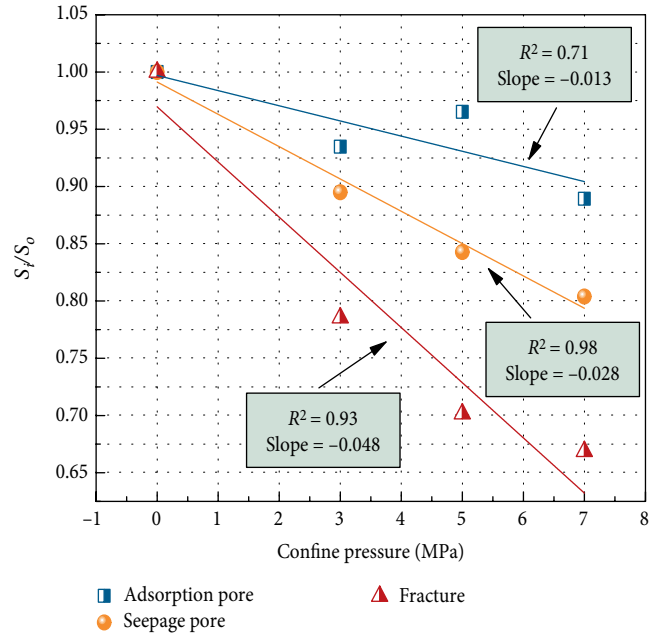
(b)

FIGURE 5: T_2 spectrum of the coal samples under different confining pressure.
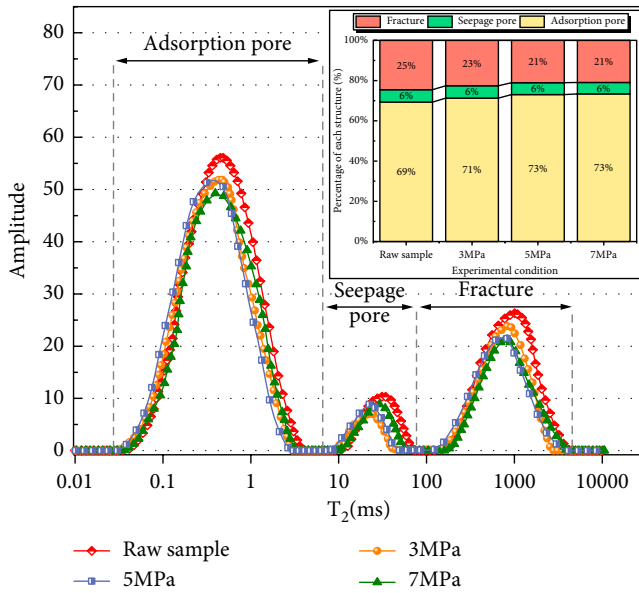
(a)
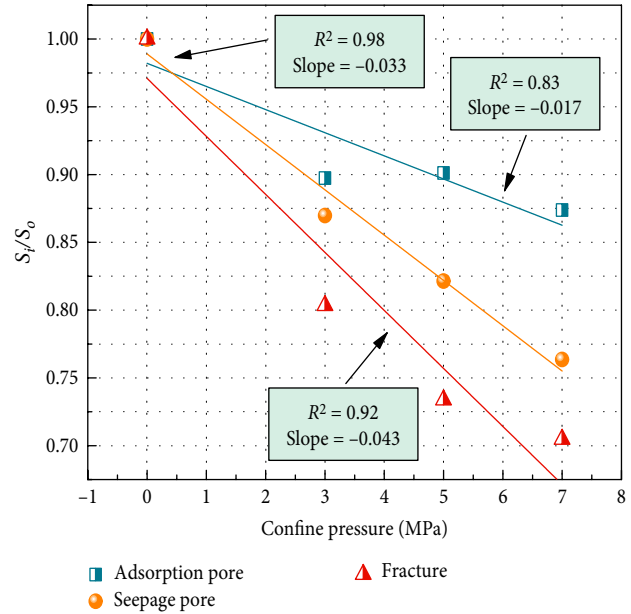
(b)

FIGURE 6: T_2 spectrum of the concrete samples under different confining pressure.

It can be found that the relative content of the fracture in the coal sample decreased to a certain extent after triaxial compression, from 12.17% of the total relaxation area before compression to 10.48%, 9.30%, and 9.55% of the total relaxation area after compression, respectively, and it can also be seen in Figure 5(b) that the S_{pfi} value of the fracture at the same confine pressure is the smallest, which indicates that the fracture content of the three pore types in the coal sample is the largest under the triaxial stress. The dimensionless coefficient (S_{pfi}) is

usually used to describe the pressure sensitivity of the sample. The larger the value of S_{pfi}, the smaller the compressible volume of the sample and weaker the pressure sensitivity. It can be seen from Figure 5(b) that the S_{pfi} values of different pore types in the coal sample tend to be smaller and smaller with the increase of confining pressure, when the effective confining pressure is raised to the highest point of 7 MPa, the S_{pf3} (S_3/S_0) values of the adsorption pore, seepage pore, and fracture are 0.89, 0.80, and 0.67, respectively. This indicates that the volume
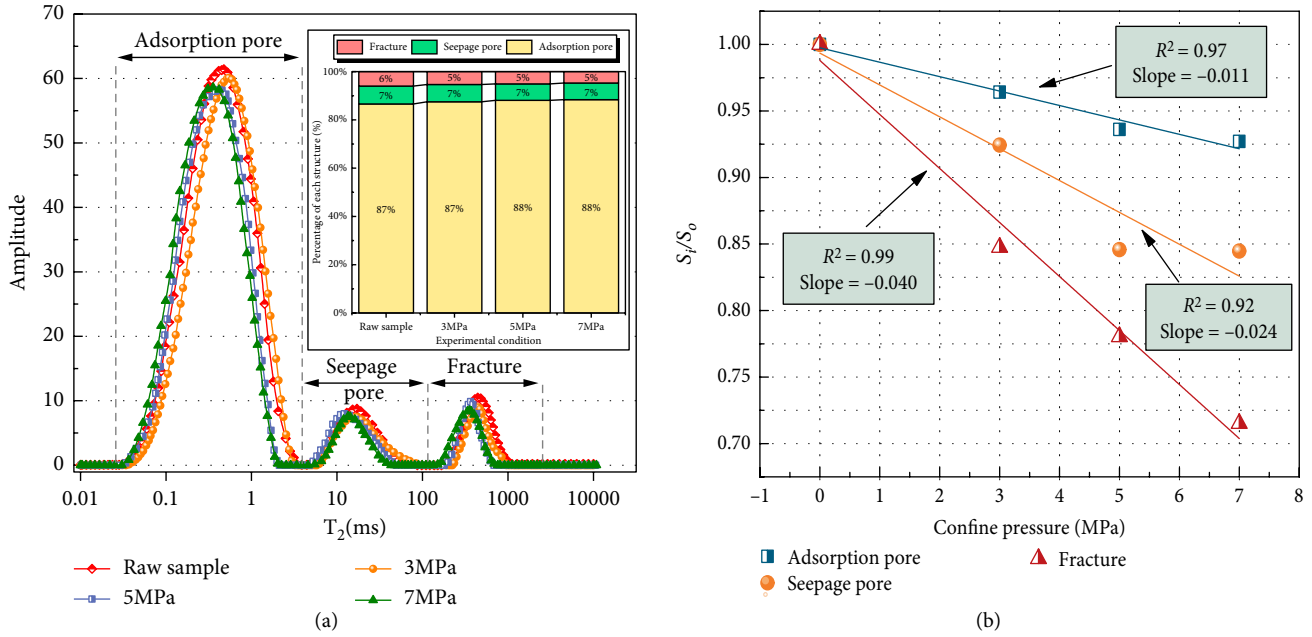
FIGURE 7: T_2 spectrum of the new solidified material samples under different confining pressure.

TABLE 3: Equation of the relationship between confine pressure and S_i/S_0.

Pore types	Coal	Concrete	New solidified material
Adsorption pore	$y = -0.0132x + 0.997$	$y = -0.0171x + 0.9821$	$y = -0.0108x + 0.9975$
Seepage pore	$y = -0.0282x + 0.9913$	$y = -0.0334x + 0.9890$	$y = -0.0240x + 0.9935$
Fracture	$y = -0.0482x + 0.9696$	$y = -0.0428x + 0.9710$	$y = -0.0406x + 0.988$

of adsorption pore, seepage pore, and fracture is compressed by 11%, 20%, and 33%, respectively. These results indicate that the pressure sensitivity of the fracture in the coal sample under triaxial loading is the strongest, the seepage pore is second, and the adsorption pore is the smallest.

In Figure 6(a), the relative content of the fracture in concrete samples is as high as 23%, which is much larger than the fracture content in coal samples and new solidified materials. Therefore, compared with the new solidified sealing materials, traditional concrete materials have more fractures, thereby affecting the sealing effect. It can be seen from Figure 6(b) that as the stress increases, the value of S_{pfi} of all pore types decreases gradually, in which the adsorption pore has the largest S_{pfi} value, the seepage pore is the second, and the fracture is the smallest. When the effective confining pressure reaches 7 MPa, the S_{pfi} values of adsorption pore, seepage pore, and fracture are 0.87, 0.76, and 0.70, respectively, which indicates that the pore volume of adsorption pore, seepage pore, and fracture is compressed by 13%, 24%, and 30%, respectively, and the downward trend of fracture is the largest (Figure 6(b) and Table 3), which indicates that the fracture pressure sensitivity of concrete samples is the strongest and most unstable.

Under different confining conditions, the relative content of seepage pore and fracture in the new solidified materials accounted for 13.40%, 12.50%, 11.90%, and 11.58% of the total pore area, respectively (Figure 8(a)), each value of them is smaller than that of the coal sample and the concrete material,

and its average content is 10.29% and 15.88% lower than that of coal and concrete, respectively. Which indicates that the relative content of the two types of transport channels that can provide gas flow in the new solidified material is less than that in the coal sample and the concrete material, so that the content of the pore type for gas circulation in the new solidified material is less than its content in concrete materials and coal samples, Therefore, the new solidified materials have better sealing performance than concrete materials.

According to Figure 7(b), the values of S_{pfi} of all types of pores decrease with the increase of effective confining pressure. When the effective confining pressure rises to a maximum of 7 MPa, the S_{pfi} values of adsorption pore, seepage pore, and fracture in the new solidified materials are 0.92, 0.84, and 0.72, respectively, which indicates that the pore volume of adsorption pore, seepage pore, and fracture is compressed by 8%, 16%, and 28%, respectively, and the downward trend of fracture is the largest (Figure 8(b)), so the stress sensitivity of the fracture in the new solidified material is the strongest. Seepage pore medium and the absorption pore are the weakest. Under the same experimental conditions, the S_{pfi} value of the new solidified material is mostly lower than that of the coal sample and the concrete material (Figure 9), and the variation trend of the new solidified material S_{pfi} value is smaller than that of the coal sample and the concrete sample (Figure 8(b) and Table 3), this indicates that the new solidified material has lower pressure sensitivity than the coal sample and the
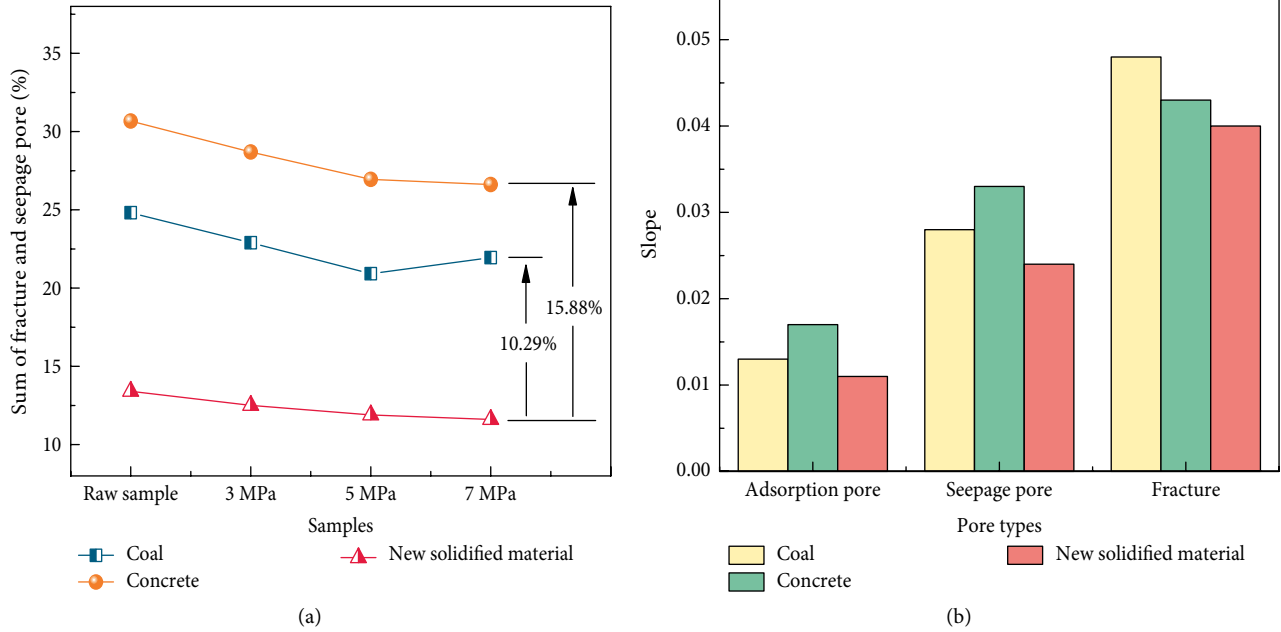
(a)

(b)

FIGURE 8: The relative content of macropores and the slope of S_i/S_0.

concrete sample, and the structure is more stable, which is more conducive to the drilling seal.

In general, it can be found that the pore content of all samples decreased to some extent after loading. The relative content of the adsorption pores in all samples is much larger than the seepage pore and fracture, and the stress sensitivity of the adsorption pore is weaker than the seepage pore and fracture. The content of the seepage pore and fracture in the new solidified material is smaller than that of the coal sample and concrete material, and it has fewer gas migration channels, which have better performance than concrete samples in borehole sealing. The pressure sensitivity of all types of pores in the new solidified materials is weaker than that of the coal samples and concrete samples, it has a slower trend of change, and its structure is more stable, which is more beneficial to drilling seals.

4.2. Analysis of Stress and Strain of Samples. The relationship curves of the stress difference and axial strain are obtained via analyzing the experimental data and shown in Figure 4. In this figure, curves (a), (b), and (c) are relation curves in different confining pressures. From those curves, it can be seen that all the peak strength and maximum axial variation increase with the confining pressure. The strength declines slower when the confining pressure becomes higher. The samples reach the plastic region earlier with small confining pressure. In this study, the strength and deformation behavior of the samples under different confining pressures are investigated based on the relationship between stress and strain, changes of elasticity modulus, the impact of wall rock on the stress, and strain and the failure angle. Meanwhile, the optimizing capacity of new solidified materials is analyzed, which could be very helpful for the coalmine borehole sealing improvement.

(1) In the process of axial compression of samples, there are four phases: the initial compaction phase,

elastic phase, yield phase, and failure phase [45]. The compaction phases of three samples increase with confining pressure. It is mainly due to the "End Effect" and the different axial elongation. The detailed information is expressed as follows:

When the stress is lower than proportional limits, the absolute value of the transverse strain (ε_1) and axial strain (ε) is a constant named Poisson's ratio μ:

$$\mu = \left| \frac{\varepsilon_1}{\varepsilon} \right|. \tag{6}$$

Because the confining pressure is added firstly, the transverse strain is produced. Hence, Eq. (6) can be expressed as follows:

$$|\varepsilon_1| = \mu |\varepsilon|. \tag{7}$$

The transverse strain increases with confining pressure. Based on Eq. (7), Poisson's ratio is the internal property of materials, which shows that the axial strain would increase with transverse strain. The axial strain augments the initial compression stages of materials. Hence, the rise of confining pressure would lead to an increase in the initial compression stage [46].

(2) In Figure 4, the peak strength and strain would increase with the confining pressure for the same lithology. Meanwhile, the increment would partly depend on material lithology. For instance, when the confining pressure changes from 3 MPa to 5 MPa, the corresponding increments of peak strength for three samples (solidified material, concrete material, and coal) are 25.83%, 46.54%, and 63.41%, respectively. When the pressure changes from 5 MPa to 7 MPa, the corresponding increments are 21.25%, 20.58%, and 24.27%, respectively.

(a)

(b)

(c)
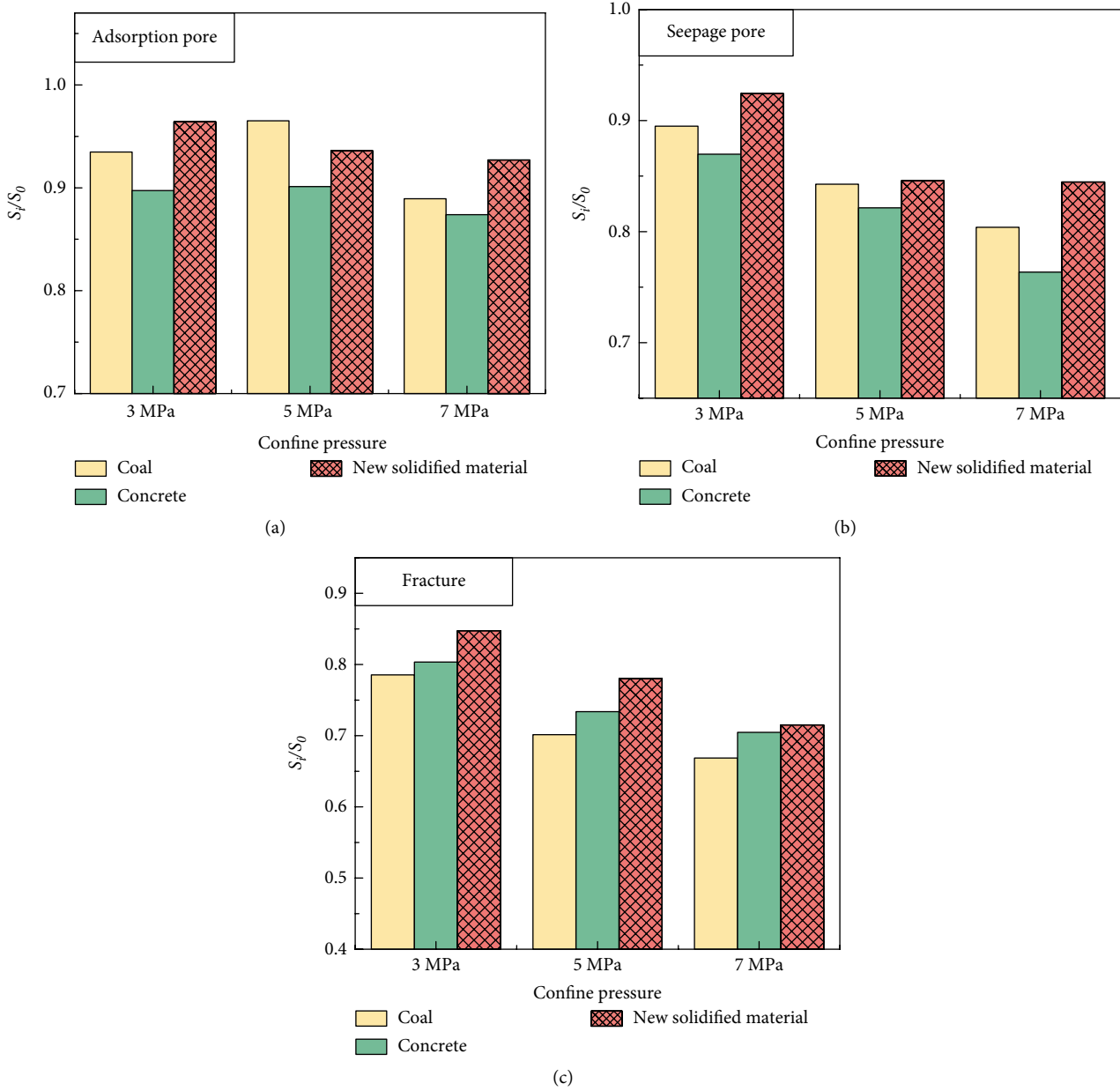
FIGURE 9: The value of S_i/S_0 in three types of pores.

The increments of peak strength from 3 MPa to 5 MPa are obviously higher than the rest, which is due to more fracture compression in the first phase than the rest. Furthermore, when the pressure changes from 3 MPa to 5 MPa, the most fracture compression in coal lead to its maximum peak strength increments. In the rest process, the peak strength increments are similar among the three samples.

(3) According to Figure 4 and Table 2, under the same confining pressure, the sort of peak strength from largest to smallest is concrete material, solidified material, and coal. In contrast, the sort is reversal in terms of peak strain. At the experimentally allowed space, three samples are loaded to the limits, as shown in Figure 4. Under different confining pressures, the stress and strain curves of concrete material reach the top and then decrease, eventually lose the loading capacity and experience brittle failure. The corresponding peak strength under confining pressure of 3 MPa decreases more quickly than that under confining pressure of 5 MPa, when stress and strain curves reach the top. Besides, the total strain quantity is larger under 5 MPa. Consequently, the concrete material experiences brittle failure while the rest experience slow changes from brittle failure to plastic failure when the confining pressure increases.

(4) In Figure 4, there is no intersection point between stress and strain curve at plastic stage of three samples. However, there are intersection points when confining pressure ranges from 3 MPa to 5 MPa, which means

(a)

(b)

(c)
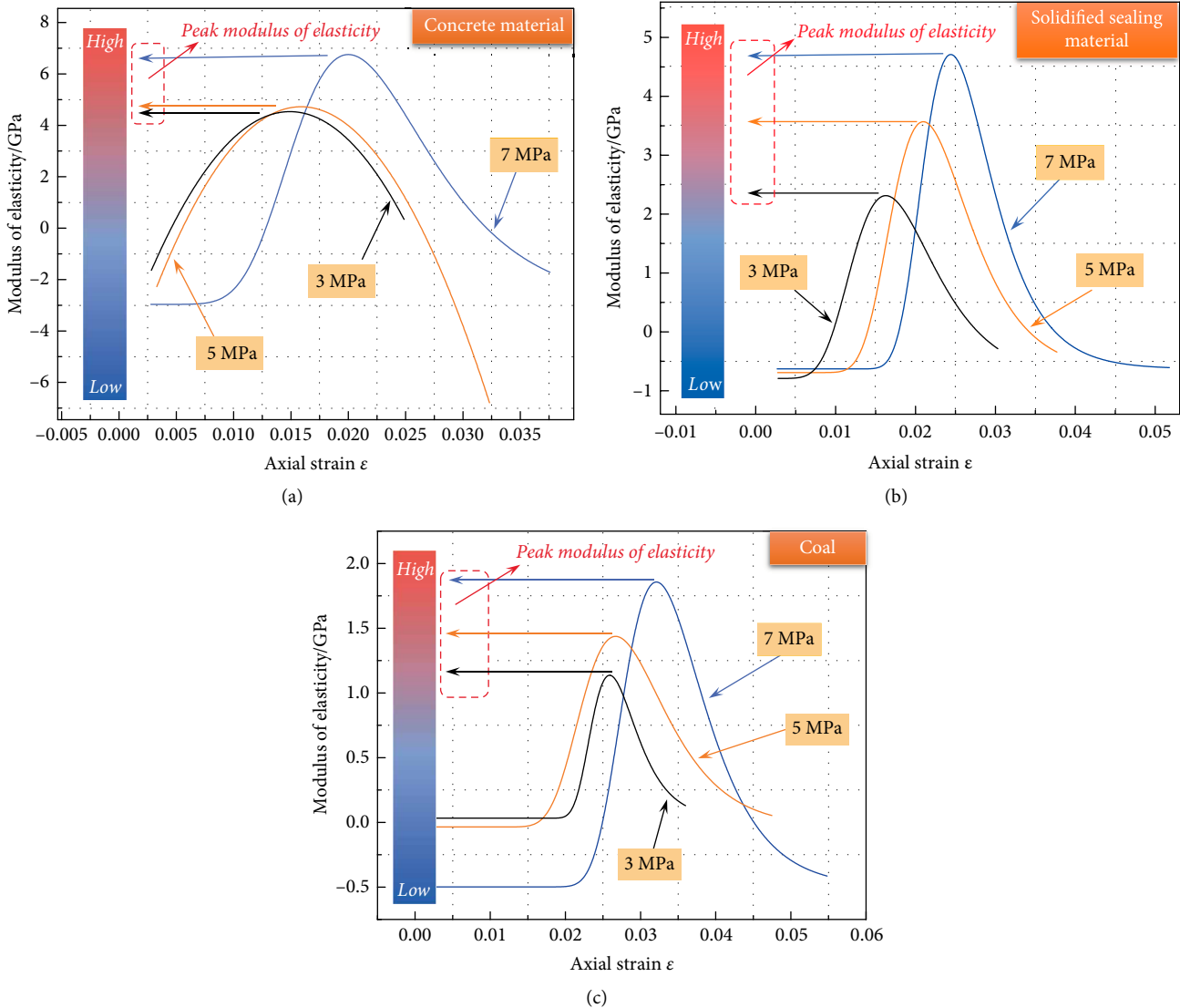
FIGURE 10: Elastic modulus-strain curves of three specimens. (a) Elastic modulus-strain curve of concrete materials. (b) Elastic modulus-strain curve of sealing solidified materials. (c) Elastic modulus-strain curve of coal.

that the increment of elasticity modulus in 3 MPa are lower than those in 5 MPa, as shown in Figure 10. According to experimental observation, this phenomenon is due to the appearance of more fractures in coal, which augments the elasticity modulus and rigidity during compression process.

4.3. Analysis on Elasticity Modulus.

(1) The elasticity modulus, which represents the capacity of plastic deformation resistance, is the amount of material severity. Based on previous theories, the elasticity modulus increases with the gradual compression of materials due to the disappearance of natural fractures and small cavities. However, in Figure 10, the samples with smallest confining pressure firstly reach the plastic deformation stage, which is due to the "End Effect" from high confining pressure and axial deformation from confining pressure loading. Besides, the longer compression time caused

by conquering larger friction force by axial strain also has an impact. Therefore, the lower confining pressure corresponds to shorter compression stage and larger elasticity modulus.

(2) According to Figure 10, the elasticity modulus of all samples firstly rise before decreasing with the increase in axial strain. Meanwhile, four stages could be observed in the sample deformation process based on curve trend: compaction phase, elastic phase, yield phase, and failure phase. In the compression stage, the elasticity modulus keeps a constant when the axial strain increases. Then, in plastic deformation stage, the elasticity modulus firstly increases under lower confining pressure. Afterwards, the elasticity modulus of samples under lower pressure reaches the top and maximum compression states as the axial strain increases. The samples under larger confining pressure keep deforming in a longer time. Then, the samples experience plastic failures and reach the failure stage. Eventually, the emerging fractures and cavities appear and the primary physical structures are damaged. Small cavities

TABLE 4: Peak elastic variable under different confining pressures of three samples.

Sample properties	Sample no.	Confining pressure σ_3/MPa	Fitting peak elastic modulus E/GPa
Concrete material	HN1	3.0	4.532
	HN2	5.0	4.723
	HN3	7.0	6.753
Solidified sealing material	GH1	3.0	2.313
	GH2	5.0	3.569
	GH3	7.0	4.709
Coal sample	MY1	3.0	1.136
	MY2	5.0	1.437
	MY3	7.0	1.857

FIGURE 11: Elastic modulus–strain curve of three samples under confining pressure of 7 MPa.

become bigger as time goes on, then elasticity modulus dramatically decreases.

For the samples with same lithology, the elasticity modulus increases with confining pressure, which shows that the larger confining pressure corresponds to the upper limits of deformation resistance capacity. As shown in Table 4, comparing the value in 7 MPa with 5 MPa, the increments of elasticity modulus of the samples (solidified material, concrete material, and coal) are 31.94%, 42.98%, and 29.23%, respectively. Comparing 5 MPa with 3 MPa, the increments are 54.30%, 4.21%, and 26.50%, respectively.

(3) In Figure 10, the samples with the same lithology possess the properties that the elasticity modulus increases with confining pressure. For example, the elasticity modulus of solidified material under 3 MPa reaches the minimum value at axial strain of 0.028 m, the fractures completely develop and internal physical structures are totally damaged. The elasticity modulus under 5 MPa is 1.44 GPa, which decreases 59.65% compared with the top value. At this stage, samples own a little rigidity and are in irreversible plastic deformation stage. The emerging fractures appear slippage and samples own macroscopic deformation. In addition, the elasticity modulus under 7 MPa is 3.40 GPa, which decreases to 27.80% compared with the top value. In this phase, a little decrease in elasticity modulus shows that the sample has completed the plastic deformation stage and internal protogenesis fractures are entirely closed. Then, the new cavities appear, and samples produce plastic deformation. However, the elasticity modulus owns greater absolute value, and rock mass has a little rigidity. The elasticity modulus can be determined via the relationship between stress difference and axial strain based on Eq. (3), which represents the change rate of stress with axial strain. The integral of elasticity modulus brings the stress difference at the same time. As shown in Eq. (8), the larger elasticity modulus corresponds to larger stress difference.

$$\sigma_\Delta = \int E d\varepsilon, \tag{8}$$

$$\sigma_\Delta = \sigma_1 - \sigma_3. \tag{9}$$

According to Figure 10, it is reasonable to noting that big differences exist between the samples with the same lithology
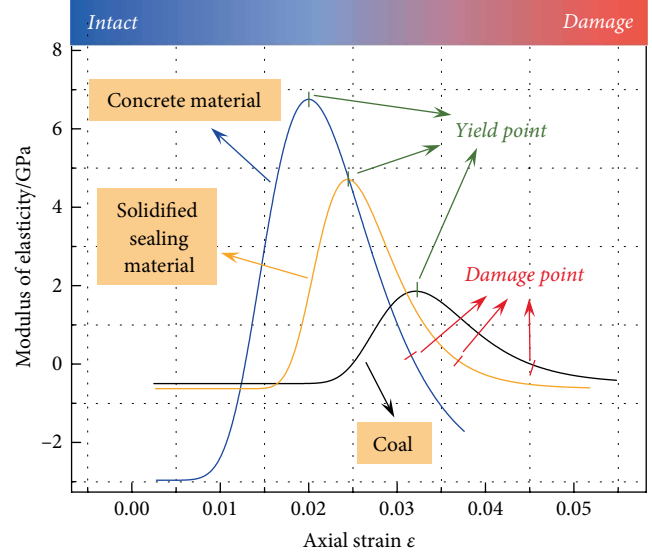
but under damage stage and failure stage. Combining the stress and strain curves in Figure 4, the phenomenon with higher confining pressure corresponds to slower declination of main stress at stress limits could be observed. One reason is irreversible physical structures change under high pressure, and emerging fractures gradually develop. Meanwhile, parts produce relative slippage, which changes from brittle failure composed of friction and fracture slippery to plastic failure consisting of relative slippage and superplastic deformation. Meanwhile, Poisson's ratio changes when the rock physical structures vary. Besides, the lateral strain trend of the samples increases. In this experiment, confining pressure kept a constant, which would lead to the lateral strain. The higher confining pressure to a certain extent prevents the radial strain of samples, which can decrease the declination of stress peak. The other reason lies in the changes of coefficient of lateral friction and the high positive stress in the lateral wall from high confining pressure which could produce large friction force that delays the axial compression deformation of samples.

(4) The inner structures and mechanical properties of the three samples are different. Among which, the compactness of solidified material is high which shows that the material owns high strength and rigidity. The concrete material is composed of gel material and aggregate, which owns a stable structure. Besides, the coal sample has a soft structure and low strength and hardness. In this study, the impacts of changes in elasticity modulus to strain on the relationship between strength and deformation of three samples under 7 MPa confining pressure were investigated. As shown in Figure 11, under the same axial strain, the elasticity modulus of concrete material firstly increases, and its elasticity modulus peak and curve inclination are also the maximum. On the contrary, the coal lies in the last. Hence, a conclusion could be made that the rigidity of the concrete material is the best, the solidified material comes second, while the coal lies in the last. This is
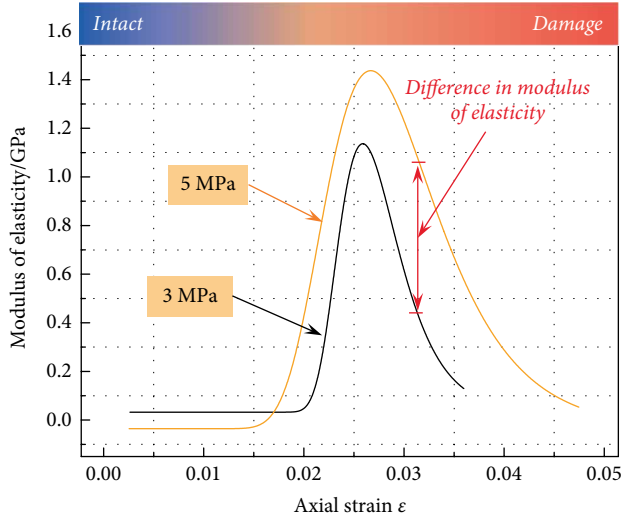
FIGURE 12: Elastic modulus–strain curve of coal samples under different confining pressures.

FIGURE 13: Relationship between axial strain and confining pressure at peak strength of sample.

because of the inner properties. It should be noted that when the elasticity modulus of the concrete material decreases to a low level which means complete damage under the control of pure axial strain, the coal still has a gap away from the peaks and lies in the deformation process. Hence, the borehole creep and rigidity decrease appear more easily for the traditional concrete material, which would cause structure damage and decrease in borehole efficiency. In the peaks, new solidified material has a clearly higher strain than that of traditional concrete material. Consequently, the new solidified material has better enduring capacities of strain. It is calculated that axial strain of peaks in the solidified material is higher than that in concrete material and the value under 7, 5, and 3 MPa are 22.25%, 31.99%, and 9.26%, respectively.

In Figure 10(a), the change of concrete material under 3 MPa and 5 MPa confining pressure are similar and tend to be the same in some parts, which is due to the inner compactness structure of the concrete material and the high inner rigidity. The slight distinction of 3 MPa to 5 MPa confining pressure cannot make a big difference to the lithology due to the rigidity. Therefore, the high similarity in the process of initial densification, elastic deformation, plastic failure, and damaging part could be observed. It can be straightly found that stress and strain curves are both near.

According to Figure 12, in the whole process, the elasticity modulus profile of confining pressure of 5 MPa is higher than that corresponds to the confining pressure of 3 MPa, which means that the rigidity and increase rate of strain difference under 5 MPa are higher than those under 3 MPa. That is mainly because the coal is soft and has many natural pores and fractures which would be gradually closed under the rising confining pressure. The corresponding rigidity and elasticity modulus naturally increase. Hence, the elasticity modulus under 5 MPa is higher.

4.4. Effects of Confining Pressure on Sample Strength and Deformation. In this experiment, the methods of controlling confining pressure and changing the axial strain to load were
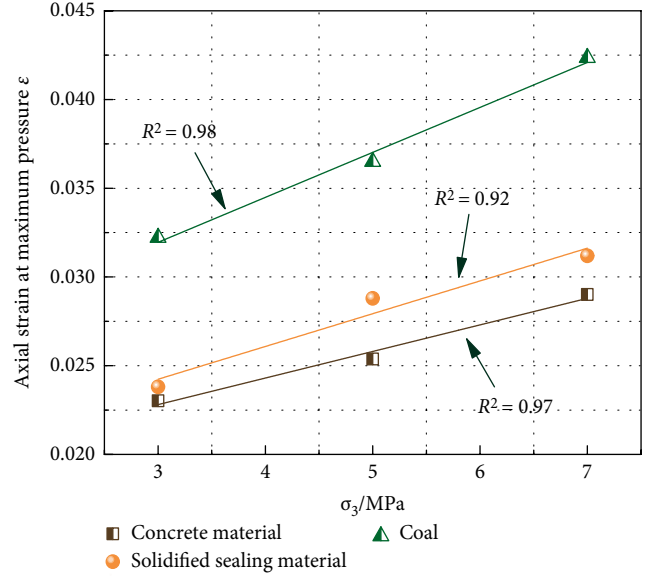
adopted. All samples experienced four stages of compaction phase, elastic phase, yield phase, and failure phase, under different confining pressures. Furthermore, the samples with the same lithology were taken from one rock sample, and owned small property difference. This proves the reliance of samples with the same lithology in three-dimensional axial experiments. Therefore, the key parameter values related to confining pressure could be the preference for practical activities of the Lu'an group company.

(1) The capacity of resisting owning attributes failure (i.e. hardness) is usually used to measure the utmost carrying limits. The axial strain in peak strength of samples represents the maximum enduring axial strain limits, which works in rigidity-analysis process. Figure 13 shows the relation between axial strain and confining pressure in peak strength. It could be directly observed that the axial strain in peak strength of three samples with different lithology gradually rises with the increase in confining pressure, which indicates that the increase in confining pressure augments the deformation-resistance capacity in the axial direction.

Compared with the concrete material and solidified material, coal has a soft structure, which means that the coal has the maximum axial strain under same confining pressure. According to Figure 13, when the confining pressure rises from 3 MPa to 7 MPa, the coal axial strain in peak strength increases 21.14% and 44.83% compared with the other two materials. It is obvious that coal has the best deformation-enduring capacity. In Figure 13, the strain curve of solidified material is higher than that of concrete material, which shows that the new solidified material has better performance in the deformation-enduring capacity and could prevent borehole creep behavior.

(2) Stress peak represents the hardness limits. Take the main stress mode of Coulomb [47] strength criterion into the equation:

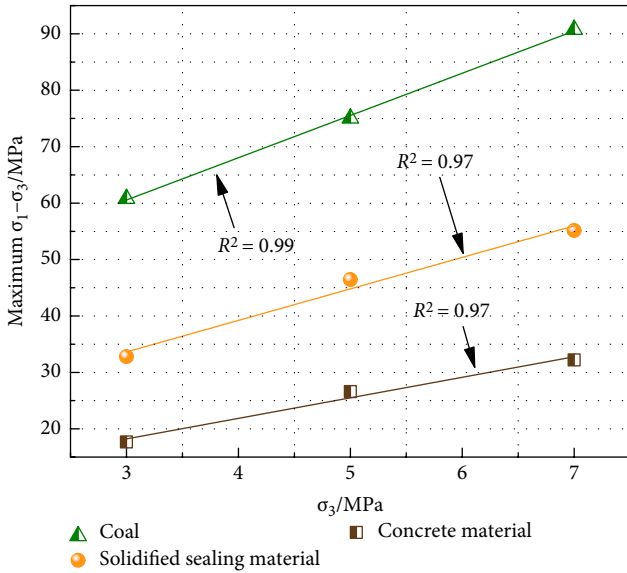$$\sigma_1 = m\sigma_3 + k, \tag{10}$$

FIGURE 14: Relationship between axial principal stress and confining pressure at peak strength of sample.
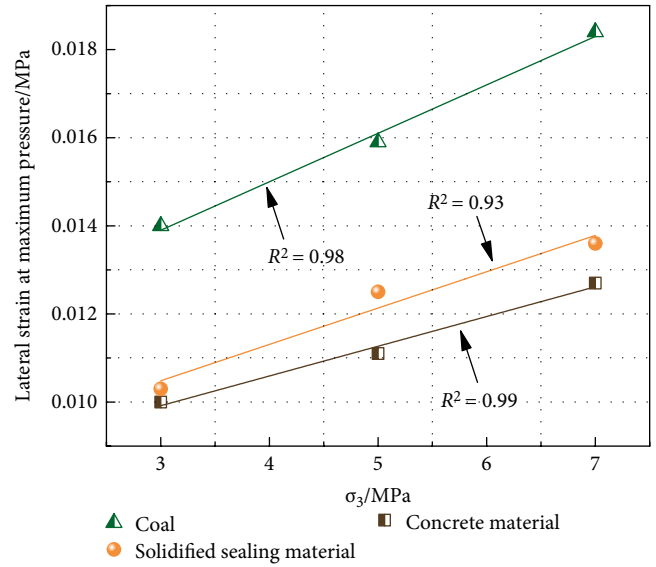
FIGURE 15: Relationship between the absolute value of side strain and confining pressure at the sample peak.

where m is the effect coefficient of confining pressure on axial stress peak, k is the sample strength on complete shearing failure under the uniaxial compression and without confining pressure. The relation of m and k could be expressed as follows:

$$m = \frac{1 + \sin \varphi}{1 - \sin \varphi}, \tag{11}$$

$$k = \frac{2C \cos \varphi}{1 - \sin \varphi}. \tag{12}$$

Based on Eqs. (11) and (12), following equations could be obtained:

$$\varphi = \arcsin \frac{m - 1}{m + 1}, \tag{13}$$

$$C = \frac{k(1 - \sin \varphi)}{2 \cos \varphi}. \tag{14}$$

According to Eq. (10), the axial strain peak σ_1 has a linear relation with confining pressure σ_3 for the specific sample. Figure 14 is the changing curve of the axial pressure peak and confining pressure, which shows that the profile parameters conform to the Coulomb strength criterion. There is a linear relation between the peak pressure and confining pressure. Besides, the existing slope shows the sensibility and great positive correlation between pressure peak and confining pressure.

(3) The lateral strain represents the lateral deformation capacity under axial pressure. The inhibition effect differs in different confining pressures. Figure 15 is the change of lateral strain with confining pressure in the peak strength of the samples. It could be clearly seen that the lateral strain of the samples in the peak rises gradually with the increase in confining pressure, which is due to the positive impact of compression
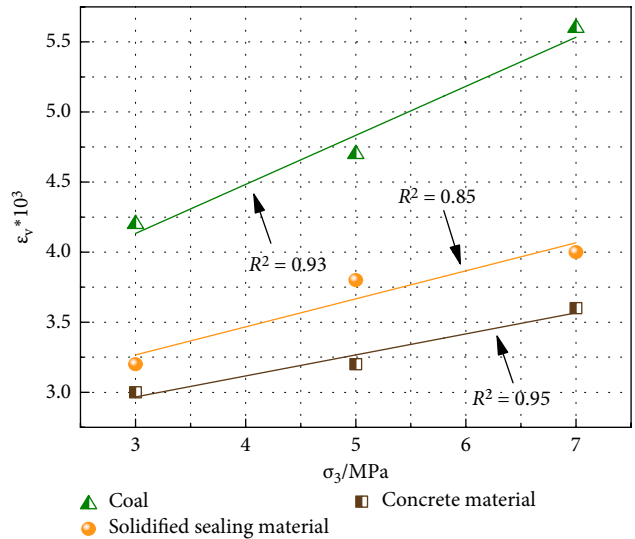
FIGURE 16: Relationship between volume strain and confining pressure at the sample peak.

on the axial capacity of enduring pressure. Based on previous analysis, the confining pressure has a positive correlation with axial peak stress and strain functions. Hence, the samples would experience higher shearing stress. Besides, the whole sample crossrange has an expansion tendency. Consequently, the lateral strain would increase with confining pressure and the trend is linear.

For three samples with different lithology but under same confining pressure, the coal has maximum lateral strain. Compared to solidified material and concrete material, the lateral strain increase of coal is 34.75% and 43.24%, respectively, which shows that the solidified material and concrete material perform well in the lateral deformation capacity.

(4) In the experiments, the sample would produce axial strain and lateral strain. Correspondingly, the volume dynamically changes, which could be proved by the change of the expansion capacity. The expansion capacity is a significant parameter among mechanical properties in the fracturing process. Figure 16 shows the change of volume strain with confining pressure in three-dimensional axial compression process. The relation could be expressed as follows:

$$\varepsilon_v = \varepsilon_1 - 2|\varepsilon_3|, \tag{15}$$

where ε_1 is the axial strain, $|\varepsilon_3|$ is the absolute value of lateral strain.

In Figure 16, the volume strain in coal peak strength is sensitive to the change of confining pressure, which is due to the soft characteristics and more natural pores than other materials. The strains in Figure 16 are positive values, which shows that the axial strain in the peak strength of coal is greatly higher than the lateral strain under the twice times peak strength and the tendency is clearer with the increase in confining pressure. As the natural pores and fractures (endogenetic fractures) divide the coal into some pieces of matrix which has numerous pores. Stress of all directions is the main reason of volume shrinkage. In macro view, when the coal experiences stress under high confining pressure, the inhibiting effect of confining pressure is stronger than the support effect of pore framework. Therefore, the volume strain of sample increases with the confining pressure.

According to the quantity relation, the volume strain in peak strength of coal is higher than that of concrete material and solidified material. The values are 31.58% and 46.87%, respectively, which shows that the coal has the best volume expansion capacity among three experimental samples.

In Figure 16, the volume strain peaks of solidified material are higher than those of concrete material under the same confining pressure, which shows that the new material has better capacity in expansion volume. When the confining pressure being 7, 5, and 3 MPa, the volume strain increase of new material is 11.11%, 18.75%, and 6.25%, respectively. Compared with the concrete material, it proves above conclusions. Meanwhile, the new solidified material could better support borehole.

5. Conclusions

(1) The pore content of all samples decreased to some extent after loading. The relative content of adsorption pores in all samples is much larger than seepage pore and fracture, and the stress sensitivity of adsorption pore is weaker than seepage pore and fracture.

(2) The content of seepage pore and fracture in the new solidified material is approximately 10.29% and 15.88% smaller than that of coal sample and concrete material, respectively. It has fewer gas migration channels, which have better performance than concrete samples in borehole sealing. The pressure sensitivity of all types of pores in the new solidified materials is weaker than that of coal samples and concrete samples, it has a slower trend of change, and its structure is more stable, which is more beneficial to drilling seals.

(3) When stress keeps the same in the range of experimental pressures, the traditional concrete material has the maximum strength, the new solidified material comes second, while the coal sample is the last. Meanwhile, when the confining pressure being constant, the concrete material has maximum peaks of elasticity modulus, the new solidified material comes second, while the coal sample is the last.

(4) While the stress is the same, the new solidified material possesses better strain-bearing capacity compared with the concrete material. This advantage could help to avoid the appearance of creep in borehole sealing section. Meanwhile, under the confining pressures of 7, 5, and 3 MPa, the stress peaks of new solidified material are 22.25%, 31.99%, and 9.26% higher than those of concrete material.

(5) In certain confining pressure, the new solidified material has superior volumetric expansion capacity after experiencing pressure. This feature could increase the volume of the borehole sealing section and improve the supporting capacity of the solidified material. At the same time, under confining pressures of 7, 5, and 3 MPa, the volume increase of the new material in stress peaks are 11.11%, 18.75%, and 6.25% higher than those of concrete material.

Data Availability

The experimental data used to support the findings of this study are available from the corresponding author upon request.

Conflicts of Interest

The authors declare that they have no conflicts of interest.

Acknowledgments

References

[1] W. Yang, B. Q. Lin, and J. T. Xu, "Gas outburst affected by original rock stress direction," *Natural Hazards*, vol. 72, no. 2, pp. 1063–1074, 2014.

[2] D. Liu, Y. Yao, D. Tang, S. Tang, Y. Che, and W. Huang, "Coal reservoir characteristics and coalbed methane resource assessment in Huainan and Huaibei coalfields, Southern North China," *International Journal of Coal Geology*, vol. 79, no. 3, pp. 97–112, 2009.

[3] K. Zhang, K. Sun, B. Yu, and R. P. Gamage, "Determination on sealing depth of in-seam boreholes for seam gas drainage based

on drilling process of a drifter," *Engineering Geology*, vol. 210, pp. 115–123, 2016.

[4] X. Zhang, G. Jiang, T. Dong, L. Wang, X. Li, and G. Wang, "An amphoteric polymer as a shale borehole stabilizer in water-based drilling fluids," *Journal of Petroleum Science and Engineering*, vol. 170, pp. 112–120, 2018.

[5] S. Hu, X. Guo, C. Li et al., "An approach to address the low concentration methane emission of distributed surface wells," *Industrial & Engineering Chemistry Research*, vol. 57, no. 39, pp. 13217–13225, 2018.

[6] S. Hu, A. Zhang, G. Feng et al., "Methane extraction from abandoned mines by surface vertical wells: a case study in China," *Geofluids*, vol. 2018, Article ID 8043157, 9 pages, 2018.

[7] C. Zhai, Z. Hao, and B. Lin, "Research on a new composite sealing material of gas drainage borehole and its sealing performance," *Procedia Engineering*, vol. 26, no. 4, pp. 1406–1416, 2011.

[8] X. Xiang, C. Zhai, Y. Xu, X. Yu, and J. Xu, "A flexible gel sealing material and a novel active sealing method for coal-bed methane drainage boreholes," *Journal of Natural Gas Science and Engineering*, vol. 26, pp. 1187–1199, 2015.

[9] A. Zhou and K. Wang, "A new inorganic sealing material used for gas extraction borehole," *Inorganic Chemistry Communications*, vol. 102, pp. 75–82, 2019.

[10] C. Zhang, B. Lin, Y. Zhou, C. Zhai, and C. Zhu, "Study on "fracturing-sealing" integration technology based on high-energy gas fracturing in single seam with high gas and low air permeability," *International Journal of Mining Science and Technology*, vol. 23, no. 6, pp. 841–846, 2013.

[11] Q. Liu, Y. Cheng, L. Yuan, Y. Fang, D. Shi, and S. Kong, "A new effective method and new materials for high sealing performance of cross-measure CMM drainage boreholes," *Journal of Natural Gas Science and Engineering*, vol. 21, pp. 805–813, 2014.

[12] Q. Zou, H. Liu, Z. Cheng, T. Zhang, and B. Lin, "Effect of slot inclination angle and borehole-slot ratio on mechanical property of pre-cracked coal: implications for ECBM recovery using hydraulic slotting," *Natural Resources Research*, 2019.

[13] Q. Zou and B. Lin, "Fluid–solid coupling characteristics of gas-bearing coal subjected to hydraulic slotting: an experimental investigation," *Energy & Fuels*, vol. 32, no. 2, pp. 1047–1060, 2018.

[14] Q. Zou, B. Lin, C. Zheng et al., "Novel integrated techniques of drilling–slotting–separation-sealing for enhanced coal bed methane recovery in underground coal mines," *Journal of Natural Gas Science and Engineering*, vol. 26, pp. 960–973, 2015.

[15] K. Zheng, X. Yang, R. Chen, and L. Xu, "Application of a capillary crystalline material to enhance cement grout for sealing tunnel leakage," *Construction and Building Materials*, vol. 214, pp. 497–505, 2019.

[16] B. Lin, F. Yan, C. Zhu et al., "Cross-borehole hydraulic slotting technique for preventing and controlling coal and gas outbursts during coal roadway excavation," *Journal of Natural Gas Science and Engineering*, vol. 26, pp. 518–525, 2015.

[17] Z. Cheng, Y. Xu, N. Guanhua, L. Min, and H. Zhiyong, "Microscopic properties and sealing performance of new gas drainage drilling sealing material," *International Journal of Mining Science and Technology*, vol. 23, no. 4, pp. 475–480, 2013.

[18] F. Yan, B. Lin, C. Zhu et al., "A novel ECBM extraction technology based on the integration of hydraulic slotting and hydraulic fracturing," *Journal of Natural Gas Science and Engineering*, vol. 22, pp. 571–579, 2015.

[19] Q. Li, B. Lin, C. Zhai et al., "Variable frequency of pulse hydraulic fracturing for improving permeability in coal seam," *International Journal of Mining Science and Technology*, vol. 23, no. 6, pp. 847–853, 2013.

[20] H. Jonsson and G. Frenning, "Investigations of single microcrystalline cellulose-based granules subjected to confined triaxial compression," *Powder Technology*, vol. 289, pp. 79–87, 2016.

[21] Z. Geng, M. Chen, Y. Jin et al., "Experimental study of brittleness anisotropy of shale in triaxial compression," *Journal of Natural Gas Science and Engineering*, vol. 36, pp. 510–518, 2016.

[22] M. Chabannes, F. Becquart, E. Garcia-Diaz, N.-E. Abriak, and L. Clerc, "Experimental investigation of the shear behaviour of hemp and rice husk-based concretes using triaxial compression," *Construction and Building Materials*, vol. 143, pp. 621–632, 2017.

[23] E. Öztekin, S. Pul, and M. Hüsem, "Experimental determination of Drucker-Prager yield criterion parameters for normal and high strength concretes under triaxial compression," *Construction and Building Materials*, vol. 112, pp. 725–732, 2016.

[24] J. Gong and J. Liu, "Effect of aspect ratio on triaxial compression of multi-sphere ellipsoid assemblies simulated using a discrete element method," *Particuology*, vol. 32, no. 3, pp. 49–62, 2017.

[25] J. Dong, Y. Cheng, B. Hu, C. Hao, Q. Tu, and Z. Liu, "Experimental study of the mechanical properties of intact and tectonic coal via compression of a single particle," *Powder Technology*, vol. 325, pp. 412–419, 2018.

[26] Y. Tan, Z. Pan, J. Liu, X.-T. Feng, and L. D. Connell, "Laboratory study of proppant on shale fracture permeability and compressibility," *Fuel*, vol. 222, pp. 83–97, 2018.

[27] Z. Pan, L. D. Connell, and M. Camilleri, "Laboratory characterisation of coal reservoir permeability for primary and enhanced coalbed methane recovery," *International Journal of Coal Geology*, vol. 82, no. 3, pp. 252–261, 2010.

[28] T. Liu, B. Lin, and W. Yang, "Impact of matrix–fracture interactions on coal permeability: model development and analysis," *Fuel*, vol. 207, pp. 522–532, 2017.

[29] S. Li, D. Tang, Z. Pan, H. Xu, and W. Huang, "Characterization of the stress sensitivity of pores for different rank coals by nuclear magnetic resonance," *Fuel*, vol. 111, pp. 746–754, 2013.

[30] Y. Meng and Z. Li, "Experimental comparisons of gas adsorption, sorption induced strain, diffusivity and permeability for low and high rank coals," *Fuel*, vol. 234, pp. 914–923, 2018.

[31] Z. Wang, Y. Cheng, K. Zhang et al., "Characteristics of microscopic pore structure and fractal dimension of bituminous coal by cyclic gas adsorption/desorption: an experimental study," *Fuel*, vol. 232, pp. 495–505, 2018.

[32] H. Guo, L. Yuan, Y. Cheng, K. Wang, and C. Xu, "Experimental investigation on coal pore and fracture characteristics based on fractal theory," *Powder Technology*, vol. 346, pp. 341–349, 2019.

[33] S. Li, D. Tang, H. Xu, and Z. Yang, "The pore-fracture system properties of coalbed methane reservoirs in the Panguan Syncline, Guizhou, China," *Geoscience Frontiers*, vol. 3, no. 6, pp. 853–862, 2012.

[34] Z. Zhang, Y. Qin, X. Zhuang, G. Li, and X. Wang, "Poroperm characteristics of high-rank coals from Southern Qinshui Basin by mercury intrusion, SEM-EDS, nuclear magnetic resonance

and relative permeability analysis," *Journal of Natural Gas Science and Engineering*, vol. 51, pp. 116–128, 2018.

[35] H. Zhu, Y. Ju, Y. Qi, C. Huang, and L. Zhang, "Impact of tectonism on pore type and pore structure evolution in organic-rich shale: implications for gas storage and migration pathways in naturally deformed rocks," *Fuel*, vol. 228, pp. 272–289, 2018.

[36] J. Zhang, C. Wei, J. Zhao, W. Ju, Y. Chen, and L. S. Tamehe, "Comparative evaluation of the compressibility of middle and high rank coals by different experimental methods," *Fuel*, vol. 245, pp. 39–51, 2019.

[37] Y. Liu, Y. Zhu, and S. Chen, "Effects of chemical composition, disorder degree and crystallite structure of coal macromolecule on nanopores (0.4–150 nm) in different rank naturally-matured coals," *Fuel*, vol. 242, pp. 553–561, 2019.

[38] L. Qin, C. Zhai, S. Liu, J. Xu, G. Yu, and Y. Sun, "Changes in the petrophysical properties of coal subjected to liquid nitrogen freeze-thaw—a nuclear magnetic resonance investigation," *Fuel*, vol. 194, pp. 102–114, 2017.

[39] S. Khatibi, M. Ostadhassan, Z. Xie et al., "NMR relaxometry a new approach to detect geochemical properties of organic matter in tight shales," *Fuel*, vol. 235, pp. 167–177, 2019.

[40] A. F. Constantino, D. C. Cubides-Román, R. B. dos Santos et al., "Determination of physicochemical properties of biodiesel and blends using low-field NMR and multivariate calibration," *Fuel*, vol. 237, pp. 745–752, 2019.

[41] Y. Yao, D. Liu, Y. Che, D. Tang, S. Tang, and W. Huang, "Petrophysical characterization of coals by low-field nuclear magnetic resonance (NMR)," *Fuel*, vol. 89, no. 7, pp. 1371–1380, 2010.

[42] J. Zhang, C. Wei, W. Ju et al., "Stress sensitivity characterization and heterogeneous variation of the pore-fracture system in middle-high rank coals reservoir based on NMR experiments," *Fuel*, vol. 238, pp. 331–344, 2019.

[43] H. Li, S. Shi, J. Lu, Q. Ye, Y. Lu, and X. Zhu, "Pore structure and multifractal analysis of coal subjected to microwave heating," *Powder Technology*, vol. 346, pp. 97–108, 2019.

[44] L. Qin, C. Zhai, S. Liu, J. Xu, S. Wu, and R. Dong, "Fractal dimensions of low rank coal subjected to liquid nitrogen freeze-thaw based on nuclear magnetic resonance applied for coalbed methane recovery," *Powder Technology*, vol. 325, pp. 11–20, 2018.

[45] A. Pineau, A. A. Benzerga, and T. Pardoen, "Failure of metals I: brittle and ductile fracture," *Acta Materialia*, vol. 107, pp. 424–483, 2016.

[46] M. Mohamadi and R. G. Wan, "Strength and post-peak response of Colorado shale at high pressure and temperature," *International Journal of Rock Mechanics and Mining Sciences*, vol. 84, pp. 34–46, 2016.

[47] D. A. Sun, Y. P. Yao, and H. Matsuoka, "Modification of critical state models by Mohr-Coulomb criterion," *Mechanics Research Communications*, vol. 33, no. 2, pp. 217–232, 2006.

WILEY | Hindawi

Research Article

Study on Flame Spread Characteristics of Flame-Retardant Cables in Mine

Gao Ke [iD],[1,2] **Liu Zimeng,**[1,2] **Jia Jinzhang,**[1,2] **Liu Zeyi,**[1,2] **Aiyiti Yisimayili,**[1,2] **Qi Zhipeng,**[1,2] **Wu Yaju,**[3] **and Li Shengnan**[1,2]

[1]*College of Safety Science and Engineering, Liaoning Technical University, Liaoning, Huludao 125105, China*
[2]*Key Laboratory of Mine Thermo-Motive Disaster and Prevention, Ministry of Education, Huludao 125105, China*
[3]*School of Safety Engineering, Shenyang Aerospace University, Shenyang 110136, China*

Correspondence should be addressed to Gao Ke; gaoke@lntu.edu.cn

Polymer combustion is an important factor in mine fires. Based on the actual environment in a mine tunnel, a cable combustion experiment platform was established to study the regularities of the cable fire spread speed and smoke temperature under different conditions, including various fire loads and ventilation speeds. The flame change and molten dripping behaviour during the fire spread process were also analyzed. The experimental results show that the flame-retardant cable can be ignited and continuously burnt at a certain wind speed, but the combustion can be restrained at high wind speed. The combustion speed of the flame-retardant cable is affected by the fire load and ventilation speed. The combustion droplets can change the shape of the flame, which can consequently ignite other combustible materials. The analysis of the experimental results provides an important basis for the prevention of tunnel fires.

1. Introduction

In recent years, polymer materials, such as cables and belts, have been widely used in mines [1]. As the main carrier of electric energy and information transmission, the cables are widely distributed in the mine. The cables are made up of conductors, insulators, fillers, wraps, and sheaths, and the most common materials for the cable sheath in China are chloroprene rubber (CR), polyvinyl chloride (PVC), polyethylene (PE), and chlorinated polyethylene (CPE), etc. While the cable has the problems of overload, short circuit, and other faults, it may cause fire and explosion accidents and the use of polymer materials increases the fire risk of the workplace [2]. With the special mine environment, the tunnel belongs to the semienclosed space, the structure of which is very complicated [3], and the cables are arranged in every tunnel. Once the cables catch fire in the tunnel, the poisonous and harmful gases from the burning cables will flow across the downstream area, threatening the miner's life safety [4, 5]. For the reasons mentioned above, the "coal

mine safety regulations" promulgated by China stipulates that "fire-retardant cables for safety signs of coal mine products must be selected underground." However, fire-retardant cables are not noncombustible, which can be burnt under certain circumstances [6]. For example, ten miners died in the fire-retardant cable fire which happened in the Chengcheng Sulfur Mine of Shanxi Province.

At present, domestic and international scholars studying cable polymers in tunnels are mainly divided into two parts. Some established the cable combustion experiment platform according to the actual environment of the tunnel, and the char length of cables covered with coating was investigated under different fire loads and ventilation conditions. Li [7] established a cable fire model in various environments to analyze the spread of cable fires. Carcillo [8] studied the fire behaviour of electrical cables in the cone calorimeter and the influence of cables' structure and layout. Xu [6] studied the combustion and flame-retardant characteristics of PVC-sheathed cables. Liang [9] focused on cable fire spread and smoke temperature distribution in a T-shaped utility tunnel.

Rickard [10] analyzed the fire behaviour involving multiple fires in a mine drift with longitudinal ventilation. The other scholars used FDS software to simulate the occurrence of cable fires, analyzing the changes of temperature field [11], smoke flow field [12, 13], and temperature with the changes of the fire source power in different types of tunnels [14–17]. However, few scholars are committed to cable fire spread and much less attention is paid to the fire load, impact of ventilation speed on flame shape, influence of fire spread speed in a cable fire, and melting and dripping produced by the polymer as the combustible is heated.

In this paper, the role of the cable layout and air ventilation on the fire behaviour of a series of flame-retardant cable which was used in the mine of China was thoroughly investigated. The study involves the flame spread processes of one and two arrangement of cables under different wind speed conditions.

2. Experiment Design

The tunnel model (see Figure 1), which opens at both ends, has dimensions of $3\,m \times 0.26\,m \times 0.26\,m$ (length $\times$ width $\times$ height). The interior of the box is made of asbestos boards with certain thermal insulation, and fireproof glass is installed on the side as the observation window. A cable bridge with a length of 3 m and a width of 0.2 m is placed in the tunnel divided into two layers, and the lower layer and the upper layer are at heights of 0.03 and 0.13 m from the bottom, respectively.

A layer of thermocouples is arranged along the central line of the tunnel to measure the temperature. The upper five thermocouples A1–A5, 0.15 m high from the bottom, are 1, 1.25, 1.5, 1.75, and 2 m away from the air inlet, respectively. The probe is located right above the cable, and the data acquisition frequency of thermocouples is 5 s each time.

Cable fires in the tunnel are mainly caused by external ignition or short circuits, both of which occur in the presence of a stable heat source. In this study, the experimental fire source is the burning pine and the fuel is diesel oil. The ignition source is located 1 m away from the air inlet to allow observation of the combustion process of the cable.

The mass loss in the fire spread process is measured by an electronic balance with a measurement range of 2000 g and an accuracy of 0.01 g (WT C20002 series). The mass loss rate is obtained by further data processing.

In the experiment, to improve ventilation, an axial fan (SFG 3-2) is connected with a ventilation pipe with a length of 1 m. In addition, high-speed photography (Sony ILCE-5100L APS-C) is set 1 m in front of the tunnel model,which is used to record the flame spread speed, flame height, and flame spread trace of cable combustion in the tunnel.

According to the national standard JB/T8735.2-2016, the experimental materials (see Figure 2) are flame-retardant cables (type3 × 2.5) with a diameter of 11 mm, whose sheath is ethylene propylene diene rubber-insulated. Single and double cables with lengths 1 m are selected and built in the bridge frame. Once the cable is ignited, the fire source will be removed. By changing the fire load and wind speed, the combustion speed and the temperature at each measuring point, as well as flame spread trace, are measured to obtain the variation of the cable fire. The results are used to guide the fire prevention design of the tunnel cable.

3. Results and Discussion

3.1. Heat Release Rate Analysis of the Cable. The heat release rate of the solid combustible, an important parameter to measure the fire hazard, is the heat released by the combustion material in unit time. In the present study, 100 g sample cables were burned on an electronic balance. The size of the confined space is $175\,mm \times 150\,mm \times 90\,mm$. Both sides of this space are ventilated with the flow rate of air $2\,m^3/min$. The pump is installed in the pipeline, and fresh air is added from the environment at the bottom of the experiment room. The cable sample is ignited, and the external heat flux is $25\,KW/m^2$. When the cable catches fire, remove the external heat flux. The dynamic data of cable mass are recorded by an electronic balance at 5 s intervals, thus the mass loss rate can be obtained. Finally, the cable heat release rate is calculated by the following equation:

$$Q = \alpha m q, \tag{1}$$

where Q is the heat release rate, kW; α is the combustion efficiency factor of the combustible ($\alpha = 1$ for complete combustion; α usually ranges from 0.3 to 0.9); m is the mass loss rate of the combustible, kg/s; and q is the average calorific value of the combustible, kJ/kg. The combustion heat value of rubber is 35×10^3 kJ/kg.

Figure 3 shows that the heat release rate of the rubber cable sample with a airflow rate of $2\,m^3/min$. When the temperature reaches a certain level, the top layer of rubber begins to crack, producing volatile gas which is ignited to a certain concentration. Then, the heat release rate increased sharply in a short time and reached its peak value as pyrolysis combustible gas increases. With the supply of air, the cable sheath is in contact with oxygen constantly and the heat release rate enters a steady stage, making the combustion continue.

3.2. Gas Temperature Changes in the Combustion Progress. The fire gas temperature refers to the airflow temperature measured in the middle of the section as the representative temperature in the tunnel. A1–A5 temperature curves are, respectively, represented by different colour curves. Figures 4 and 5 show that the oxygen supply for the combustion in the tunnel is more sufficient with an 11 Hz fan. The temperature in the developing stage is relatively stable, while the inflection point in the attenuation stage is also obvious.

The fire gas temperatures of A1–A5 (see Figure 5) with the double cable are higher than their corresponding values with the single cable (see Figure 4). The maximum fire gas temperatures of the single cable and double cable are 170°C–180°C and 400°C–500°C, respectively.

3.3. Flame Spread Speed. Figure 6 presents the variation curves of cable flame speed under different fire loads with a
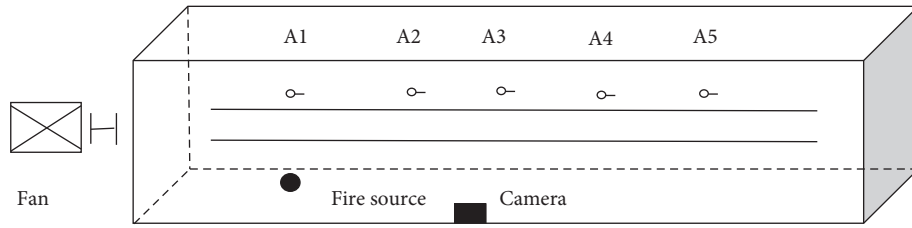
Figure 1: Tunnel platform.

Figure 2: The image of the cable sample.
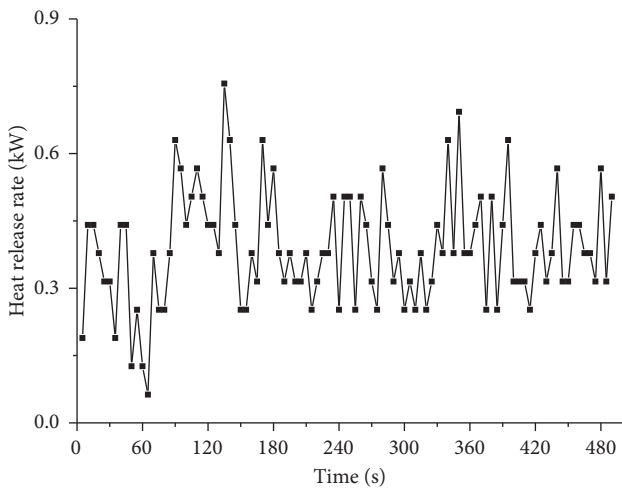
Figure 3: Heat release rate of the rubber cable sample with an airflow rate of $2 \, m^3/min$.

Figure 4: Temperature curves in the tunnel with a single cable with a fan frequency of 11 Hz.
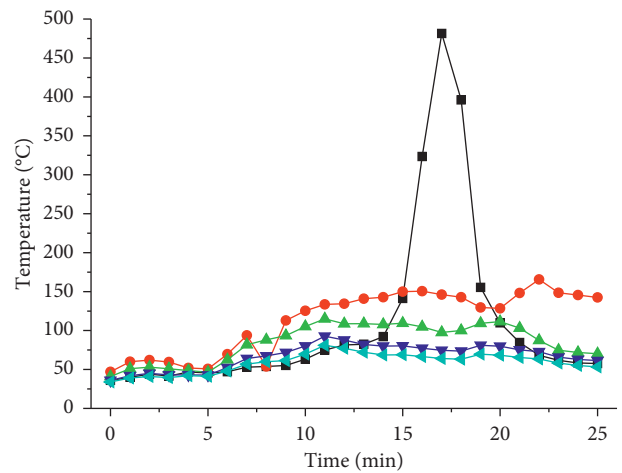
Figure 5: Temperature curves in the tunnel with a double cable with a fan frequency of 11 Hz.

fan frequency of 11 Hz. According to the test results, the flame speed of the cable increases with the fire load. This is because, in a confined space, heat released by a large number of cables is easy to gather and the cross-radiation among cables is obvious and can preheat the unburned cables and facilitate their combustion.

Moreover, as the combustion spreads continuously, the flame speed decreases and an inflection point appears, indicating that the flame in the binding joint or the lap joint will also affect the flame combustion speed.

FIGURE 6: Flame spread curve of different cable with a fan frequency of 11 Hz.

When the fan frequency increases to 15 Hz, the combustion spread length keeps decreasing until the fire is extinguished, demonstrating that excessively high wind speed inhibits combustion. This is mainly due to the airflow cooling effect which can produce disturbance to the cable flame. As a result, the obtained heat of the unburned area decreases and the flame speed slows down. The cable fire spread length also decreases accordingly.

3.4. Characteristic Analysis of Flame Spread. In the experiment, the flame spread processes of single cable and double cable are recorded by high-speed camera. Through observing, it can be found that the combustion begins when the thermal contact temperature from the ignition source is within the ignition limit and the 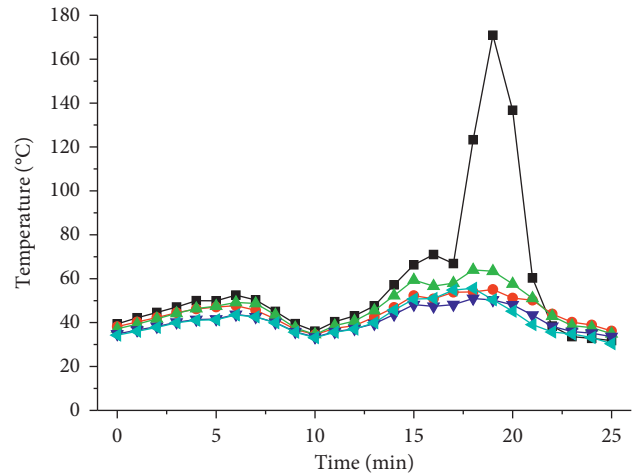temperature is higher than the ignition point. Figure 7 presents the flame spread images of the cable combustion under no wind conditions. The flame shape varies with time: it changes from single-peak fire to double-peak, then to triple-peak, while the length of flame spread keeps increasing.

With increasing smoke in the tunnel, the contact between the cable and oxygen is disturbed. One hundred and forty three seconds after the combustion starts, it enters the decaying stage and will be extinguished at 202 s. It can be concluded that the rubber cable keeps burning due to the thermal decomposition of the heated combustible. As long as the heat supply to the cable is sufficient to sustain the rate of polymer degradation required by the flame, the combustion will continue, otherwise, the flame will die out.

Figure 8 presents the flame spread images of the single cable combustion with the fan frequency of 11 Hz. The flame burns along the wind direction at this fan frequency. At 129 s, part of the heat energy generated by the gas 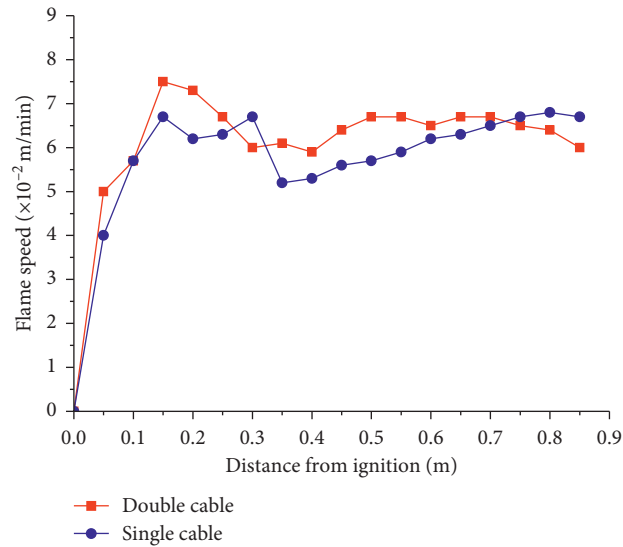flame flows to the unburned area, causing thermal decomposition of the polymer. The combustible gas produced by the thermal decomposition then combines with oxygen in the air, which promotes the combustion flame spread without interruption.

At 311 s, the flame is affected by the temperature and pressure gradient in the tunnel as well as the throttle effect on the downwind side of the fire source. Fresh air flows to the fire source on the bottom of the tunnel along the wind direction, while the smoke flow generated by the fire source flows reversely on the ceiling of the tunnel on the upwind side and rolls back to the fire source. The backflow smoke can make the combustibles on the windward side catch fire. Meanwhile, the rolling smoke flow in the tunnel may induce a gas explosion when it mixes with fresh air on the windward side of the fire source and flows back to the fire source again.

The molten appears at 1244 s. As the burning molten gradually detaches from the wire, the cable flame jumps wildly. The droplet separated from the cable appears to be burnt as it falls off from the cable. At this dropping moment, the flame above the cable becomes thinner and longer and the flame volume decreases obviously [18–20].

Figure 9 shows the flame spread images of the double cable combustion with the fan frequency of 11 Hz. At 64 s, the fire enters the developing stage. The heat generated by the double cable accumulates so that the flame height and fire spread speed are significantly faster than those in the scenario with the single cable.

The temperature of the heated cable increases drastically at 449 s. Since the temperature is higher than the melting temperature or viscous flow temperature, the cable will be gradually softened until the molten flows at 452 s. This is due to the breakdown of the thermoplastic polymer which makes
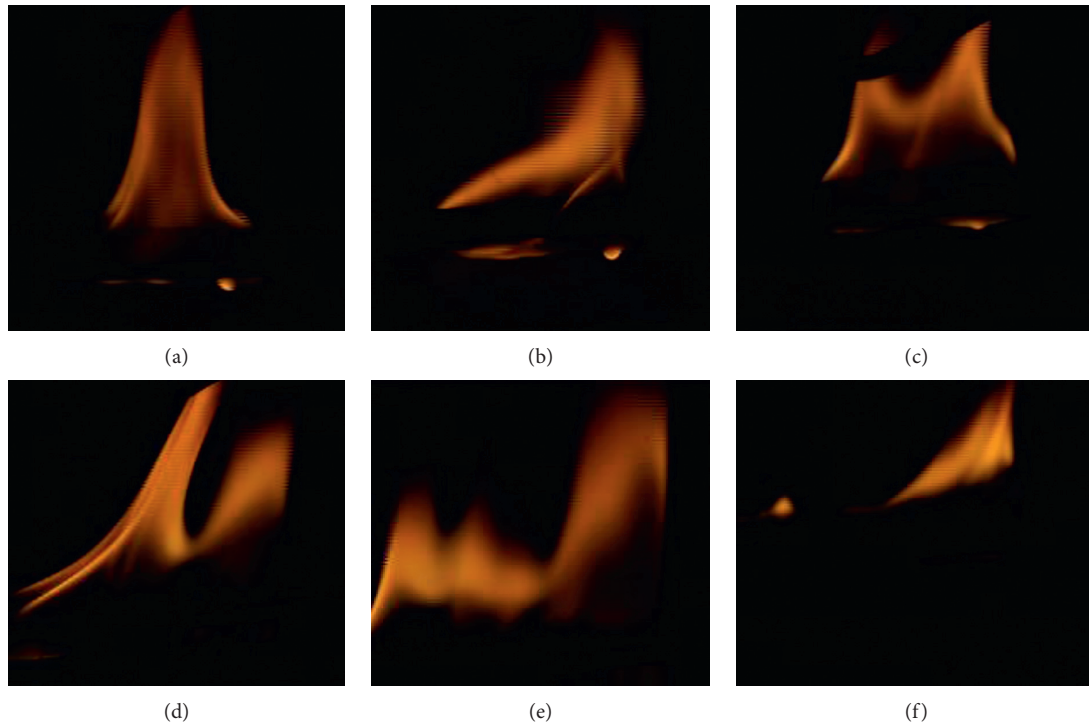
FIGURE 7: Images of flame spread under calm condition. (a) $t = 4$ s, (b) $t = 8$ s, (c) $t = 18$ s, (d) $t = 43$ s, (e) $t = 67$ s, and (f) $t = 143$ s.

FIGURE 8: Images of a single cable flame spread at a fan frequency of 11 Hz. (a) $t = 129$ s, (b) $t = 131$ s, (c) $t = 311$ s, (d) $t = 1205$ s, (e) $t = 1244$ s, and (f) $t = 1277$ s.

its molecular weight and viscosity decrease. Therefore, more and more molten drops or melt were produced. The droplet has a higher temperature after a long-distance drop, which can ignite other combustibles. The scope of the fire may expand if it is not dealt with, causing the rapid development of fire and serious consequences.
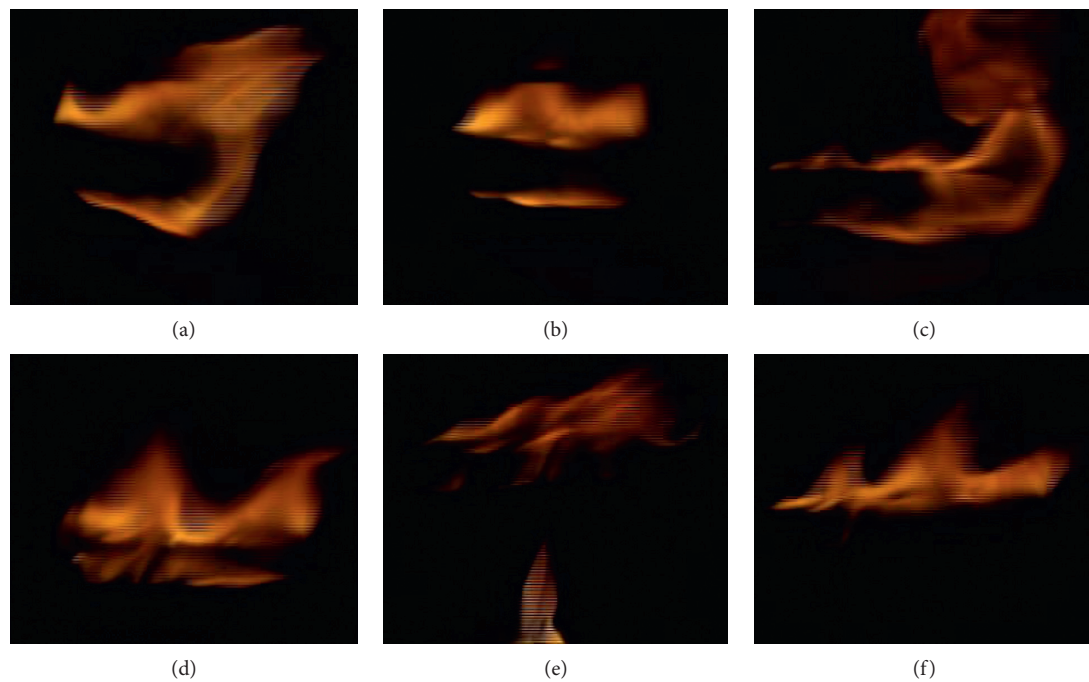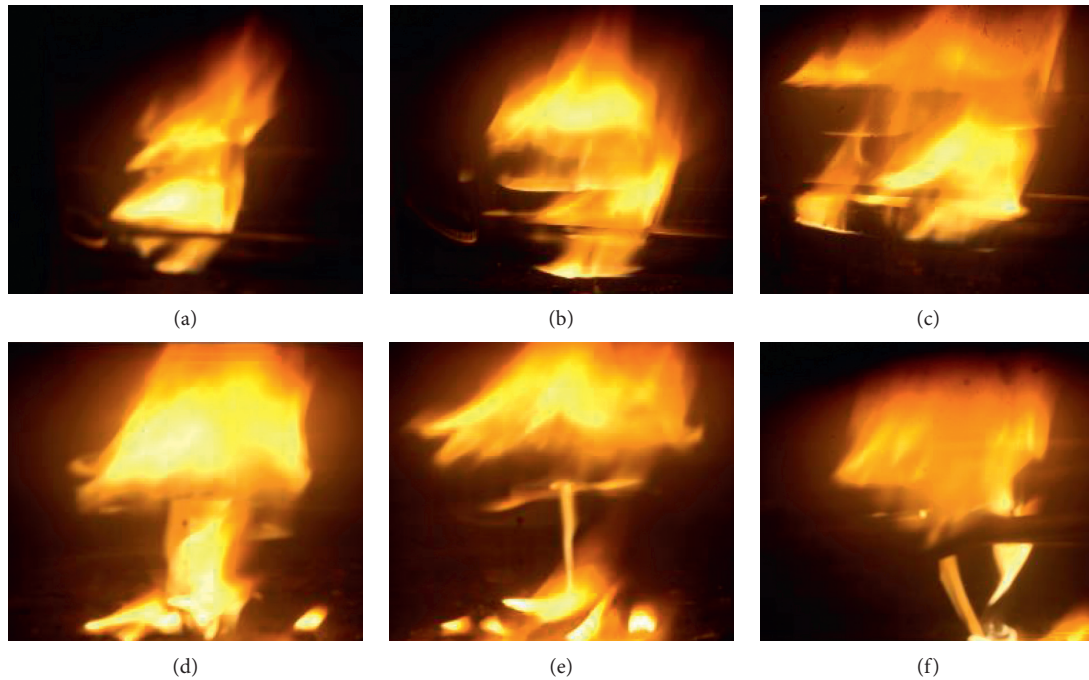
(a) (b) (c)

(d) (e) (f)

Figure 9: Images of double cable flame spread at a fan frequency of 11 Hz. (a) $t = 64$ s, (b) $t = 111$ s, (c) $t = 175$ s, (d) $t = 449$ s, (e) $t = 452$ s, and (f) $t = 744$ s.

4. Conclusion

(1) The heated flame-retardant cable can be decomposed and catch fire. Under certain wind speed conditions, partial heat generated by the flame gas flows to the unburned areas so that the polymer in these areas will be decomposed and start burning. The wind speed keeps increasing and suppresses the combustion until the fire is extinguished. As a result, the wind speed can affect the cable fire spread.

(2) In the combustion process, the cable exhibits molten flow phenomena, producing a large amount of molten with the change in the flame shape. The melting drops with a higher temperature after the long-distance travel can ignite other combustibles.

(3) The flame is affected by the temperature and pressure gradient in the tunnel as well as the throttle effect on the downwind side of the fire source. The backflow smoke phenomenon is produced. Meanwhile, the smoke flow rolling back in the tunnel mixes with fresh air on the upwind side of the fire source and flows back to the fire source again, which may induce a gas explosion.

Data Availability

The figure data in this paper used to support the findings of this study may be released upon application to the College of Safety Science and Engineering of Liaoning Technical University, who can be contacted with the corresponding author Gao Ke, and the E-mail is gaoke@lntu.edu.cn.

Conflicts of Interest

The authors declare that there are no conflicts of interest regarding the publication of this paper.

Acknowledgments

References

[1] T. F. He, W. H. Wang, H. F. Mi et al., "Comprehensive evaluation of fire risk of three polymeric materials based on CONE," *Industrial Safety and Environmental Protection*, vol. 44, no. 10, pp. 5–19, 2018.

[2] Z. M. Luo, B. Su, Q. Li et al., "Micromechanism of the initiation of a multiple flammable gas explosion," *Energy & Fuels*, vol. 33, no. 8, pp. 7738–7748, 2019.

[3] K. Gao, L. J. Deng, J. Liu et al., "Study on mine ventilation resistance coefficient inversion based on genetic algorithm," *Archives of Mining Sciences*, vol. 4, pp. 813–826, 2018.

[4] W. Cheng, X. Hu, J. Xie, and Y. Zhao, "An intelligent gel designed to control the spontaneous combustion of coal: fire prevention and extinguishing properties," *Fuel*, vol. 210, pp. 826–835, 2017.

[5] X. Ren, X. Hu, D. Xue et al., "Novel sodium silicate/polymer composite gels for the prevention of spontaneous combustion of coal," *Journal of Hazardous Materials*, vol. 371, pp. 643–654, 2019.

[6] L. N. Xu, Z. C. Shi, and D. Wu, "Experimental study of typical electric cables on cone calorimeter," *Journal of Safety and Environment*, vol. 12, no. 5, pp. 210–214, 2012.

[7] L. W. Ting, *Numerical Simulation of Integrated Pipe and Cable Fire*, Capital University of Economics and Business, Beijing, China, 2012.

[8] M. Carcillo, A. S. Caro, R. Sonnier et al., "Fire behaviour of electrical cables in cone calorimeter: influence of cables structure and layout," *Fire Safety Journal*, vol. 99, pp. 12–21, 2018.

[9] K. Liang, X. F. Hao, W. G. An et al., "Study on cable fire spread and smoke temperature distribution in T-shaped utility tunnel," *Case Studies in Thermal Engineering*, vol. 14, pp. 1–10, 2019.

[10] H. Rickard, "Fire behaviour of multiple fires in a mine drift with longitudinal ventilation," *International Journal of Mining Science and Technology*, vol. 29, no. 2, pp. 245–254, 2019.

[11] Y. Niu and W. Li, "Simulation study on value of cable fire in the cable tunnel," *Procedia Engineering*, vol. 43, pp. 569–573, 2012.

[12] T. Beji and B. Merci, "Numerical simulations of a full-scale cable tray fire using small-scale test data," *Fire and Materials*, vol. 43, no. 5, pp. 486–496, 2019.

[13] D. Yang, L. H. Hu, R. Huo et al., "Effects of longitudinal air flow on smoke stratification in channel fire," *Journal of Combustion Science and Technology*, vol. 16, no. 3, pp. 252–256, 2010.

[14] K. Shimizu, M. Kikuchi, N. Hashimoto, and O. Fujita, "A numerical and experimental study of the ignition of insulated electric wire with long-term excess current supply under microgravity," *Proceedings of the Combustion Institute*, vol. 36, no. 2, pp. 3063–3071, 2017.

[15] S.-h. Min and B.-j. Song, "A study on ignition and fire risks of electric heat wire," *Journal of the Korea Safety Management and Science*, vol. 17, no. 4, pp. 113–121, 2015.

[16] M. Siemon, O. Riese, B. Forell, D. Krönung, and W. Klein-Heßling, "Experimental and numerical analysis of the influence of cable tray arrangements on the resulting mass loss rate and fire spreading," *Fire and Materials*, vol. 43, no. 5, pp. 497–513, 2019.

[17] Y. E. Ze and L. Lei, "Temperature field and smoke flow of fire in L-type cable tunnel," *Fire Science and Technology*, vol. 37, no. 1, pp. 37–41, 2018.

[18] X. K. Li, W. F. Du, and Z. S. Xu, "Efficiency of fire-retardant cable coating in cable tunnel fire test," *Journal of Nanjing University of Technology (Natural Science Edition)*, vol. 33, no. 2, pp. 38–41, 2011.

[19] W. Plumecocq, L. Audouin, and P. Zavaleta, "Horizontal cable tray fire in a well-confined and mechanically ventilated enclosure using a two-zone model," *Fire and Materials*, vol. 6, pp. 530–542, 2019.

[20] H. He, *Molten Thermoplastic Dripping Behavior Induced by Dame Propagation over Energized Polyethylene-Insulated Wires*, University of Science and Technology of China, Anhui, China, 2017.

Research Article

Development Performance and Pressure Field Evolution of ASP Flooding

Junjian Li [ID], Hao Wang [ID], Jinchuan Hu, Hanqiao Jiang, Rongda Zhang, and Lihui Tang

State Key Laboratory of Petroleum Resources and Prospecting, China University of Petroleum (Beijing), Beijing 102249, China

Correspondence should be addressed to Junjian Li; junjian@cup.edu.cn

ASP (alkali-surfactant-polymer) is acknowledged as an effective technology to improve the oil recovery. The microscopic displacement efficiency and macroscopic sweep efficiency have been discussed in detail for the past few years. However, development performance, especially pressure characteristics, needs to be further studied. This paper aims to explore the pressure evolution performance during ASP flooding, of which the results will shed light on development characteristics of ASP flooding. The study on ASP flooding pressure field development is conducted by laboratory and numerical methodology. A large sandpack laboratory model with vertical heterogeneous layers is used to monitor pressure performance during the ASP flooding. With the help of interpolation methods, a precise and intuitive pressure field is obtained based on pressure data acquired by limited measurement points. Results show that the average formation pressure and its location are changing all the time in the whole process. In addition, the influence of heterogeneity and viscosity on recovery and pressure is also probed in this paper. We built a numerical simulation model to match the experiment data considering the physical and chemical alternation in ASP flooding. Also, response surface methodology (RSM) is adopted to obtain the formula between pressure functions and influencing factors.

1. Introduction

After a long period of natural depletion and waterflooding, there are still considerable proportions of crude oil that are untapped in the reservoir, especially for heterogeneous reservoirs, leaving about 50%~67% original oil in place [1]. Therefore, how to enhance oil recovery (EOR) is the key to develop the remaining oil left in the reservoir and increase oil production rate. Chemical flooding technology has the potential to play an important role in unlocking the hydrocarbon resources left behind after natural depletion and waterflooding stages in mature reservoirs [2–4]. Now that quantities of physical and chemical reactions between fluid and rocks exit in the reservoir [3, 5–8], there are still many problems in the process of chemical flooding. Many researchers have studied the effects of salinity [9], dehydration [10], shear stress [11], etc. on production and developed many new chemical agents. Zhao et al. [9] developed a new antisalt polymer that was prepared by produced water and was successfully applied in low-permeability reservoirs. They

found that this new polymer outperformed HPAM in terms of viscosity, stability, resistant factor, and core displacement experiment. Zhao et al. [10] also studied the effect of composition and brine concentration on gel compression-induced dehydration. The results showed that damage occurred inside the gel after compression due to some microscopic fractures.

Alkali-surfactant-polymer (ASP) flooding, as a promising chemical EOR technology, has greatly attracted attention in recent years [12–14]. For example, the ASP flooding test conducted in Daqing Oilfield confirmed that about 20% additional OOIP was recovered [15]. The ASP flooding mechanism includes the individual mechanism of each of its components and their synergism. Polymer is responsible for improving mobility ratio and increasing the sweep efficiency, while diminishing viscous fingering issues and creating a smooth flood front in the reservoir [16]. Another mechanism of the polymer is that there is a large normal stress exerted on the residual oil droplets and oil films due to its high viscosity. Thus, the residual oil

saturation will decrease; in other words, the microscopic displacement efficiency will increase [17]. In addition, as for heterogeneous reservoirs, polymer plays an important role in profile control and increases the vertical sweep efficiency. The mechanism of surfactant is low interfacial tension (IFT) effect. Waterflooding becomes ineffective as the oil is trapped in the small pore by capillary forces; therefore, the residual oil appears. And the indicator that characterizes whether the residual oil can flow is defined as capillary number (Nc). The larger the capillary number, the more easily the residual oil flows. After the waterflooding stage, the capillary number is estimated to be about 10^{-7} [18]. An increase in the capillary number to around 10^{-5} is required to produce additional oil after waterflooding [19, 20]. And the surfactant in ASP can practically increase the capillary number by about 1000 times through its low IFT effect, thus unlocking the residual oil. Besides, the emulsification of the surfactant can hamper the breakthrough along the main streamline and increase sweep efficiency [21]. And for oil-wet reservoirs, the surfactant can alter the wettability of the rock surface to water-wet, which is beneficial to microscopic displacement efficiency. Alkali reacts with the natural organic acids (naphthenic acid group) present in the crude oil, forming an in situ surfactant (different from the injected surfactant) at the oil-water interface which reduces the interfacial tension (IFT) [22]. And alkali also possesses the emulsification and wettability alternation effect.

The synergies of ASP may be summarized as follows: (1) there is a competition of adsorption between the polymer and the surfactant; thus, the addition of polymer can reduce the adsorption of surfactant on rock surfaces [23]. (2) Alkali also reduces the surfactant adsorption, which makes the surfactant work more efficiently and reduces costs. (3) Polymer helps to stabilize emulsions due to the emulsification of surfactant and alkali, which contributes to improving the sweep efficiency. (4) There are synergies between soap (generated from the reaction between alkali and organic acid) and injected surfactant. And the mixed system possesses stronger IFT reduction and emulsification effects. (5) Polymer can react with Ca^{2+} and Mg^{2+} to prevent the surfactant from becoming calcium and magnesium salt of low activity. (6) It was reported that the decrease of water production was not only related to the increase of the viscosity of displacing fluid but also related to emulsification and scaling after injection of ASP slug [24]. (7) Molecular chain of polymer combines with the nonpolar part of the surfactant to form association under the salt condition. Besides, the interaction between the surfactant and the polymer changes the configuration of polymer aggregation and stretches molecular chain, thereby increasing the viscosity of displacing fluid [21].

Although ASP flooding has been proven to be an effective method for enhancing oil recovery and has been fruitful in actual oil fields [25–27], due to the late birth of this technique, its enhanced recovery mechanism and characteristics, especially the evolution of pressure field, remain to be explored. Physical experiments [27–29] and numerical simulation [30–34] about ASP have been conducted in recent years. Li et al. [35] studied performance of ASP systems

and effects of the individual component. Wang et al. [36] established the loss law of ASP systems, and they also found that formation damage is available in the ASP flooding EOR. Delshad et al. [31] developed a simplified ASP numerical model considering a large number of reactions, and several ASP pilots were successfully modelled. However, as an important indicator of the effectiveness of ASP flooding, pressure gained little attention in the past. So, how does pressure evolve at various stages of ASP flooding? What is the difference between the pressure in the near-well zone and that in the deep reservoir? How to guide the injection process of ASP flooding in actual oil fields according to the evolution characteristics of pressure field? These questions will become the research content of this paper.

In this study, a large sandpack heterogeneous model is used to study development performance and pressure characteristics of different ASP flooding stages. Recovery and pressure are recorded dynamically. Average pressure front, the distance between the inlet and the average pressure front, and area ratio are proposed to characterize the pressure evolution process. In addition, different experimental conditions (different viscosities and heterogeneities) are provided to discuss adaptability of heterogeneous reservoirs to ASP flooding. Lastly, evolution characteristics of the pressure field are obtained by experimental and numerical methods to gain response expression between pressure and injection parameters, which helps engineers design better project plans to extract the residual oil in an oriented way.

2. Material and Method

The physical simulation about ASP flooding pressure field development is conducted in this section. A large three-layer heterogeneous laboratory model was employed to monitor the pressure field of different stages in ASP flooding. It could provide reference and fundamental for numerical simulation.

2.1. Laboratory Model. The laboratory model used in this experiment was a $60\,cm \times 60\,cm \times 4.5\,cm$ sandpack model with high/middle/low-permeability layers from top to bottom in order to represent heterogeneous formation. It was equipped with limited measurement points to obtain pressure data that reflect actual pressure field through the interpolation method.

Restricted to the size of the laboratory model, the amount of measurement points was limited and excessive measurement points also brought complex to the data acquisition procedure. So, how to achieve the most precise reduction by means of those measurement points and simultaneously simplify the experiment procedure as much as possible were our primary task. There were numerous measurement point configurations, such as Full-Matrix, Semimatrix, Side Bidirectional Axis, and Full + One-way Axis, which are shown in Figure 1.

To optimize the pressure monitor system, reduction rate and saturation rate were defined. The reduction rate is defined as
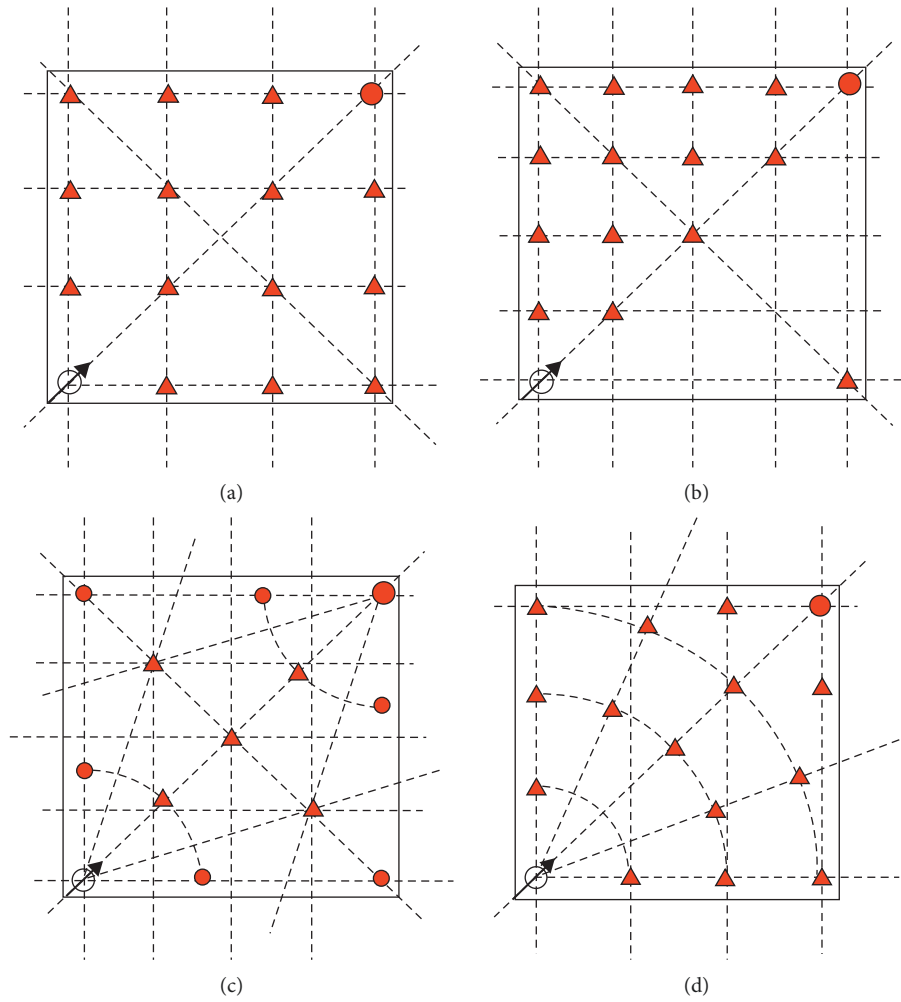
(a)

(b)

(c)

(d)

Figure 1: Available measurement point configurations. (a) Full-Matrix. (b) Semimatrix. (c) Side Bidirectional Axis. (d) Full + One-way Axis.

$$P = \frac{n}{N}, \qquad (1)$$

where n is the number of valid measurement points (mistake is less than 5%) and N is the total number of measurement points. A waterflooding pressure field was available by interpolating pressure data of measurement points. By comparing the interpolation results and numerical simulation results, the reduction rate could be calculated naturally.

The effect of oil saturation process was the key basis for the success of the experiment. Based on numerical simulation, the optimal saturation mode (injection order and relationship between injection and production) and corresponding saturation rate under different pressure measurement point arrangement modes were obtained, which guided saturation process in the experiment.

The saturation rate is defined as

$$\eta = \frac{1 - \overline{S_w}}{1 - S_{wc}}, \qquad (2)$$

where $\overline{S_w}$ is the average water saturation and S_{wc} is the residual water saturation.

The optimization of saturation process is shown in Figure 2. Different saturation orders were designed to calculate saturation rate through numerical simulation.

The optimization process of measurement point detection (including number, configuration, and saturation process) is shown in Figure 3. Thus, the Side Bidirectional Axis pattern achieved the largest reduction rate and would act as the candidate for pressure measurement configuration of our laboratory model, which is depicted in Figure 1(d).

The interpolation method was crucial for reduction results of the pressure field. Quantities of interpolation methods were available (e.g., "Inverse Distance to a Power," "Kriging," and "Minimum Curvature") to accomplish our goal, whereas there was slight distinction between them for our measurement point configuration. Figure 4 shows the optimization process of the interpolation method. We can see that the kriging method possessed the highest precision, which would be adopted for future study.

In conclusion, the final laboratory model is depicted in Figure 5.

In order to explore the influence of heterogeneity on pressure field improvement, models of 3 kinds of

Plan 1 Saturation order Saturation rate

Step 1:   1 3 4 5   42%

Step 2:   1 3 4 2   86%

Plan 2 Saturation order Saturation rate

Step 1:   1 2 3 4   72%

Step 2:   2 3 4   85%

Step 3:   5 3 4   92%

Plan 1 Saturation order Saturation rate

Step 1:   5 1-4 6-9   88%

Plan 2 Saturation order Saturation rate

Step 1:   1 6 9 5   20%

Step 2:   1 6 9 3 4 5   45%

Step 3:   1 3 4 7 8   85%

Step 4:   1 2 7 8   95%

Plan 3 Saturation order Saturation rate

Step 1:   1-4 5-9   80%

Step 2:   5 6-9   93%

Plan 4 Saturation order Saturation rate

Step 1:   3 4 5-9   40%

Step 2:   1 2 6-9   90%

Plan 3 Saturation order Saturation rate

Step 1:   5 1 4   68%

Step 2:   1 3 4   79%

Step 3:   2 3 4   90%

Note: producer is shut as water cut reaches 95%

Red: injector

Blue: producer

Injector
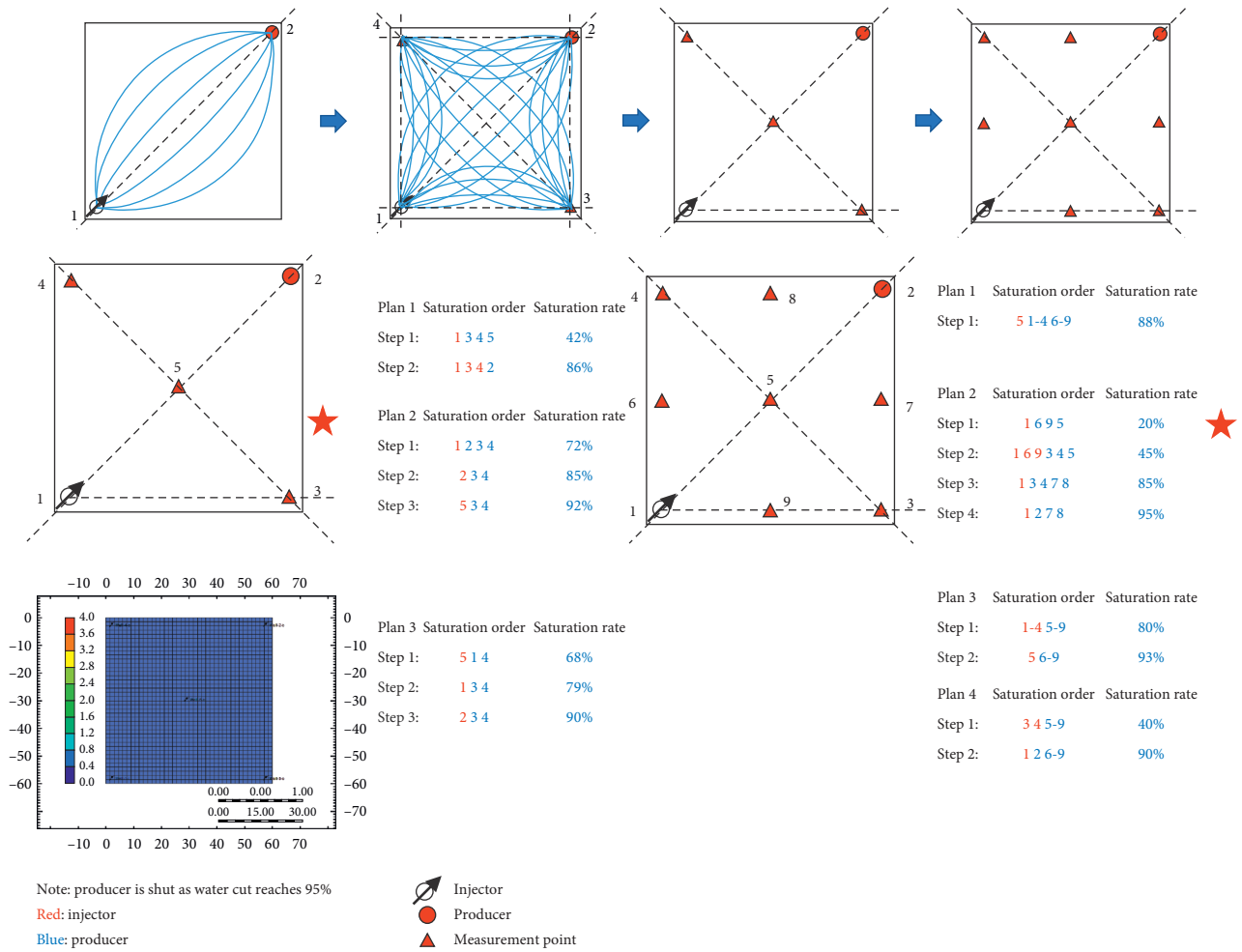
Producer

Measurement point

FIGURE 2: Optimization of saturation process.
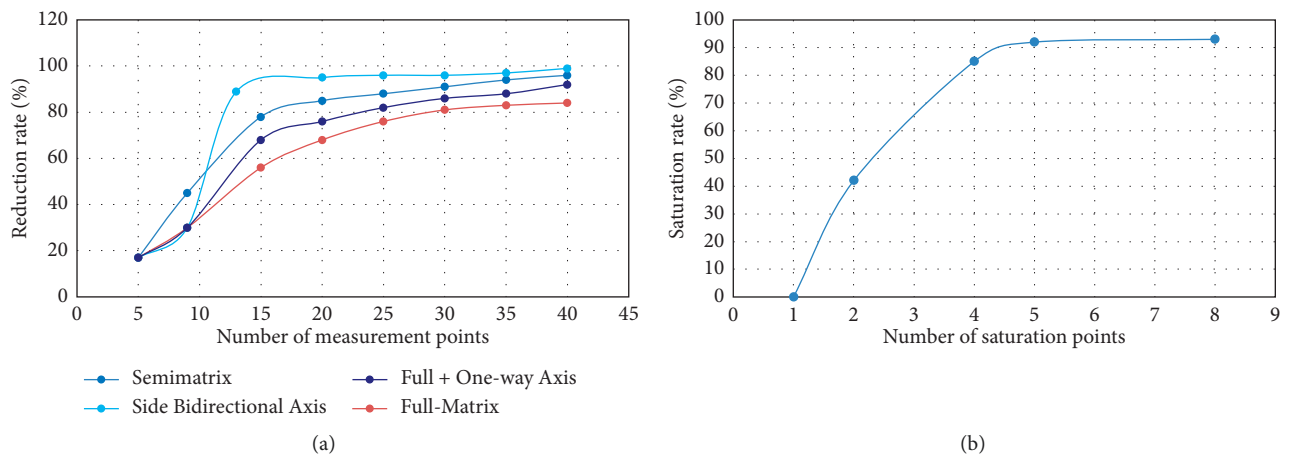

(a)

(b)

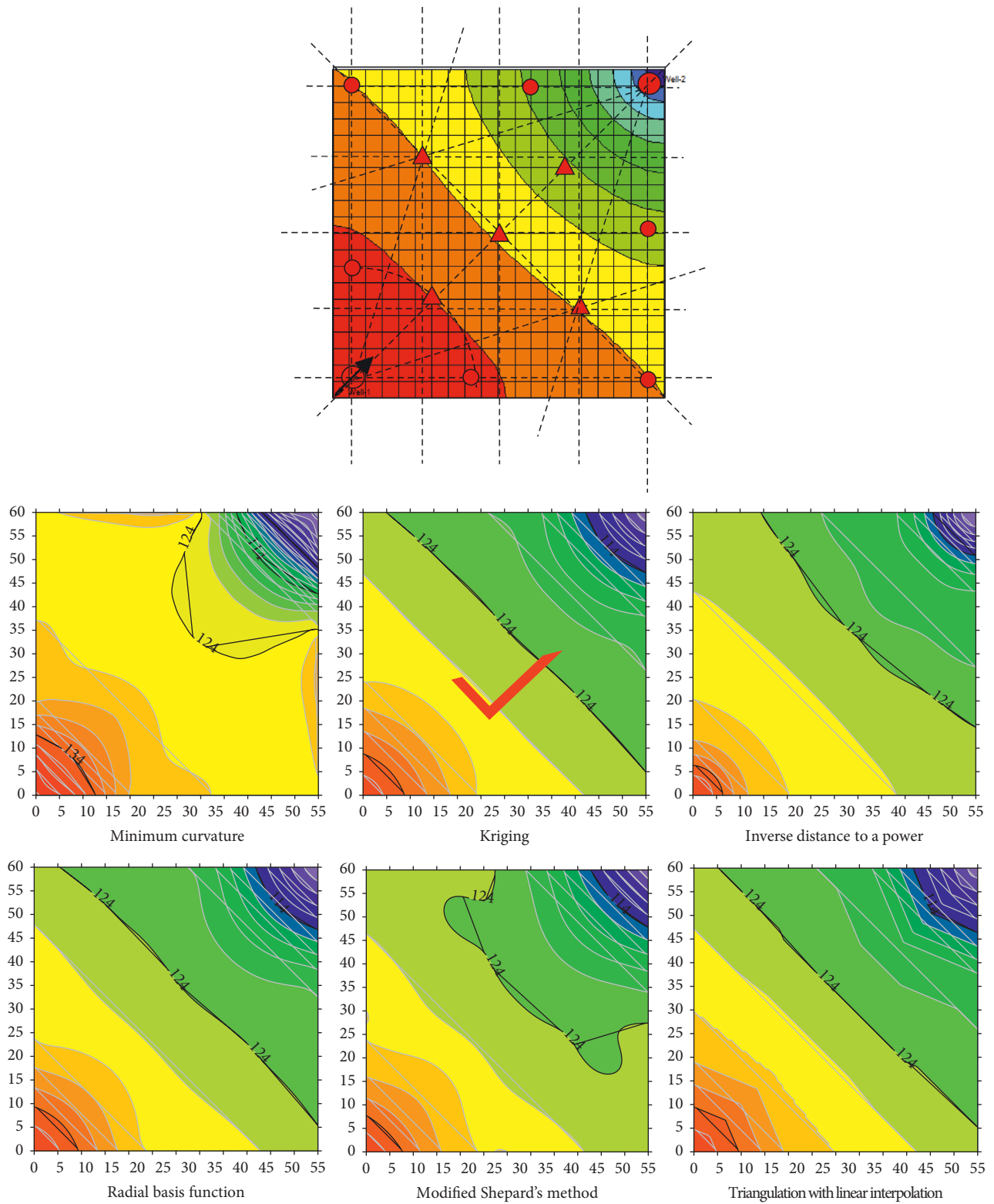FIGURE 3: Optimization of (a) measurement points and (b) saturation points.

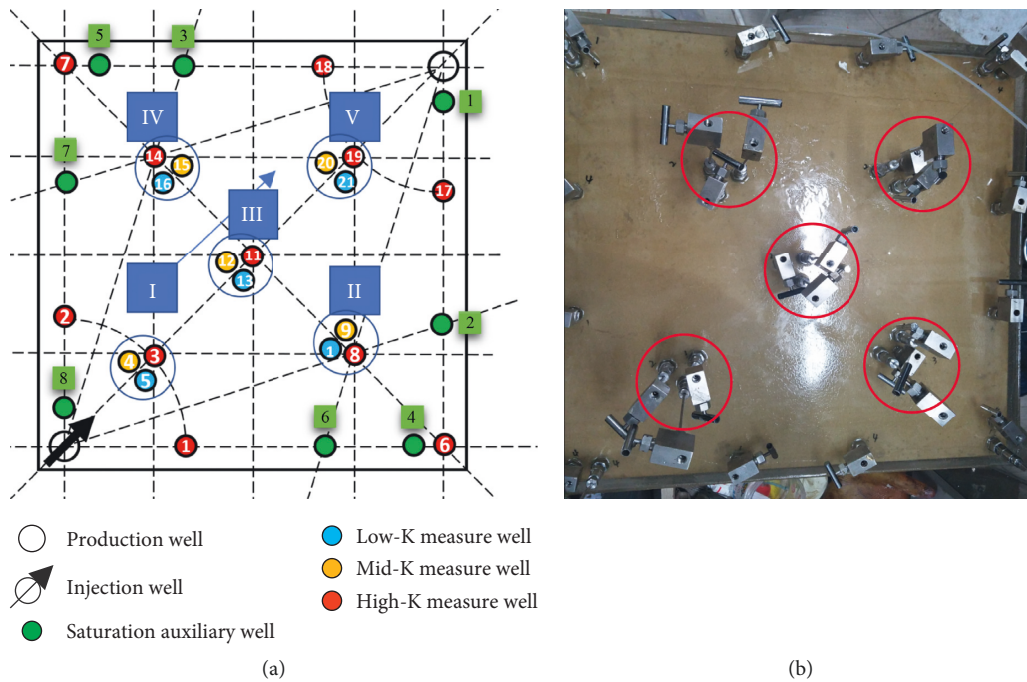Figure 4: Optimization of the interpolation method.

(a)

(b)

FIGURE 5: Layout of measurement points in the laboratory model. (a) Schematic diagram of the laboratory model. (b) Photo of the laboratory model.

TABLE 1: Experimental conditions.

Number	Variable	
	Heterogeneity (mD)	Injection viscosity (cp)
1	200 : 600 : 1000	30
2	200 : 600 : 1000	40
3	300 : 600 : 900	30
4	300 : 600 : 900	40
5	400 : 600 : 800	30
6	400 : 600 : 800	40

TABLE 2: Formula of simulated formation water.

Component	Concentration (g/L)
NaCl	2.294
KCl	0.013
$CaCl_2$	0.042
$MgCl_2 \cdot 6H_2O$	0.172
Na_2SO_4	0.075
$NaHCO_3$	1.86

heterogeneity and 2 kinds of mobility were designed. Table 1 lists permeability and injection viscosity of each model.

2.2. Experiment Material

2.2.1. ASP

(1) Alkali. To lower the caustic consumption of NaOH/ Na_2SiO_3, sodium carbonate (Na_2CO_3) was selected instead as the alkali agent in the flooding [5, 6]. The active alkali content is 99.5%.

(2) Surfactant. Because of relatively low adsorption on sandstone, XPS anionic petroleum sulfonate was employed as the surfactant in the chemical preparation. The active surfactant content is 38.8%.

(3) Polymer. The typical synthetic polymer we used was partially hydrolysed polyacrylamide (HPAM) (Daqing Refining & Chemical Company, China), which is a water-soluble polyelectrolyte with negative charges. The solid

content is over 90%, hydrolysis degree is less than 6%, and the molecular weight ranges from 6 million to 10 million.

2.2.2. Oil.

The oil sample we used in the experiment was the mixture of kerosene and crude oil. The viscosity was 10 MPa·s at 45°C (Table 2).

2.2.3. Formation Water.

The salinity of the formation water sample was 4456 mg/L, and the formula is shown in Table 1.

2.3. Experiment Equipment.

The whole displacement device included data acquisition system, constant flux pump, vacuum system, incubator, physical model, oil/water metering system, and backpressure system (Figure 6). The temperature of the experiment was 45°C.

2.4. Experiment Procedures.

The whole experiment was divided into five steps: sealing inspection; water saturation; oil saturation; waterflooding; and ASP flooding (Figure 7).
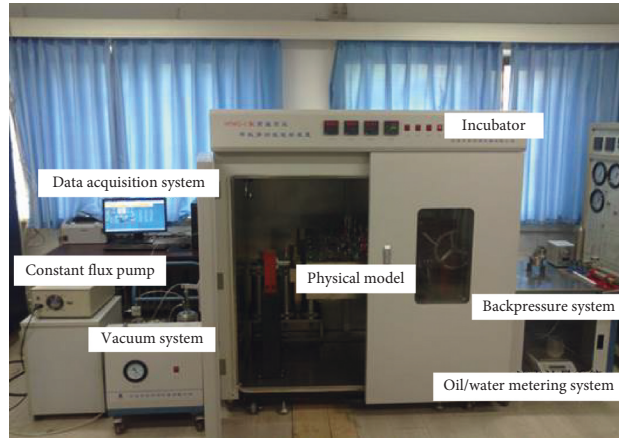
FIGURE 6: Experiment equipment.

(a)   (b)   (c)
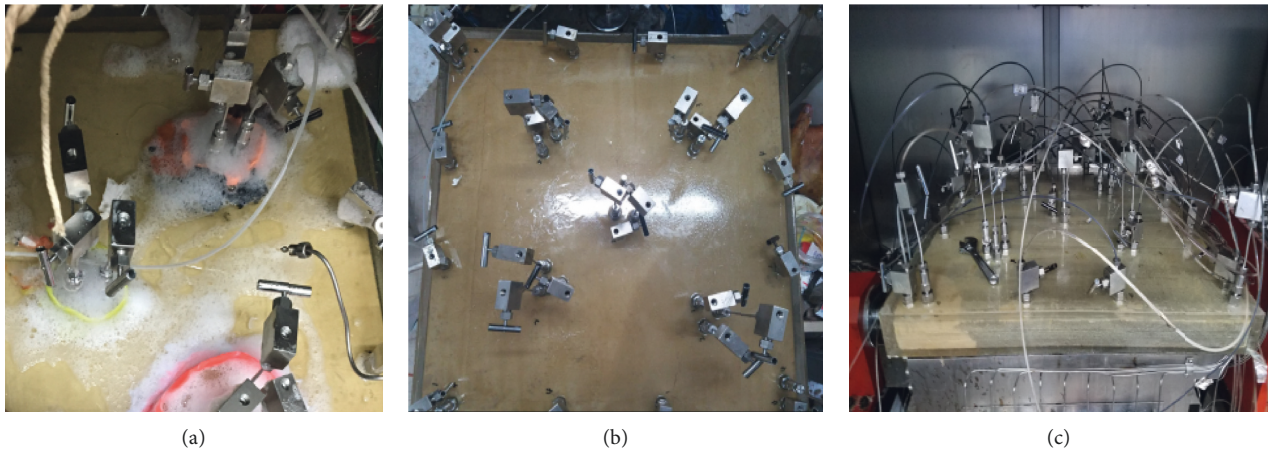
FIGURE 7: Experiment procedures. (a) Leak detection. (b) Water saturation. (c) Oil saturation.

Due to numerous measurement points, sealing of the laboratory model was a key factor to the success of the experiment. As is shown in Figure 7(a), we used foam to detect the leaky valves and repaired them with glue.

Particularly, during ASP flooding stages, the slug solution in each stage is shown in Table 3. After each slug solution was made, added it to the intermediate container and connected to the pipeline. The injection rate was 1 mL/min, took samples every 30 min to measure the oil production, water cut, and water phase viscosity.

3. Results and Discussion

3.1. Development Performance. Development performance is shown in Figure 8 (take model 1 as an example). In the primary waterflooding stages, oil cut was 100%, and oil recovery was increasing rapidly. At about 0.25 d of water-flooding, water front reached the outlet of the model and water cut rose sharply. And the recovery climbed steadily to 39.5% until waterflooding ended. Then, ASP flooding that contained preflush, main, auxiliary, and postprotection stages began. The minimum water cut (67.1%) occurred at the end of main slug stages. Since the end of main slug stages,

the synergistic effect of the ASP had decreased, and the water cut had gradually increased due to the retention of a large amount of the chemical agent in the pores (especially near the inlet). The pressure near the outlet maintained a high level. Finally, the subsequent waterflooding supplemented the slug displacement energy. The viscosity of the production fluid began to decrease significantly and returned to the initial level. All pressures also began to decrease, and when the water cut rose steadily to 98%, the entire development ended.

Viscosity of the produced fluid is shown in Figure 9. In the waterflooding and early stage of the main slug process, viscosity of the produced fluid remained constant about 2.5 MPa·s, which indicated that there was only water flowing out of the model. At the end of the main slug stage, the ASP system reached the outlet of the model, and viscosity of effluent increased to over 10 MPa·s. And when the subsequent waterflooding came, viscosity returned to the initial level. Meanwhile, the shear thinning phenomenon of the produced fluid was observed.

3.2. Water Cut. The water cut curve is shown in Figure 10. We can draw the conclusion that minimum water cut was smaller and its appearance time was later under the

TABLE 3: Formula of each slug in ASP flooding.

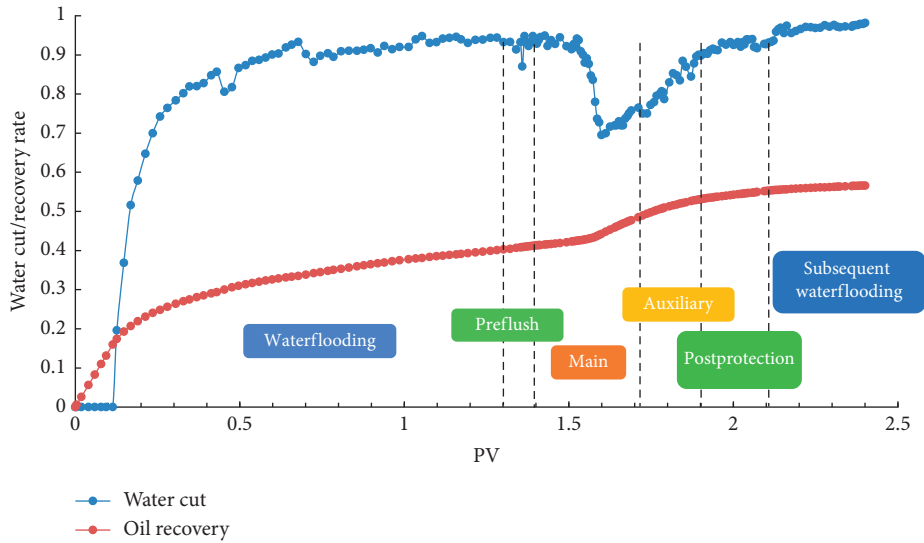| Stage	Injection volume	Mass fraction (%)		
		Polymer	Surfactant	Alkaline
Preflush slug	0.08 PV	100	0	0
ASP main slug	0.3 PV	98.5	0.3	1.2
ASP auxiliary slug	0.2 PV	98.9	0.1	1
Postprotection slug	0.2 PV	100	0	0

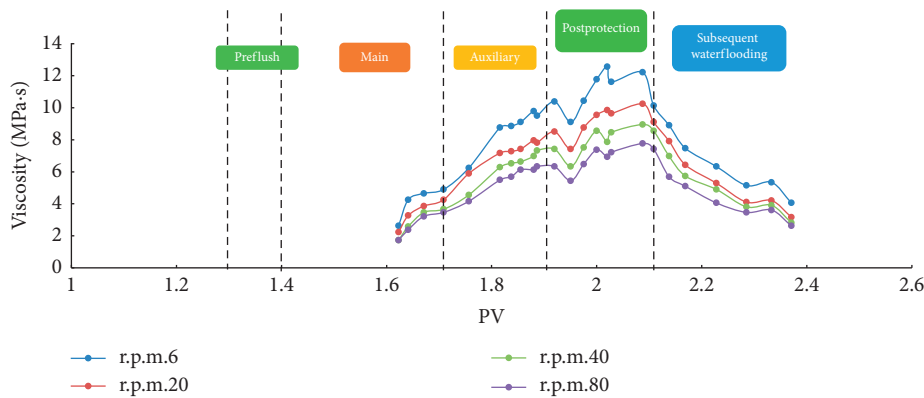FIGURE 8: Development performance of No. 1 experiment.

FIGURE 9: Viscosity change of produced liquid.

condition with higher injection viscosity. Water cut began to decrease earlier but to a small extent as to the model with strong heterogeneity. It was worth noting that, at the same viscosity, the water cut curve fluctuation of the 200 : 600 : 1000 model was more severe than the other two models, demonstrating that the model of strong heterogeneity was unstable and it was prone to occur local breakthrough phenomenon.

3.3. Oil Recovery.
Under the same conditions, the stronger the heterogeneity, the greater the contradiction between layers due to permeability difference and the lower the oil recovery in the waterflooding stage (Figure 11). In the ASP

flooding stage, the model with weak heterogeneity can better recover oil in the middle and low-permeability layers. For models with the same heterogeneity, a greater enhanced recovery corresponded to a higher viscosity of the injected fluid. Due to the higher viscosity/concentration, injected fluid could reduce the mobility ratio and improve the profile (especially the high and the middle permeability layer) more effectively. And this phenomenon was more remarkable in the model with strong heterogeneity.

3.4. Liquid Production Index per Meter.
Liquid production index was an indicator of the production ability of oil wells.
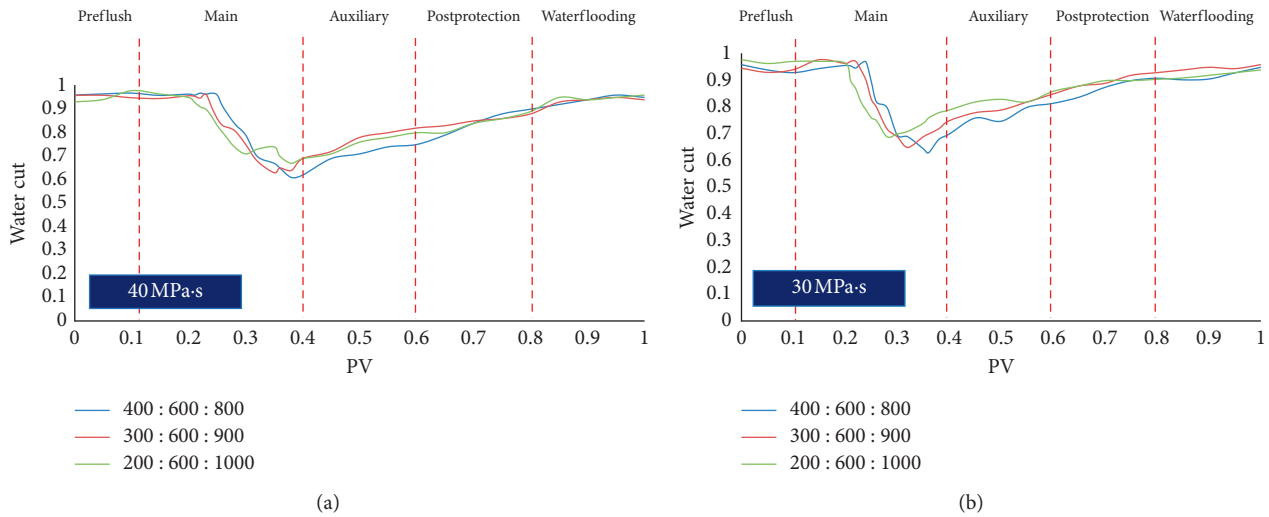
FIGURE 10: Water cut curve comparison. (a) Water cut with viscosity of 40 MPa·s. (b) Water cut with viscosity of 30 MPa·s.
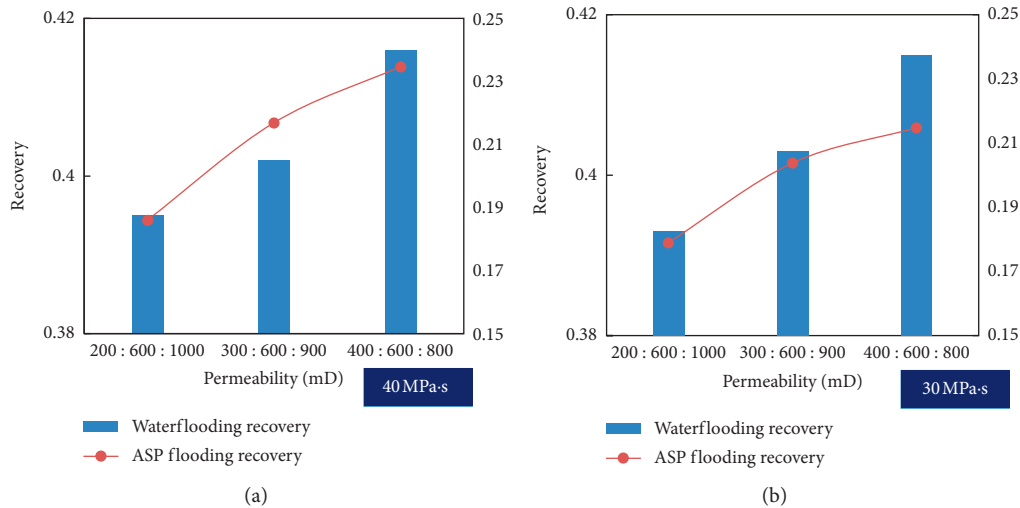

FIGURE 11: Oil recovery comparison. (a) Oil recovery with viscosity of 40 MPa·s. (b) Oil recovery with viscosity of 30 MPa·s.

Prediction of the liquid production index under different water cut conditions was a main basis for the production evaluation. In the ASP flooding stages, liquid production index per meter showed a falling tendency (Figure 12), which was ascribed to high viscosity of the ASP system. Due to the increase of macroscopic sweep efficiency and microscopic displacement efficiency, liquid production index restored to a certain degree in the main slug stages.

At the same viscosity, the liquid production index per meter was at a lower level with stronger heterogeneity, which was obvious in the preflush stage. Meanwhile, liquid production increase during the main slug stage was not obvious. After the auxiliary slug stage, viscosity and heterogeneity had little effect on the liquid production index.

3.5. Pressure Field Development

3.5.1. One-Dimensional Reduction. As is shown in Figure 13, the lower left corner was the inlet, the upper right corner was

the outlet, and the diagonal line constituted the main streamline. In the one-dimensional pressure field development reduction, we selected the main streamline as our research objective.

The pressure difference along the main streamline was divided into four parts (Figure 14). In the waterflooding stages, all 4 pressure differences were small and tended to be stable at the end. Then pressure near the inlet increased sharply as the preflush polymer was injected into the model. The pressure wave gradually spread forward along the main streamline, and pressure in the middle also began to climb. It was observed that the middle part pressure soared, indicating the previous polymer solution migrated ahead. During the late stage of the main slug, the injected polymer travelled to the vicinity of the outlet, causing the last two pressure differences (ΔP_3 and ΔP_4) rose in turn but the amplitude was weakened. When injecting postprotection slug, the value of 4 pressure differences reversed.
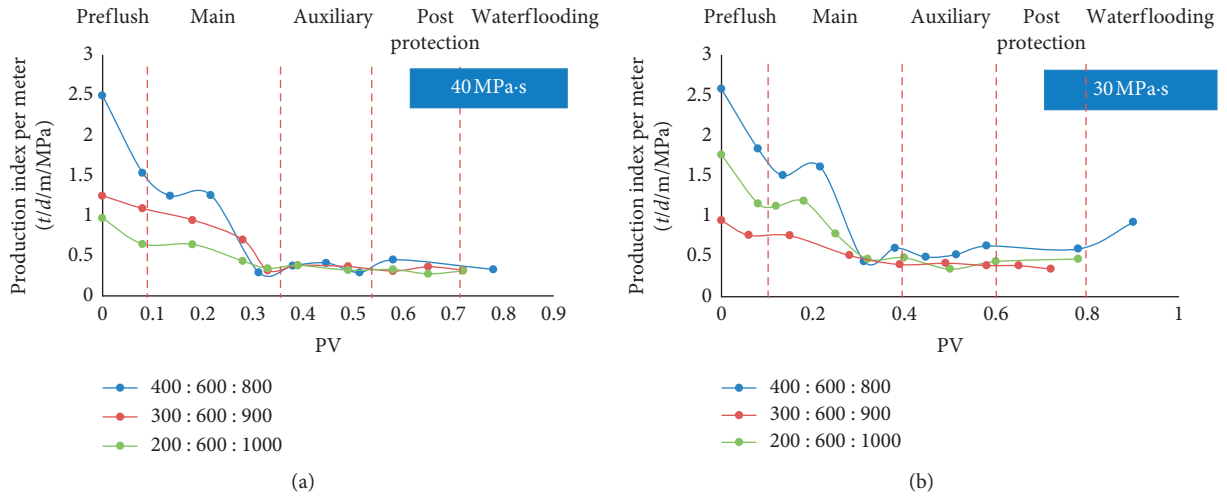
FIGURE 12: Liquid production index per meter (a) with viscosity of 40 MPa·s and (b) with viscosity of 30 MPa·s.
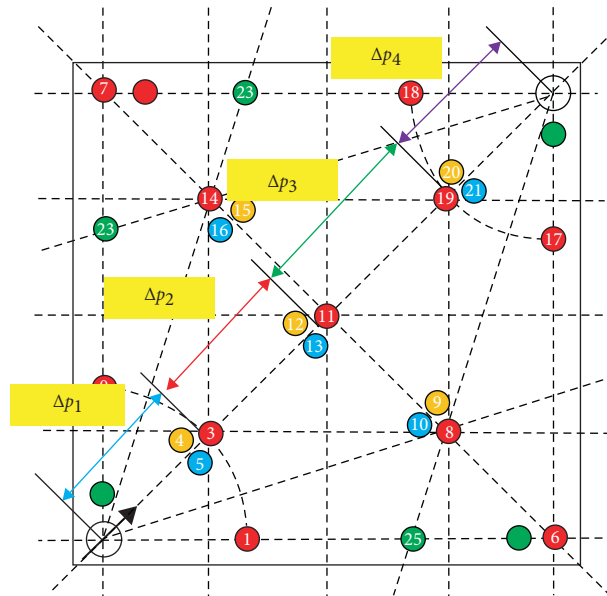

FIGURE 13: Schematic diagram of pressure differences along the main streamline.
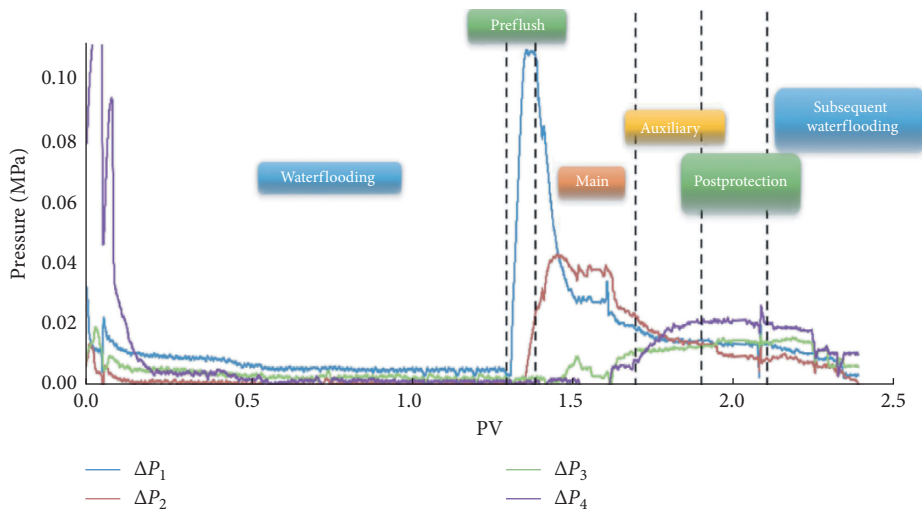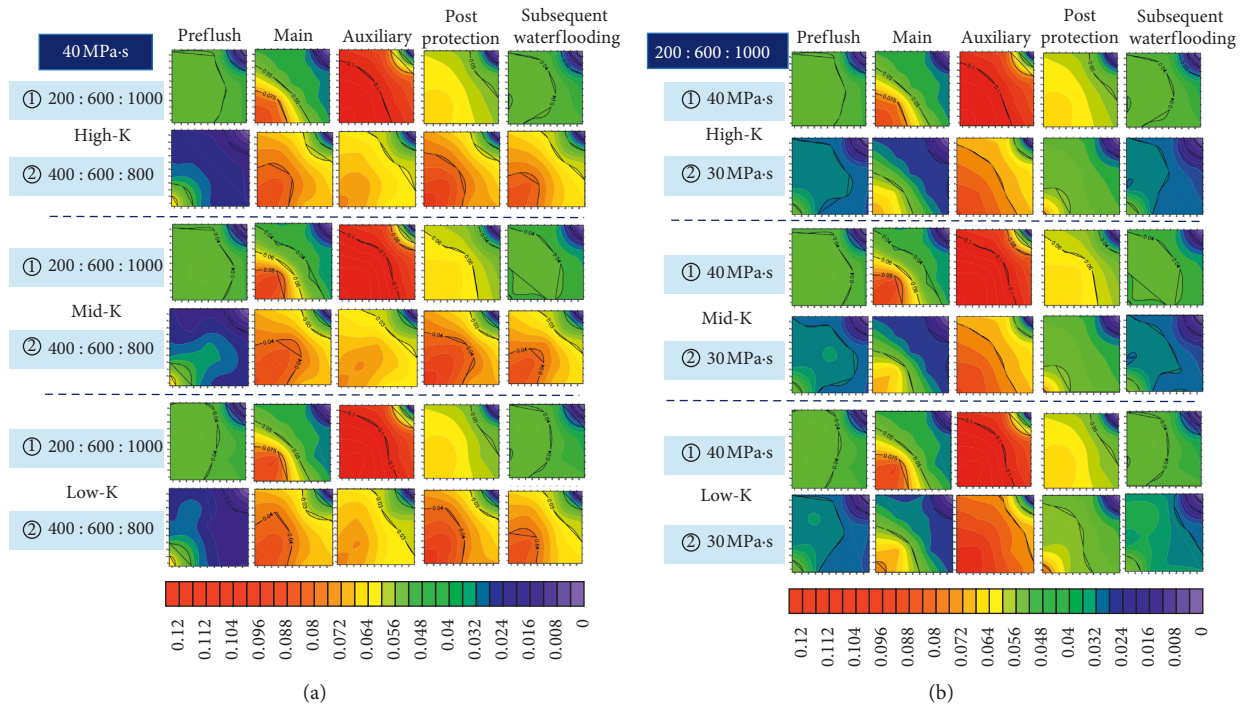

FIGURE 14: Sectional pressure differences.

FIGURE 15: Two-dimensional pressure field of (a) different heterogeneities and (b) different viscosities.
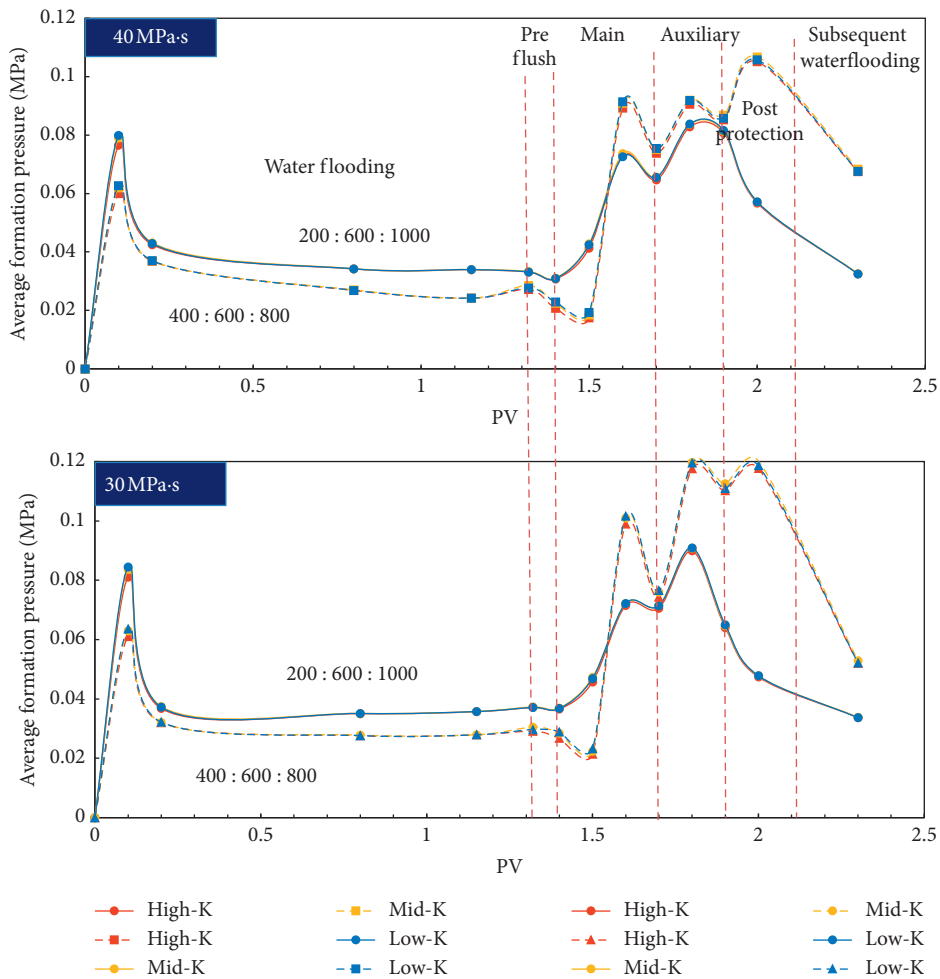

FIGURE 16: Average pressure curve comparison of different heterogeneities and viscosities.
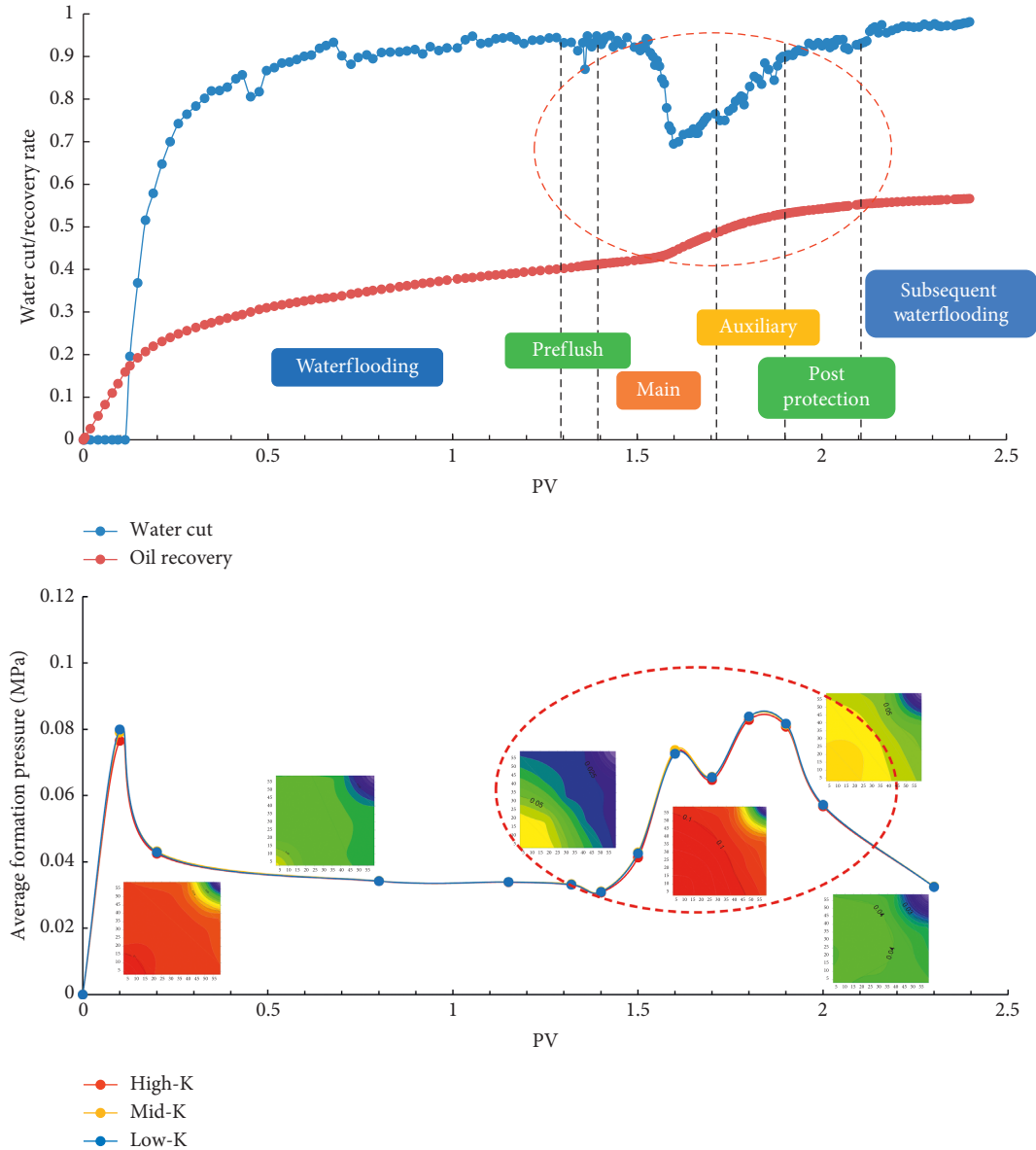
FIGURE 17: Production dynamics and pressure field.

3.5.2. Two-Dimensional Reduction. The interpolation method was used to process the data collected at the measuring point for the purpose of restoring the two-dimensional pressure field. Figure 15(a) shows the two-dimensional pressure field of different heterogeneities. From the preflush to the auxiliary slug stage, pressure of model ② was lower than model ① but maintained a higher level in the late period (the postprotection and the subsequent waterflooding stage). There was an obvious breakthrough along the main streamline in model ②. The pressure tendency of model ① was to rise primarily and then dropped, while the pressure of model ② fluctuated in the late stage.

Figure 15(b) is the two-dimensional pressure field of different viscosities. The pressure increased to a larger extent and the pressure gradient was more obvious of highly viscous system. For model ②, because of the low displacement intensity, the difference between three layers was relatively small, and the moving rate was similar. Model ① has a better recovery in high and middle permeability layers (mainly the middle permeability layer), and model ② has better recovery in middle and low-permeability layers (mainly the lower permeability layer).

The average formation pressure was a significant indicator for reservoir energy, and it could be acquired via interpolated data of two-dimensional reduction. It was a steeply rising-falling-rising in fluctuation-falling process in our experiment (Figure 16). The preflush slug pressure rose greatly but contributed little to the average formation pressure. The average pressure of the model with weak heterogeneity was lower, but its pressure increasing scale in the ASP flooding stage was much larger than that of other models. And the pressure and pressure increasing scale were at a higher level under the higher viscosity condition.
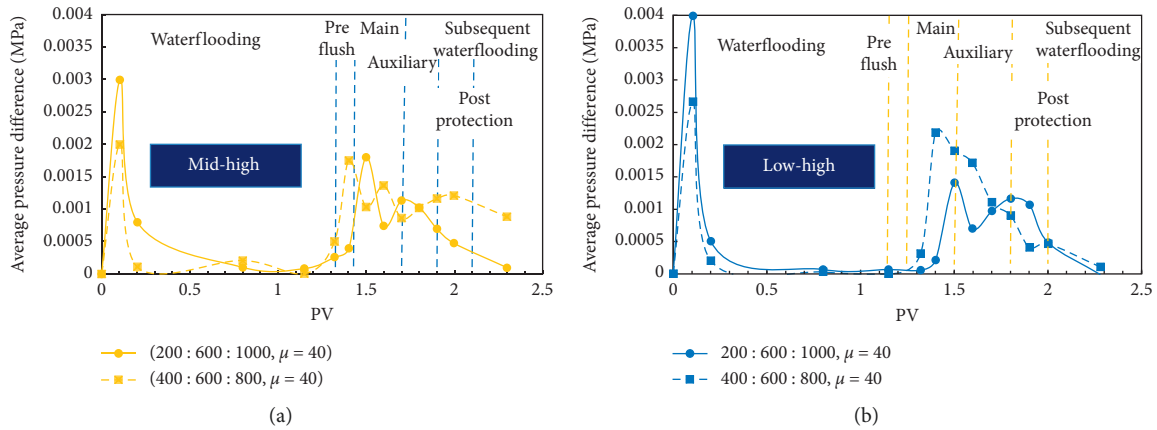
FIGURE 18: Average pressure difference curve. (a) Average pressure difference between the middle and the high permeability layer. (b) Average pressure difference between the low and the high permeability layer.
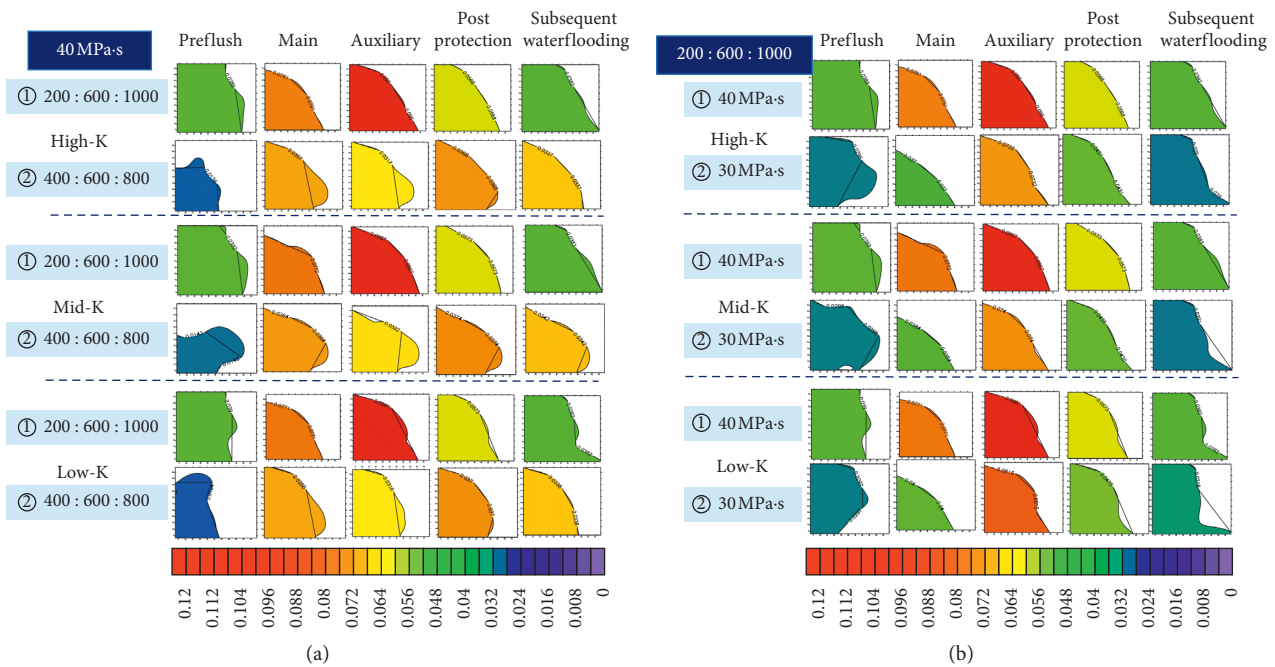
FIGURE 19: Average pressure front of (a) different heterogeneities and (b) different viscosities.

Through the above calculation and analysis, the corresponding relationship between production dynamics and the pressure field is depicted in Figure 17.

In order to compare pressure of each layer under different heterogeneous conditions, we made the subtraction between pressure of the middle or low-permeability layer and that of the high permeability layer (Figure 18). Due to the resistance, the average formation pressure of the middle and low-permeability layers was greater than that of the high permeability layer. In the waterflooding stage, the model of strong heterogeneity had a great pressure difference between the middle and low-permeability layer, whereas in the ASP flooding stage, the middle and low-permeability layer possessed a great pressure difference in the homogeneous model. The model of weaker heterogeneity represented a

more frequent fluctuation of pressure difference, indicating that the flow steering between layers was more sensitive and frequent.

Based on the two-dimensional pressure field above, we could find out the average pressure front characteristics (Figure 19(a)). The average pressure front figure reflected the overall pressure level of different layers. We could see that the pressure front became smooth in the late period of ASP flooding, showing that the flow profile was improved. Model ② (weak heterogeneity) performed better in the subsequent waterflooding according to its smoother pressure front. In particular, as for the low-permeability layer, profile amelioration of model ② performed better than that of model ①.

Figure 19(b) is the average pressure front of different viscosities. Ascribed to low viscosity, there was an apparent

FIGURE 20: Schematic diagram of distance between the average pressure front and the inlet.

(a)   (b)   (c)

FIGURE 21: L of (a) high permeability layer, (b) middle permeability layer, and (c) low-permeability layer with different viscosities.

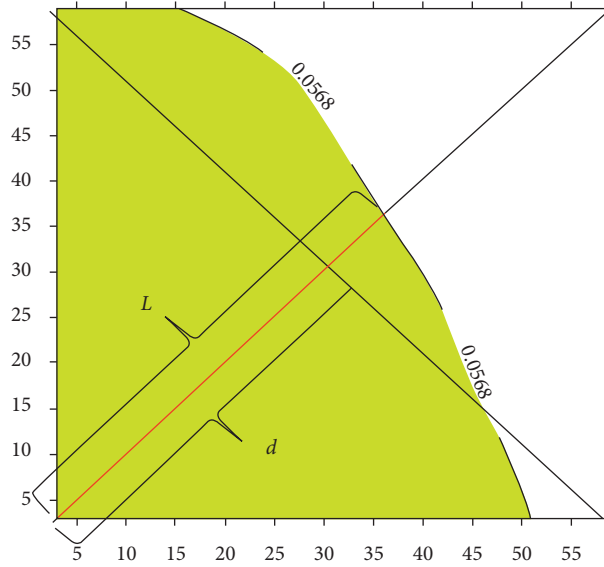front breakthrough phenomenon in model ① in the preflush and subsequent waterflooding stage. The injection profile modification on the high permeability layer of model ① was effective which was ascribed to stabilization effect on pressure front of the high-viscosity injected agent. And the low-viscosity agent was prone to enter the low-permeability layer and improved its development effect.

Here, we define L was the distance between the inlet and the average pressure front in the main streamline and d was the distance between the inlet and the model centre point (Figure 20). In this experiment, $d = 39.6$ cm.

And L versus injection volume (PV) curve of different viscosities is shown in Figure 21. The figure shows that, at different viscosity conditions, L declined initially and rose later. L was close to d and demonstrated a more stable pressure front. And the most stable pressure front occurred in the main slug stage. At low viscosity, the movement amplitude of the pressure front was reduced, and declining time was delayed. It was also concluded that the low-viscosity agent had little influence on the middle permeability layer but had a great influence on the high and low-permeability layer.

In order to make a deep sight in the pressure front advancement, we defined the area ratio of the average pressure front as

$$S = \frac{S_1}{S_2}, \tag{3}$$

where S_1 is the area enveloped by the pressure front and S_2 is the area of the rest part of the pressure field, which is illustrated in Figure 22. The pressure field would be more uniform if S is closer to 1, and in this case, the development performance was better.

Under different heterogeneity conditions, S initially declined and rose later (Figure 23). In the preflush stage, pressure near the inlet increased sharply, resulting in the retreat of pressure front, so the value of S began to fall. And the pressure field was likely to be more uniform during the main and auxiliary stages for $S < 1 \pm 0.5$. At the subsequent waterflooding stage, S returned to a relatively high level.
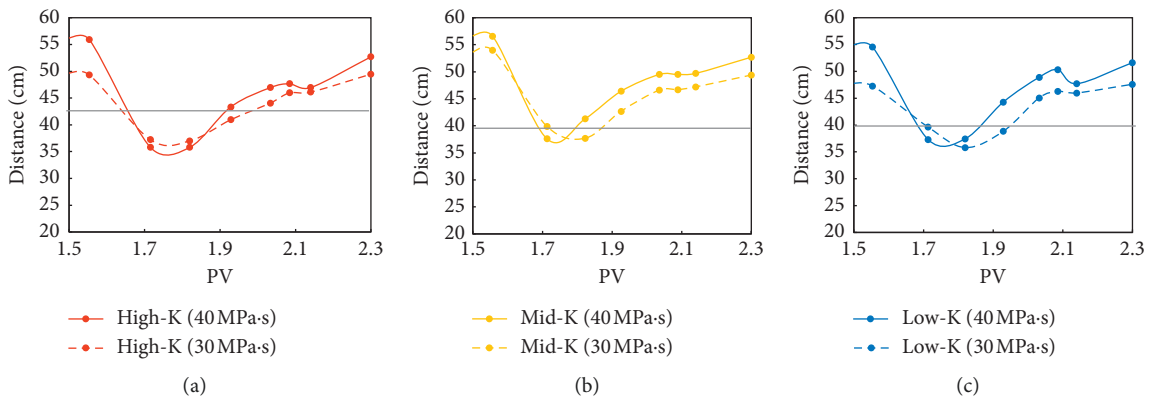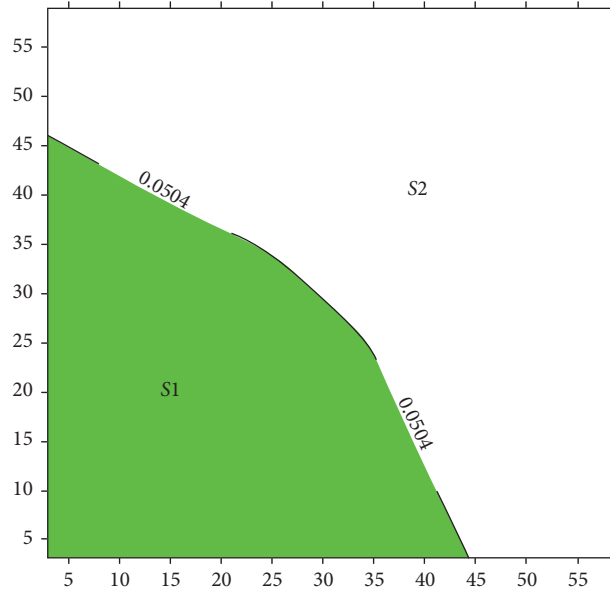
FIGURE 22: Schematic diagram of the area ratio.

(a)

(b)

(c)
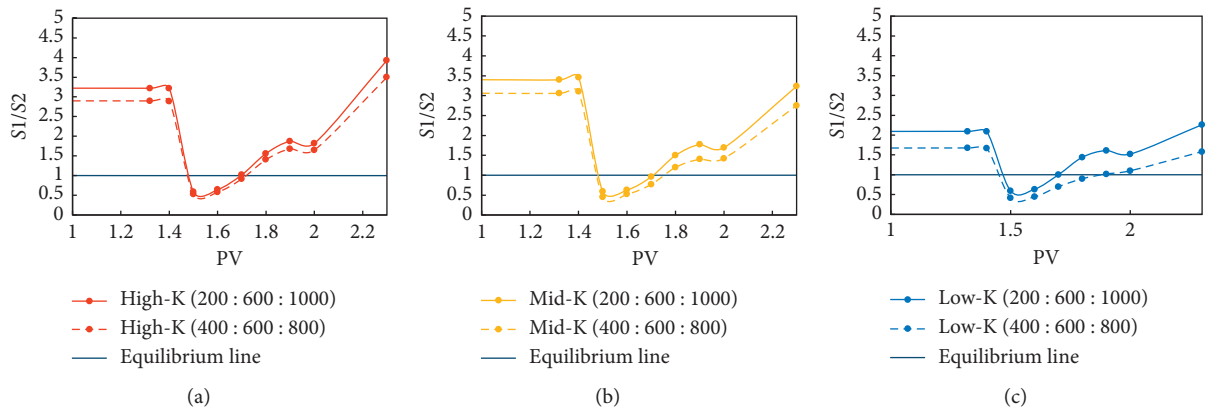
FIGURE 23: S of (a) high permeability layer, (b) middle permeability layer, and (c) low-permeability layer with different heterogeneities.

Compared with the other layers, the area ratio of the middle permeability layer decreased more obviously, revealing the best profile control. The area ratio of the relatively homogeneous model was less than that of other models, indicating that advancement of the pressure front preferred to be more stable, which ensured a better development performance.

In summary, with regard to the strong homogeneous formation, the water cut curve performed a wide, shallow, and more fluctuant funnel, which had poor production ability. In addition, waterflooding and ASP flooding recovery were much lower. On the contrary, for the weak homogeneous formation, the inlet pressure and average pressure increasing scale of the ASP stage skyrocketed to a larger extent, and in this case, achieving a good development effect of the low/middle permeability and less contradiction between different permeability layers. Viscosity of the injected agent also made a difference to the ASP flooding effect. When a high-viscosity agent was injected into the reservoir, water cut would drop later and drastically, and the ASP flooding would be more efficacious. Low-permeability layer was attractive to the low-viscosity agent; thus, its development status was ensured to be enhanced naturally. And the high-viscosity agent was beneficial to profile control, which unlocked the untouched reserve.

3.6. Numerical Simulation Methodology. Given the production data and chemical properties from laboratory test, the numerical model was established all based on the data acquired from the physical model. After history match, the numerical simulation model was used to further study the development process of the ASP flooding.

3.6.1. Numerical Simulation Model of ASP Flooding. At present, most mechanisms could be characterized by the commercial reservoir simulators, but there were still some parts that cannot be described reasonably. In this section,

(a)   (b)   (c)
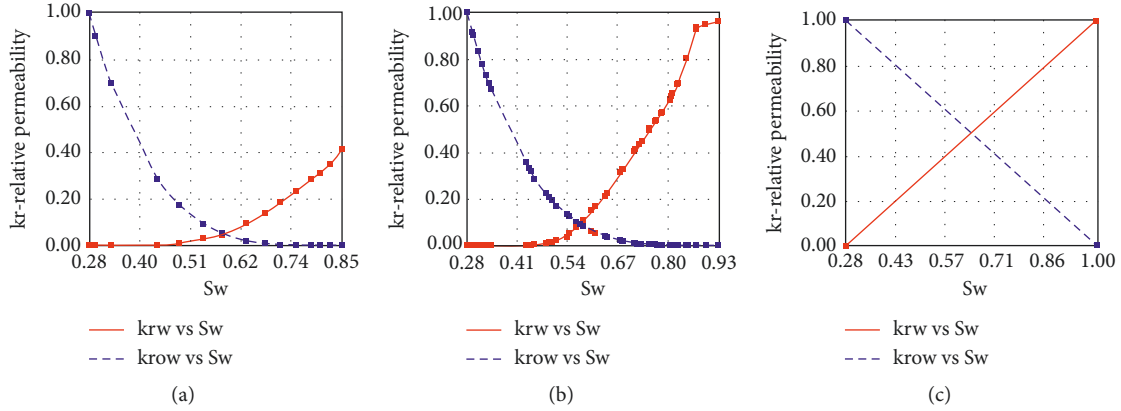
FIGURE 24: Relative permeability curves used in the simulator.
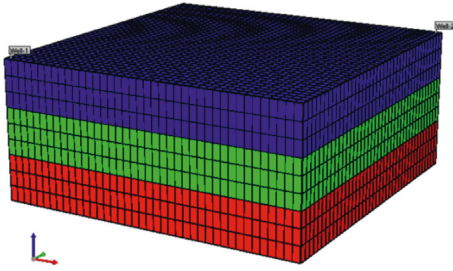
FIGURE 25: The numerical simulation model.

FIGURE 27: History matching result of recovery.

FIGURE 26: History matching result of water cut.

considering the physical and chemical process during the ASP flooding, we established the numerical simulation model on the basis of the CMG reservoir simulator. The factors that were considered in the model contain as follows:

(1) Adsorption. Due to the higher surface to volume ratio of the rock, adsorption phenomenon would happen during the ASP flooding. The adsorption caused the retardation of surfactant transport [37]. And the adsorption was higher in the low-permeability rock as it had smaller grain sizes, and thus, it had a larger specific surface [38]. We preferred

the low adsorption so that the ASP agent would work further.

The adsorption was characterized by inputting a series of isothermal adsorption curves, which were expressed as Langmuir equation:

$$\text{Ad} = \frac{A \times c_i}{(l + B \times c_i)}, \tag{4}$$

where c_i is the component of fluid and A and B is the constant related to temperature. It is noted that the maximum adsorption is A/B.

(2) Porosity and Permeability Reduction. When the polymer passes through the porous medium, the adsorption due to chemical or mechanical retention would reduce the pore volume, thereby reducing the permeability of the formation. It could be characterized by the following formula:

$$\overline{K} = \frac{k}{R_k}, \tag{5}$$

where k is the initial permeability of the formation; R_k is the function of the adsorption and the residual resistance factor, which is defined by
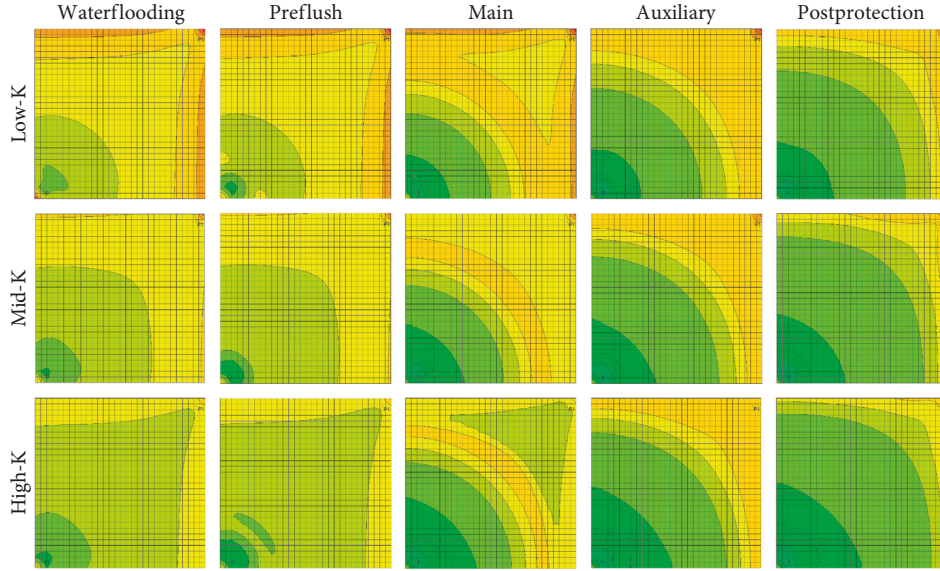
FIGURE 28: Pressure field of the numerical simulation model.

TABLE 4: Values of influence factors in RSM.

Variables	Value 1	Value 2	Value 3
Permeability (md) (k_r)	300	600	900
Variation coefficient (V_k)	0.27	0.41	0.54
Viscosity (cp) (μ)	30	40	50
Injection rate/(PV/a) (v)	0.2	0.25	0.3

$$R_k = 1 + (RRF - 1) \times \frac{AD}{ADMAXT}, \tag{6}$$

where AD is the cumulative adsorption of the polymer per unit volume rock, ADMAXT is the maximum of AD, and RRF is the residual resistance factor, which can be determined through experiments.

(3) Viscosity. In CMG STARS, we used the nonlinear mixture method to calculate the liquid mixed viscosity:

$$Ln(\mu_\alpha) = \sum_{i=1}^{n_{C \in S}} f(f_{\alpha_i}) \times Ln(\mu_{\alpha_i}) + N \times \sum_{i=1}^{n_{C \notin S}} f_{\alpha_i} \times Ln(\mu_{\alpha_i}), \tag{7}$$

where μ_α is the mixed viscosity, $\mu_{\alpha i}$ is the viscosity of component i, $f_{\alpha i}$ is the weight of ith noncritical component in the water or oil phase, and $f(f_{\alpha i})$ is the weight of ith critical component in the water or oil phase.

Besides, since the ASP system is a kind of non-Newtonian fluid, its rheology inevitably has an impact on its viscosity. The relationship between the shear velocity and Darcy velocity was described as [7]

$$\dot{\gamma} = \frac{\gamma_{\text{fac}} \times |u_l|}{\sqrt{k_{\text{abs}} \times k_{rl} \times \phi \times S_l}}, \tag{8}$$

where k_{abs} and Φ are the absolute permeability and porosity, u_l, k_{rl}, and S_l are the Darcy velocity, relative permeability, and saturation of some phase, respectively.

In addition, the salinity of formation water, emulsification, and degradation were also considered in the numerical model. Polymer, such as HPAM, is very sensitive to the salinity of formation water. Due to the presence of emulsification, emulsion that has higher apparent viscosity will form in the formation, thereby increasing the viscosity of the ASP agent. The degradation of the polymer contributes to a lower viscosity of the ASP agent. All of the above factors were integrated into the nonlinear mixture method.

(4) Inaccessible Pore Volume. As the macromolecular polymer flows through the porous medium, it may be confined to the tiny throat. And those pores that are not in contact with the flowing macromolecular polymer are called inaccessible pore volumes (IPV) [8]. It is also verified by the experiment [25]. So, the effective porosity of the ASP agent was defined as

$$\phi_p = (1 - IPV) \times \phi, \tag{9}$$

where ϕ is the initial porosity.

(5) IFT. Owing to the addition of surfactant and alkali, the interfacial tension is significantly reduced, resulting in an increase in the capillary number (Nc) and a decrease in residual oil saturation (S_{or}). The synergistic effect of the

TABLE 5: Final schemes used in RSM.

| Schemes	Permeability (mD)	Variation coefficient	Viscosity (MPa·s)	Injection rate (PV/a)
1	600	0.408	30	0.2
2	600	0.408	50	0.3
3	600	0.272	50	0.25
4	600	0.408	40	0.25
5	300	0.544	40	0.25
6	900	0.272	40	0.25
7	300	0.408	40	0.2
8	900	0.408	30	0.25
9	300	0.272	40	0.25
10	600	0.408	40	0.25
11	900	0.408	50	0.25
12	300	0.408	30	0.25
13	600	0.408	40	0.25
14	600	0.408	40	0.25
15	600	0.408	40	0.25
16	600	0.408	50	0.2
17	600	0.272	30	0.25
18	600	0.544	50	0.25
19	300	0.408	50	0.25
20	900	0.408	40	0.3
21	600	0.272	40	0.2
22	600	0.544	30	0.25
23	900	0.408	40	0.2
24	900	0.544	40	0.25
25	600	0.544	40	0.3
26	600	0.408	30	0.3
27	600	0.544	40	0.2
28	600	0.272	40	0.3
29	300	0.408	40	0.3
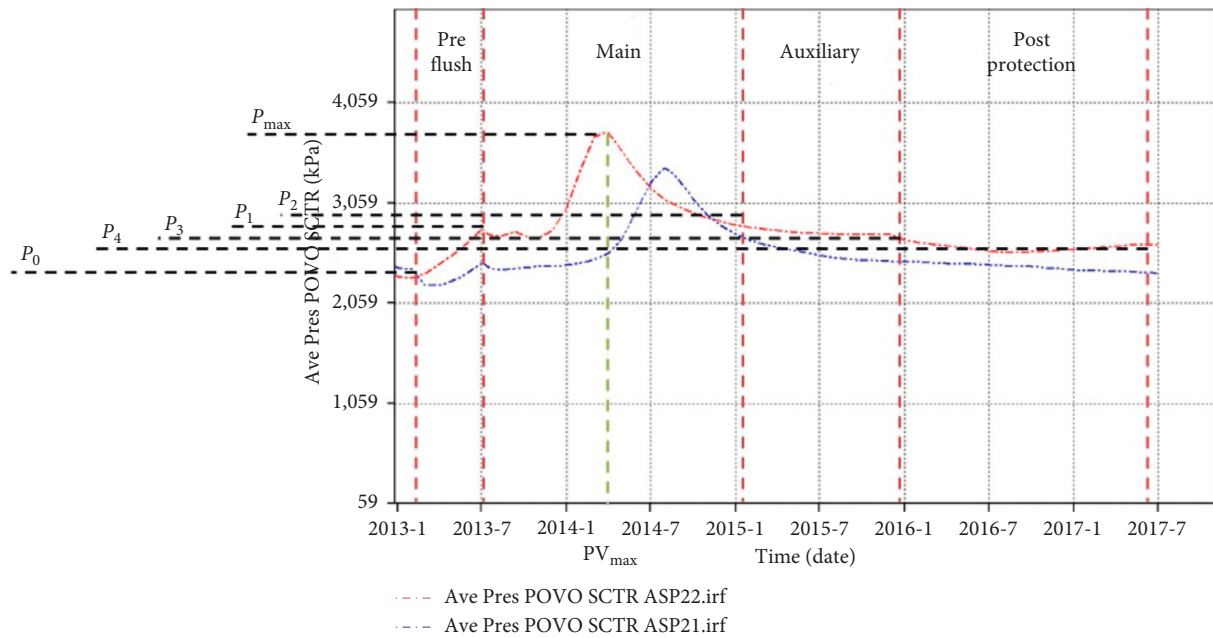
FIGURE 29: Objective pressure employed in RSM.
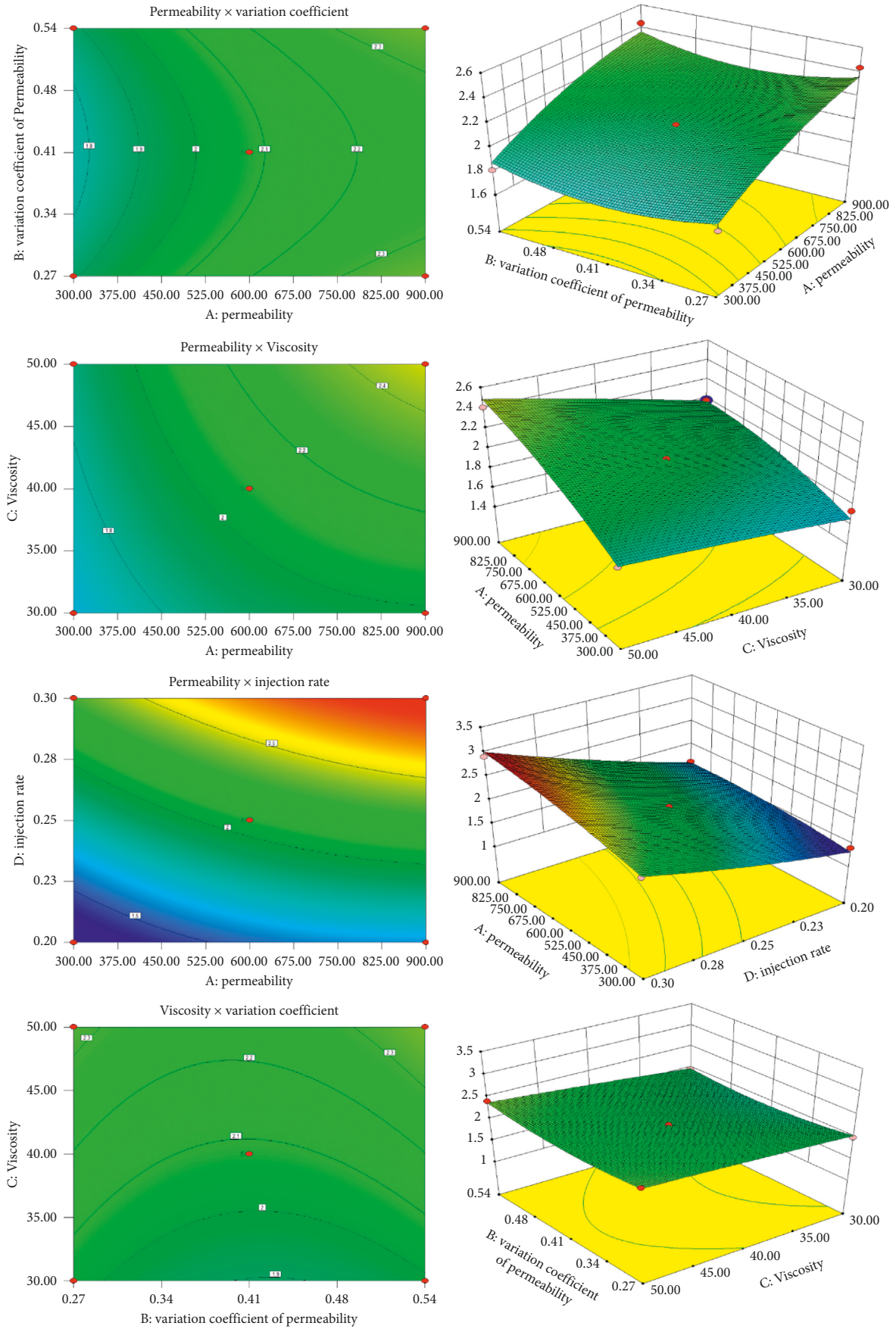
(a)

Figure 30: Continued.

(b)
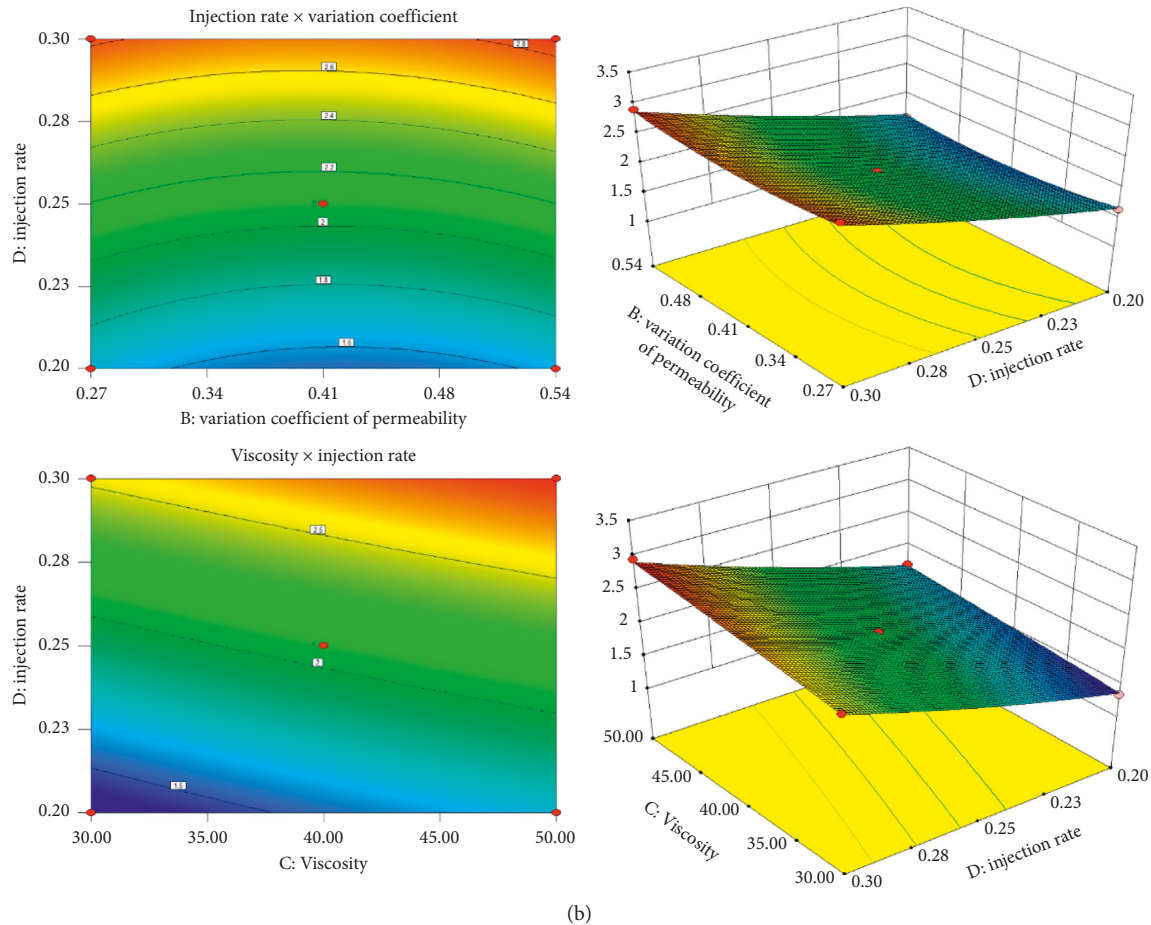
FIGURE 30: The response surface results.

surfactant and alkali was characterized by inputting the interfacial tension at different concentrations.

(6) Relative Permeability Curve. The relative permeability curve would alter during the ASP flooding. CMG STARS can solve this problem through interpolation methods (Figure 24).

A laboratory-scale $60\,cm \times 60\,cm \times 4.5\,cm$ model was established (Figure 25). All the parameters were identical to the experiment above.

The history match result is shown in Figures 26 and 27. The fitting degree of water cut was 92% and that of oil recovery was 90%.

Figure 28 shows the oil saturation calculated by numerical simulation. In the waterflooding stage, there was obvious water advancing along the mainstream line. The development effect increased with the increase of permeability, and the difference between layers was notable. In the ASP flooding, displacement effect on both sides of the mainstream line was significantly improved. The sweeping and displacement efficiency were also continuously improved, and the difference between layers was weakened.

3.7. Evolution Characteristics of Pressure Field of ASP Flooding. The evolution characteristics of pressure field of ASP flooding were going to be studied through response

surface methodology (RSM), including the heterogeneity, mobility ratio, injection rate, and formation permeability. And the values of these influence factors are listed in Table 4.

A total of 29 experimental groups were finally generated according to the RSM design requirements (Table 5). Substitute these data into the numerical simulation model, and we can obtain the development performance and data for future use.

We selected the following points, which are illustrated in Figure 29, as our objective functions in RSM:

(1) P_1: the pressure when the preflush slug stage ended

(2) P_{max}: the maximum pressure of the main slug stage

(3) P_2: the pressure when the main slug ended

(4) P_3: the pressure when the auxiliary slug ended

(5) P_4: the pressure when the postprotection slug stage ended

(6) $(P_{max} - P_{wf})/(P_0 - P_{wf})$: the increase magnitude of pressure,

where P_{wf} is the well bottom pressure and P_0 is the pressure when the waterflooding ended.

(7) PV_{max}: The injection volume when P_{max} occurred

Then, RSM was carried out to explore the quantitative relationship between influence factors and our objective

functions. The response surface results are shown in Figure 30 (Take $(P_{\max} - P_{\text{wf}})/(P_0 - P_{\text{wf}})$ as an example). Analysing the response surfaces, we could obtain the conclusion that a larger increase magnitude of pressure was corresponding to a larger average permeability, a faster injection rate, and a higher viscosity. With the increase of variation coefficient, the increase magnitude of pressure declined primarily, which was followed by a rise. And the influence levels were sorted as injection rate > average permeability > viscosity > variation coefficient.

Hence, the response expression of the increase magnitude of pressure was acquired:

$$
\frac{(P_{\max} - P_{\text{wf}})}{(P_o - P_{\text{wf}})} = 2.65 - 1.1 \times 10^{-3} k_r - 6.92 V_k - 7.67
$$

$$
\times 10^{-3} \mu - 6\nu - 1.1 \times 10^{-4} k_r V_k + 2.7
$$

$$
\times 10^{-5} k_r \mu + 7 \times 10^{-3} k_r \nu + 0.02 V_k \mu
$$

$$
+ 3.37 V_k \nu + 0.036 \mu \nu - 8.1 \times 10^{-7} k_r^2
$$

$$
+ 6.35 V_k^2 - 1.1 \times 10^{-4} \mu^2 + 22 \nu^2
$$

$$(10)$$

and that of other objective functions emerged in the same way.

4. Conclusions

The following conclusions can be drawn from both experimental and numerical results:

(1) Pressure field proved to be an effective indicator for the development performance in the ASP flooding. Pressure in the main slug stage increased dramatically and began to decline in the auxiliary slug stage. The preflush slug stage contributed little to the average formation pressure.

(2) The low-permeability layer was favourable for the entry of low-viscosity injection fluid, thereby improving its development effect. The high-viscosity fluid preferred to improve the flow profile.

(3) The stronger heterogeneity resulted in the more prominent contradiction between the low-permeability recovery and profile improvement. Single-viscosity slug was difficult to meet this contradiction.

(4) The response surface methodology was used to determine the relationship between pressure field and development parameters.

Data Availability

The data used to support the findings of this study are available from the corresponding author upon request.

Conflicts of Interest

The authors declare that they have no conflicts of interest.

References

[1] J. Speight, *Enhanced Recovery Methods for Heavy Oil and Tar Sands*, Gulf Publishing Company, Houstan, TX, USA, 2009.

[2] S. A. Shedid, "Experimental investigation of alkaline/surfactant/polymer (ASP) flooding in low permeability heterogeneous carbonate reservoirs," in *Proceedings of the SPE North Africa Technical Conference and Exhibition*, vol. 16, Society of Petroleum Engineers, Cairo, Egypt, September 2015.

[3] A. A. Olajire and A. Abass, "Review of ASP EOR (alkaline surfactant polymer enhanced oil recovery) technology in the petroleum industry: prospects and challenges," *Energy*, vol. 77, pp. 963–982, 2014.

[4] D. Cuong, "Modeling and optimization of alkaline-surfactant-polymer flooding and hybrid enhanced oil recovery processes," *Journal of Petroleum Science and Engineering*, vol. 169, pp. 578–601, 2018.

[5] J. H. Burk, "Comparison of sodium carbonate, sodium hydroxide, and sodium orthosilicate for EOR," *SPE Reservoir Engineering*, vol. 2, no. 1, pp. 9–16, 1987.

[6] H. Mohammadi, M. Delshad, and G. A. Pope, "Mechanistic modeling of alkaline/surfactant/polymer floods," *SPE Reservoir Evaluation & Engineering*, vol. 12, no. 4, pp. 518–527, 2009.

[7] W. J. Cannella, C. Huh, and R. S. Seright, "Prediction of xanthan rheology in porous media," in *Proceedings of the SPE Annual Technical Conference and Exhibition*, vol. 16, Society of Petroleum Engineers, Houston, TX, USA, 1988.

[8] R. Dawson and R. B. Lantz, "Inaccessible pore volume in polymer flooding," *Society of Petroleum Engineers Journal*, vol. 12, no. 5, pp. 448–452, 1972.

[9] X. Zhao, J. Zhang, Q. He, and X. Tan, "Experimental study and application of anti-salt polymer aqueous solutions prepared by produced water for low-permeability reservoirs," *Journal of Petroleum Science and Engineering*, vol. 175, pp. 480–488, 2019.

[10] X. Zhao, X. Sun, J. Zhang, and B. Bai, "Gel composition and brine concentration effect on hydrogel dehydration subjected to uniaxial compression," *Journal of Petroleum Science and Engineering*, vol. 182, Article ID 106358, 2019.

[11] G. Zhao, J. Li, C. Gu, L. Li, Y. Sun, and C. Dai, "Dispersed particle gel-strengthened polymer/surfactant as a novel combination flooding system for enhanced oil recovery," *Energy & Fuels*, vol. 32, no. 11, pp. 11317–11327, 2018.

[12] J. J. Sheng, "Chapter 9—ASP fundamentals and field cases outside China," in *Enhanced Oil Recovery Field Case Studies*, J. J. Sheng, Ed., pp. 189–201, Gulf Professional Publishing, Boston, MA, USA, 2013.

[13] R. Fortenberry, "Experimental demonstration and improvement of chemical EOR techniques in heavy oils," Master thesis, University of Texas at Austin, Austin, TX, USA, 2013.

[14] C. Huh, "Interfacial tensions and solubilizing ability of a microemulsion phase that coexists with oil and brine," *Journal of Colloid and Interface Science*, vol. 71, no. 2, pp. 408–426, 1979.

[15] G. Shutang and Q. Gao, "Recent progress and evaluation of ASP flooding for EOR in daqing oil field," in *Proceedings of the SPE EOR Conference at Oil & Gas West Asia*, vol. 7, Society of Petroleum Engineers, Muscat, Oman, April 2010.

[16] E. Amirian, M. Dejam, and Z. Chen, "Performance forecasting for polymer flooding in heavy oil reservoirs," *Fuel*, vol. 216, pp. 83–100, 2018.

[17] D. Wang, "Viscous-elastic polymer can increase microscale displacement efficiency in cores," in *Proceedings of the SPE Annual Technical Conference and Exhibition*, vol. 10, Society of Petroleum Engineers, Dallas, TX, USA, October 2000.

[18] Aitkulov, *Two-dimensional ASP Flood for a Viscous Oil. Master Thesis*, University of Texas at Austin, Austin, TX, USA, 2014.

[19] K. K. Mohanty, "Multiphase flow in porous media: III. Oil mobilization, transverse dispersion, and wettability," in *Proceedings of the SPE Annual Technical Conference and Exhibition*, vol. 21, Society of Petroleum Engineers, San Francisco, CA, USA, 1983.

[20] M. Delshad, D. Bhuyan, G. A. Pope, and L. W. Lake, "Effect of capillary number on the residual saturation of a three-phase micellar solution," in *Proceedings of the SPE Enhanced Oil Recovery Symposium*, 1986.

[21] X. A. Yue, Y. F. Wang, and K. L. Wang, *Basis for Enhanced Oil Recovery*, Petroleum Industry Press Publishing, Beijing, China, 2007.

[22] R. Saha, R. V. S. Uppaluri, and P. Tiwari, "Influence of emulsification, interfacial tension, wettability alteration and saponification on residual oil recovery by alkali flooding," *Journal of Industrial and Engineering Chemistry*, vol. 59, pp. 286–296, 2018.

[23] J. J. Sheng, "A comprehensive review of alkaline-surfactant-polymer (ASP) flooding," in *Proceedings of the SPE Western Regional & AAPG Pacific Section Meeting 2013 Joint Technical Conference*, vol. 20, Society of Petroleum Engineers, Monterey, CA, USA, April 2013.

[24] X. An Yue et al., "Calculation of IPR curves of oil wells for polymer flooding reservoirs," in *Proceedings of the SPE Annual Technical Conference and Exhibition*, vol. 9, Society of Petroleum Engineers, San Antonio, TX, USA, October 1997.

[25] M. Pancharoen, M. R. Thiele, and A. Robert Kovscek, "Inaccessible pore volume of associative polymer floods," in *Proceedings of the SPE Improved Oil Recovery Symposium*, vol. 15, Society of Petroleum Engineers, Tulsa, OK, USA, April 2010.

[26] K. Panthi, H. Sharma, and K. K. Mohanty, "ASP flood of a viscous oil in a carbonate rock," *Fuel*, vol. 164, pp. 18–27, 2016.

[27] L. Fu, G. Zhang, J. Ge et al., "Study on organic alkali-surfactant-polymer flooding for enhanced ordinary heavy oil recovery," *Colloids and Surfaces A: Physicochemical and Engineering Aspects*, vol. 508, pp. 230–239, 2016.

[28] S. S. Riswati, W. Bae, C. Park, A. K. Permadi, I. Efriza, and B. Min, "Experimental analysis to design optimum phase type and salinity gradient of alkaline surfactant polymer flooding at low saline reservoir," *Journal of Petroleum Science and Engineering*, vol. 173, pp. 1005–1019, 2019.

[29] X. Han, I. Kurnia, Z. Chen, J. Yu, and G. Zhang, "Effect of oil reactivity on salinity profile design during alkaline-surfactant-polymer flooding," *Fuel*, vol. 254, Article ID 115738, 2019.

[30] Y. Ge, S. Li, and X. Zhang, "Optimization for ASP flooding based on adaptive rationalized haar function approximation," *Chinese Journal of Chemical Engineering*, vol. 26, no. 8, pp. 166–173, 2018.

[31] M. Delshad, C. Han, F. K. Veedu, and G. A. Pope, "A simplified model for simulations of alkaline–surfactant–polymer floods," *Journal of Petroleum Science and Engineering*, vol. 108, pp. 1–9, 2013.

[32] M. Bai, Z. Zhang, X. Cui, and K. Song, "Studies of injection parameters for chemical flooding in carbonate reservoirs," *Renewable and Sustainable Energy Reviews*, vol. 75, pp. 1464–1471, 2017.

[33] S. Keshtkar, M. Sabeti, and A. H. Mohammadi, "Numerical approach for enhanced oil recovery with surfactant flooding," *Petroleum*, vol. 2, no. 1, pp. 98–107, 2016.

[34] A. M. Alsofi, J. S. Liu, M. Han, and S. Aramco, "Numerical simulation of surfactant–polymer coreflooding experiments for carbonates," *Journal of Petroleum Science and Engineering*, vol. 111, pp. 184–196, 2013.

[35] J. Li, L. Niu, and X. Lu, "Performance of ASP compound systems and effects on flooding efficiency," *Journal of Petroleum Science and Engineering*, vol. 178, pp. 1178–1193, 2019.

[36] Z. Wang, T. Yu, X. Lin, X. Wang, and L. Su, "Chemicals loss and the effect on formation damage in reservoirs with ASP flooding enhanced oil recovery," *Journal of Natural Gas Science and Engineering*, vol. 33, pp. 1381–1389, 2016.

[37] J. J. Sheng, *Modern Chemical Enhanced Oil Recovery: Theory and Practice*, Elsevier, Amsterdam, Netherlands, 2011.

[38] J. J. Sheng, "What type of surfactants should be used to enhance spontaneous imbibition in shale and tight reservoirs?" *Journal of Petroleum Science and Engineering*, vol. 159, pp. 635–643, 2017.

WILEY | Hindawi

Research Article

Interaction and Adsorption of Hydrophobically Modified Polyacrylamide on Silica and Asphaltene Surfaces

Wenjie Zou [iD],[1] **Zichuan Fang,**[1] **Zhijun Zhang** [iD],[2] **and Zhenzhen Lu** [iD][3]

[1]*Civil and Resource Engineering School, University of Science and Technology Beijing, Beijing 100083, China*
[2]*School of Chemical and Environmental Engineering, China University of Mining and Technology, Beijing, China*
[3]*Department of Chemical and Materials Engineering, University of Alberta, Edmonton, AB T6G 1H9, Canada*

Correspondence should be addressed to Zhijun Zhang; zhijunzhang@cumtb.edu.cn and Zhenzhen Lu; zhenzhen@ualberta.ca

The adsorption of polymers affects the cost and oil recovery in oil reservoir exploitation and the flocculation effect in the treatment of oil sand tailings. The adhesion and adsorption of a hydrophobically modified polyacrylamide (HMPAM), i.e., P(AM-NaAA-C_{16}DMAAC), on silica and asphaltene were investigated using surface force measurements, thermodynamic analysis and quartz crystal microbalance with dissipation (QCM-D) measurement. Our study indicates that HMPAM polymer has strong interaction with both silica and asphaltene. The adhesion force of HMPAM on silica was stronger than that on asphaltene surface. Consistently, the adsorption of HMPAM was also greater on silica surface, with a more rigid layer formed on the surface. For HMPAM/silica system, the attractive interaction and the strong adhesion are mainly driven by the hydrogen bonding and electrostatic interaction. For HMPAM/asphaltene system, it is mainly due to hydrophobic interaction between the long hydrocarbon chains of HMPAM and asphaltene. Furthermore, continuous adsorption of HMPAM was detected and multiple layers formed on both silica and asphaltene surfaces, which can be attributed to the hydrophobic chains of HMPAM polymers. This work has illustrated the interaction mechanism of HMPAM polymer on hydrophilic silica and hydrophobic asphaltene surfaces, which provide insight into the industrial applications of hydrophobically modified polymer.

1. Introduction

Recently, special attention has been focused on the hydrophobically modified polyacrylamide containing relatively low amounts of hydrophobic monomers (~2 mol%). Different hydrophobic monomers were reported, such as di-alkyl substituted acrylamides di-*n*-propylacrylamide, di-*n*-octylacrylamide [1], *N,N*-dihexylacrylamide or *N,N*-diphenylacrylamide [2], *N*-octadecylacrylamide [3], sodium 2-acrylamido-tetradecane sulfonate [4], 3-acrylamido-2-hydroxypropyltriakylammonium chloride [5], poly(propylene glycol) monomethacrylate [6], isomeric 11-acrylamidoundecanoic acid [7], stearyl methylacrylate [8], sodium 9-(and 10)-acrylamidostearate [9], etc. Due to the intramolecular and intermolecular interaction between the hydrophobic groups, the enlargement of hydrodynamic volume of polymers increases the viscosity of hydrophobically modified polyacrylamide aqueous solutions, and intermolecular association may further enhance the viscosity [10]. The aqueous solution of these polymers is expected to show special properties,

including temperature, salt, and shear resistances [11, 12]. The viscosity of hydrophobically modified polyacrylamide solution does not decrease at high salinity when its concentration is larger than the critical aggregation concentration [13]. For example, a kind of hydrophobically modified polyacrylamide based novel functional polymer (RH-4) at the concentration of 2000 mg/L has lower the apparent viscosity as NaCl concentration increase until ~2000 mg/L but it increased with the NaCl concentration at 2000–8000 mg/L [14]. In a semi-dilute solution of polyacrylamide with hydrophobic *t*-octylacrylamide group (0.5 wt.%), the zero-shear viscosity decreases with salt concentration at low salt conditions (0~0.3 M KCl), while it displayed a monotonically increase with salt concentration at high salt conditions (0.3~4 M KCl) [15]. NaCl was found to promote the association and adsorption of a hydrophobically modified polyacrylamide on kaolin particles, resulting in higher flocculation efficiency [16]. The adsorption isotherms of a hydrophobically associating polyacrylamide on K-montmorillonite and on siliceous minerals, has shown different behaviors compared with a nonassociating

polymer [17]. Another kind of hydrophobically modified poly-acrylamide with monomers of acrylamide and 2-(methacryloy-loxyl) ethylhexadecyldimethylammonium bromide displays the adsorption of multilayer on natural sand [18]. Guo et al., systematically studied the flow behavior through porous media and microdisplacement performances of hydrophobically modified partially hydrolyzed polyacrylamide (HMHPAM) [19–21]. They found that hydrodynamic sizes of HMHPAMs were much more sensitive to the polymer concentration, filtration pressure, and associating monomer content than partially hydrolyzed poly-acrylamide, and had better an efficiency than glycerol and HPAM for displacing the residual oil trapped in the "dead" ends of flow channel at the same viscosity. With the excellent properties, hydrophobically modified polyacrylamide polymers have been applied in enhanced oil recovery (EOR) of oil reservoir exploitation [7, 22–26], emulsified oil removal from aqueous solution [27] and oil sand tailings treatment [28].

To be noted, the adsorption behavior of polyacrylamide directly affects its adsorption loss and the related cost [29, 30]. The adsorption retention loss of polymer solution in reservoir pores should not be too large, so that the polymer solution in deep reservoir can keep sufficient concentration, and the reservoir near the injection well will not be blocked by large amount of polymer adsorption, which will affect the oil recovery. Also, the adsorption of flocculants would influence the flocculation efficiency in oil sand tailings treatment. Therefore, the adsorption and interaction mechanism of polymer at different solid/liquid interfaces are important for the application of hydrophobically modified polyacrylamide.

In this work, a hydrophobically modified polyacrylamide (HMPAM) was synthesized with a hydrophobic monomer hexadecyl dimethyl allyl ammonium chloride (~0.3 mol%). The interaction and adsorption behaviors of HMPAM on silica and asphaltene surface were investigated using colloidal probe atomic force spectroscopy, thermodynamic analysis of interaction energy, and quartz crystal micro-balance with dissipation (QCM-D) monitoring technique. Our work revealed the fundamental interaction mechanisms between HMPAM and silica and asphaltene surface, which will benefit the development of polymers in oil reservoir exploitation and oil sand tailings treatment.

2. Experimental

2.1. Materials. HMPAM were synthesized using the procedures described in our previous work [31, 32]. Diiodomethane, glycerol, hydrogen peroxide and sulfuric acid were purchased from Fisher Scientific (China). Ethanol, methylbenzene, Sodium dodecyl sulfate (SDS) and sodium hydroxide (NaOH) were purchased from Shanghai Aladdin Bio-Chem Technology Co., Ltd. Toluene was purchased from Nanjing Reagent (China). Octadecyltrichlorosilane (OTS, ≥90%) was purchased from Sigma Aldrich, China. Water was purified by Milli-Q system. Nitrogen at 99.99+% purity levels was used to dry the surfaces. Silica sensors were purchased from Q-sense (Gothenburg, Sweden).

2.2. Preparation of Asphaltene Surfaces. Asphaltene was extracted from vacuum distillation feed Athabasca bitumen following the previous procedure [33, 34]. The asphaltene sample was dissolved in toluene at the concentration of 0.5 wt.%. The asphaltene-toluene solution was sonicated for 10 min and filtered through a 0.2 μm polytetrafluoroethylene filter (Nalgene) before use. Subsequently, the silica wafer was immersed in the piranha solution (7 : 3 vol./vol. concentrated H_2SO_4 : 30% H_2O_2) for 20 min and washed with ethyl alcohol. Then, the silica surface was rinsed thoroughly with copious amount of Milli-Q water and blown dry by nitrogen gas. Then the cleaned silica wafer was immersed in dilute asphaltene-toluene solution (0.005 wt.%) for 12 h at 25°C. Finally, the prepared asphaltene surface was washed by toluene and dried by nitrogen gas before use.

The asphaltene sensors for QCM-D were prepared by spin-coating asphaltene solution onto OTS-treated silica sensors following the procedures shown in the literature [31]. Briefly, silica sensor was washed with 2% SDS, milli-Q water and UV/ozone followed the cleaning protocols provided by the Biolin Scientific. OTS was deposited on silica wafer by the vapor deposition as reported [33, 35]. Several drops of asphaltene were spin-coated on the OTS-treated silica sensor. Then the sensor was placed in vacuum overnight to remove any residual toluene.

2.3. AFM Force Measurements. The interaction forces measurements between HMPAM and silica or asphaltene surface were conducted using an MFP-3D AFM instrument (Asylum Research, Santa Barbara, USA). The HMPAM functionalized silica probes were prepared under the catalysis of EDC/NHS as described in the literature [36]. The force measurements were conducted, also, as in the literature [36]. The aqueous solution for the AFM force measurements was 100 mM KCl. Force mapping mode was conducted to analyze the interactions for at least 100 times at more than 3 different areas of the silica or asphaltene surfaces.

2.4. Characterization. The surface morphologies of silica and asphaltene surface before and after adsorption of HMPAM were imaged by the tapping mode. The surface wettability was characterized by KRUSS DSA100 (Hamburg, Germany) instrument. The errors of the contact angles at more than 3 different areas were less than ±2%, and the average contact angles were used. The QCM-D analysis was carried out to measure the in-situ adsorption kinetics of HMPAM using a Q-sense E1 system (Q-sense, Gothenburg, Sweden).

3. Results and Discussion

Figure 1 shows the different wettability of silica and asphaltene surfaces. The water contact angles of silica and asphaltene surfaces were 36.7 ± 1.5° and 82.2 ± 2.1°. Asphaltene is more hydrophobic than silica surface. Both silica and asphaltene surfaces were submerged in 20 mg/L HMPAM of 100 mM KCl solution. After 3 hours, the surfaces were washed with 100 mM KCl solution, then the morphology of the surfaces was observed after being dried by nitrogen gas. In Figure 2, the
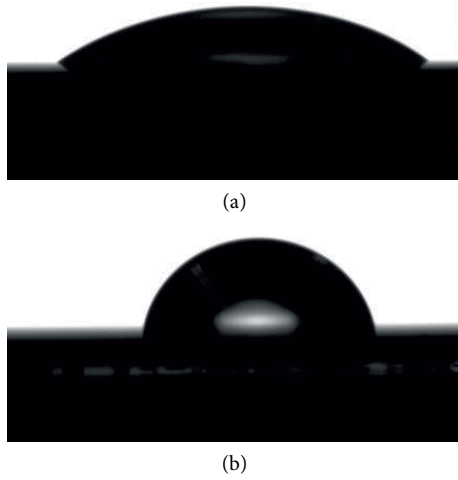
(a)

(b)

FIGURE 1: Water contact angle on (a) silica and (b) asphaltene surfaces.

AFM imaging shows silica exhibits a smooth and uniform morphology, and the root-mean-square surface roughness $\left(R_q\right)$ is only 0.06 nm. After adsorption of HMPAM, the R_q of silica surface increases to 0.75 nm. Differently, asphaltene surface is rougher with the R_q of 0.68 nm. After adsorption of HMPAM, the asphaltene surface becomes slightly smoother with R_q of 0.61 nm, which might be due to the large amount of HMPAM adsorption.

To measure the interaction between HAMPAM and silica and asphaltene, force measurement was carried out as shown in Figure 3. It shows an attraction between HMPAM and silica surface at up to 10 nm distance during approaching in 100 mM KCl solution (Figure 3(a)). It is also attraction between HMPAM and asphaltene surface (Figure 3(b)). But the attraction distance on asphaltene is longer up to 20 nm, which could attribute to the larger roughness of asphaltene surface and the hydrophobic interaction between the hydrophobic asphaltene surface and HMPAM. During retraction, jump-out behaviors were detected on both silica and asphaltene surfaces, indicating the adhesion between HMPAM and silica/asphaltene surface. Force mapping was carried out on silica and asphaltene surfaces to statistically obtain the adhesion forces. In Figure 3(c), the F_{adh} of HMPAM on silica surface was 3.30 ± 0.56 nN, slightly larger than on asphaltene surface at 2.96 ± 0.41 nN. This result indicates that the adhesion between HMPAM and silica surface is stronger than that between HMPAM and asphaltene surface.

The curved probe surface and flat substrate can be correlated according to the Johnson–Kendall–Roberts contact mechanics model [37, 38] as follows.

$$F_{\text{adh}} = 1.5\pi R W_{\text{adh}}, \tag{1}$$

where W_{adh} is the adhesion energy (mJ/m^2), R the radius of the probe (m).

The measured adhesion energies of HMPAM are 0.350 mJ/m^2 on silica and 0.278 mJ/m^2 on asphaltene, respectively. Generally, the adhesion interaction can be ascribed to van der

Waals force, electrostatic interaction, hydrogen-bonding and hydrophobic interaction. The van der Waals interaction is generally weak in the aqueous medium and only works in a few nanometers of the two surfaces. The Debye length, describing the range of the electric double layer was 0.96 nm in 100 mM KCl. Thus, for hydrophilic silica surface, the adhesion can be induced by both electrostatic interaction between amine group in HMPAM and silica surface, and hydrogen bonding interaction between the C=O, NH$_2$ groups of HMPAM and the –OH group on silica surface. Besides, the silica surface can be mildly hydrophobic with water contact angle of $36.7 \pm 1.5°$, according to the literature [39, 40]. There could be hydrophobic attraction between HMPAM and silica surface. For asphaltene surface, hydrophobic interactions may dominate the adhesion, which is between the hydrophobic domains on asphaltene surface and the long hydrocarbon chains of HMPAM. It indicates that HMPAM has the capability of attracting with both silica and asphaltene by various interactions.

Surface thermodynamic characterization of the HMPAM coated silica and asphaltene surfaces has been assessed to better understand the interaction of HMPAM on these surfaces. According to the Van Oss-Chaudhury-Good theory, the surface free energy of solid is composed of the non-polar part and polar part [41, 42]. The surface energy of solid can be calculated as follows.

$$\gamma_s = \gamma_s^{\text{LW}} + \gamma_s^{\text{AB}} = \gamma_s^{\text{LW}} + 2\left(\gamma_s^+ \gamma_s^-\right)^{1/2}, \tag{2}$$

where γ_s (mJ·m^{-2}) is the total surface free energy of solid, γ_s^{LW} (mJ·m^{-2}) the nonpolar part, referring to LIfshitz-van der Waals, γ_s^{AB} (mJ·m^{-2}) the polar part, referring to short range acid-base interaction forces, γ_s^+ (mJ·m^{-2}) the acid part and γ_s^- (mJ·m^{-2}) the base part. The interface free energy of solid and liquid is expressed:

$$\gamma_{\text{sl}} = \gamma_s + \gamma_1 - 2\left[\left(\gamma_s^{\text{LW}}\gamma_1^{\text{LW}}\right)^{1/2} + \left(\gamma_s^+\gamma_1^-\right)^{1/2} + \left(\gamma_s^-\gamma_1^+\right)^{1/2}\right]. \tag{3}$$

Young's equation [43] is as follows:

$$\gamma_s = \gamma_{\text{sl}} + \gamma_1\cos\theta, \tag{4}$$

$$\gamma_{\text{sl}} = \gamma_s^+ \gamma_s^- W_a, \tag{5}$$

where γ_1 (mN/m) is the surface tension of liquid, γ_{sl} (mN/m) the interfacial tension of solid and liquid, γ_l^+ (mN/m) the acid part of liquid, γ_l^- (mN/m) the base part of liquid, $\theta(°)$ the contact angle, the W_a (J) is a adhesion work.

Thus, combining the Equations (3), (4), and (5), there would be Equation (6):

$$W_a = \gamma_1(1 + \cos\theta) = 2\left[\left(\gamma_s^{\text{LW}}\gamma_1^{\text{LW}}\right)^{1/2} + \left(\gamma_s^+\gamma_1^-\right)^{1/2} + \left(\gamma_s^-\gamma_1^+\right)^{1/2}\right]. \tag{6}$$

Surface free energy can be calculated based on contact angles of three model liquids by the Equation (6). The surface tensions of three liquids, i.e., diiodomethane, glycerol and deionized water, were shown in Table 1. Contact angles of the model liquids on silica and asphaltene surfaces before and after the
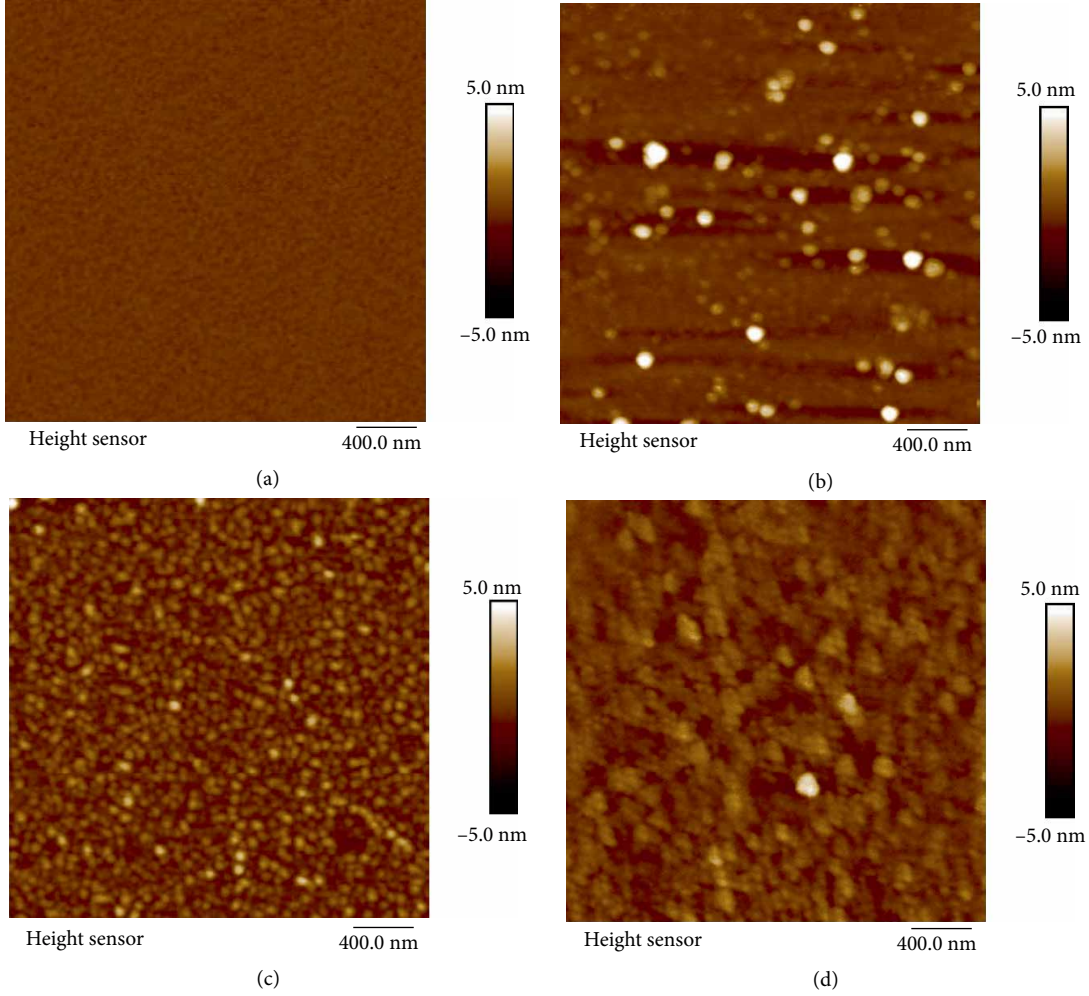
(a)

(b)

(c)

(d)

FIGURE 2: AFM images of different samples: (a) silica, (b) silica after adsorption of HMPAM, (c) asphaltene, and (d) asphaltene after adsorption of HMPAM.

adsorption of HMPAM were listed in Table 2. The group of equations was solved when the contact angles were substituted to Equation (6) to estimate the surface free energy and its components. The values of surface tension and components of the samples were collected in the Table 3.

The surface free energy of silica is 57.40 mJ/m^2, which agrees with the literature [45]. The γ_s^- of silica is 58.10 mJ/m^2, while that of asphaltene surface is 1.42 mJ/m^2. The γ_s^- is due to H-bonds, and the greater the γ_s^- is, the sample surface is more hydrophilic [42, 43]. It consists with the higher hydrophilicity of silica than asphaltene. After adsorption of HMPAM, the γ_s of asphaltene increased to 58.44 mJ/m^2, while its γ_s^- remarkably increased to 33.03 mJ/m^2. In contrast, the γ_s of silica increased slightly to 63.32 mJ/m^2. Its γ_s^{AB} increased from 12.57 mJ/m^2 to 19.64 mJ/m^2, while the γ_s^{LW} decreased from 44.83 mJ/m^2 to 43.68 mJ/m^2. To be noted, the surface free energy of both silica and asphaltene increased.

The free energy ΔG(mJ/m^2) of interactions between two solid surfaces can be calculated according to the following Equations [46].

TABLE 1: Surface tension and components (mN/m) of three model liquids [44].

Liquid	γ^{LW}	γ^+	γ^-	γ^{AB}	γ
Diiodomethane	50.80	0.00	0.00	0.00	50.80
Glycerol	34.00	3.92	57.40	30.00	64.00
Water	21.80	25.50	25.50	51.00	72.80

$$\Delta G_{adh} = \Delta G^{LW} + \Delta G^{AB}, \tag{7}$$

$$\Delta G^{LW} = 2 \times \left[\left(\gamma_w^{LW}\right)^{1/2} - \left(\gamma_2^{LW}\right)^{1/2} \right] \times \left[\left(\gamma_1^{LW}\right)^{1/2} - \left(\gamma_w^{LW}\right)^{1/2} \right], \tag{8}$$

$$\Delta G^{AB} = 2 \times \left\{ \left(\gamma_w^+\right)^{1/2} \times \left[\left(\gamma_1^-\right)^{1/2} + \left(\gamma_2^-\right)^{1/2} - \left(\gamma_w^-\right)^{1/2} \right] \right.$$
$$\left. + \left(\gamma_w^-\right) \times \left[\left(\gamma_1^+\right)^{1/2} + \left(\gamma_2^+\right)^{1/2} - \left(\gamma_w^+\right)^{1/2} \right] - \left(\gamma_1^+ \gamma_2^-\right)^{1/2} - \left(\gamma_1^- \gamma_2^+\right)^{1/2} \right\}, \tag{9}$$

TABLE 2: Contact angles of three model liquids on different surfaces.

Different surfaces	Contact angle (°)		
	Diiodomethane	Glycerol	Water
Asphaltene	55.6	57.9	82
Silica	28.5	27.5	36.7
HMPAM on asphaltene	34.5	29.2	34.3
HMPAM on silica	31.3	15.7	22

TABLE 3: Surface free energy (mJ/m^2) of different surfaces.

Different surfaces	γ_s^{LW}	γ_s^+	γ_s^-	γ_s^{AB}	γ_s
Asphaltene	31.12	3.48	1.42	4.45	35.57
Silica	44.83	0.68	58.10	12.57	57.40
HMPAM on asphaltene	42.27	1.98	33.03	16.17	58.44
HMPAM on silica	43.68	2.51	38.4	19.64	63.32

TABLE 4: Free energy of interaction (mJ/m^2) between surfaces.

Surfaces	ΔG^{LW}	ΔG^{AB}	ΔG_{adh}
Two asphaltene surfaces	−1.65	−49.14	−50.80
Two silica surfaces	−8.21	43.48	35.26
Asphaltene and silica	−3.69	−16.22	−19.90
HMPAM adsorbed silica and asphaltene	−3.53	−12.63	−16.16
Two HMPAM adsorbed silica	−7.53	−30.68	−38.21
HMPAM adsorbed silica and silica	−7.86	−41.13	−48.99
Two HMPAM adsorbed asphaltene surfaces	−6.72	−33.67	−40.39
HMPAM adsorbed asphaltene and HMPAM adsorbed silica	−7.11	−33.39	−40.50

(a)

(b)

(c)

FIGURE 3: Typical force-distance profiles of the HMPAM-coated silica probe on surfaces in 100 mM KCl solution: (a) silica, (b) asphaltene, and (c) summary of the adhesion.
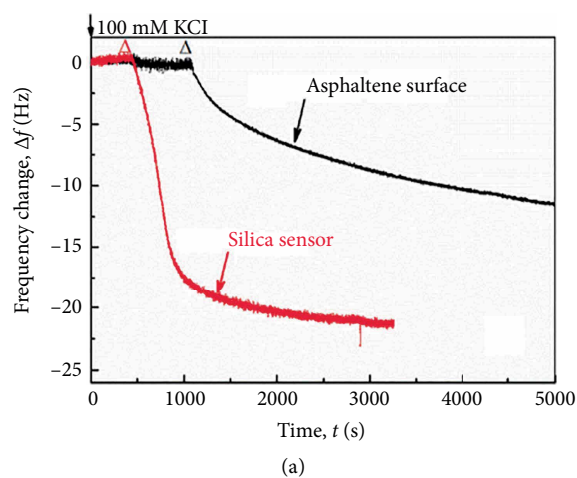
(a)
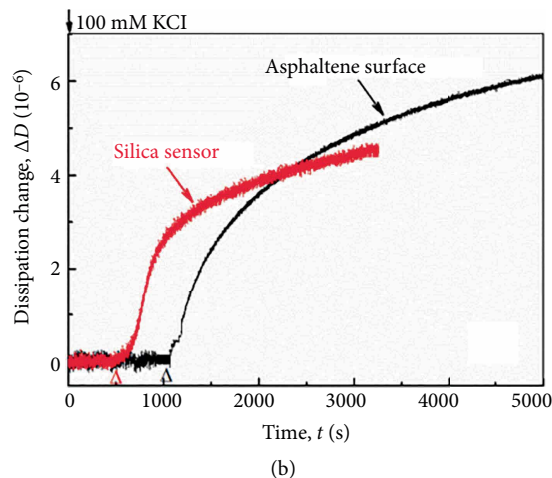
(b)

FIGURE 4: Changes of (a) frequency Δf and (b) dissipation ΔD obtained by QCM-D associated with adding 20 mg/L HMPAM in 100 mM KCl solution on silica and asphaltene sensors. (Δ-start injection).

where γ_1 and γ_2 are the surface energy parameters of two solid surfaces, and γ_w is the surface tension of water. When the value of ΔG is negative, the adhesion process will occur spontaneously. The more negative the value of ΔG is, the more likely the adhesion process happens. In Table 4, the ΔG of the two

silica surfaces is positive, and that of the two asphaltene surface is negative, implying that the adhesion of silica would not happen, and adhesion between two asphaltene surfaces could occur spontaneously. The ΔG_{adh} between silica and asphaltene is -19.90 mJ/m^2 indicating that the coating of asphaltene on silica could occur.

The values of ΔG_{adh} between HMPAM adsorbed silica and asphaltene, silica or HMPAM adsorbed silica, are all negative, suggesting that all the above pairs of surfaces would adhere spontaneously. The absolute value of ΔG_{adh} between HMPAM adsorbed silica and silica is the largest. The values of ΔG_{adh} between HMPAM adsorbed asphaltene and HMPAM adsorbed asphaltene or HMPAM adsorbed silica are both negative. Both the thermodynamic calculations and AFM force measurements demonstrate that the adhesions of HMPAM on silica and asphaltene surfaces are spontaneous processes.

The adsorption of HMPAM on silica and asphaltene surfaces in 100 mM KCl were determined by QCM-D to verify the interaction mechanism. Figure 4(a) shows, the changes of frequency (Δf) of asphaltene and silica sensors decreased from the baseline to -14.6 Hz, and -21.5 Hz, respectively, indicating the adsorption amount of HMPAM on the silica surface was larger than that on the asphaltene surface. The adsorption time of HMPAM on asphaltene was longer which means the adsorption rate of HMPAM on asphaltene was slower than that on silica sensor. Meanwhile in Figure 4(b), the changes of dissipation (ΔD) of asphaltene surface (7.1×10^{-6} at adsorption equilibrium) was larger than that of silica (5.0×10^{-6} at adsorption equilibrium), indicating that the adsorption layer was less dissipative on silica surface. This result agrees with stronger interaction between HMPAM and silica surface by the AFM force measurement. Attractive hydrophobic force between HMPAM polymers led to continuous adsorption and formed multiple layers of HMPAM, which induces higher adsorption amount compared with the commercial PAM in previous study [36].

4. Summary and Conclusions

In this work, the adsorption and adhesion of a hydrophobically modified polymer HMPAM on silica and asphaltene was investigated using surface force measurements, thermodynamic analysis and QCM-D measurement. The surface force measurements and thermodynamic analysis of interaction energy have clearly shown the HMPAM have strong attractive interaction with both silica and asphaltene. The results show that the HMPAM polymer has strong attractive interaction with both silica and asphaltene. The adhesion force of HMPAM on silica surface (3.30 ± 0.56 nN) is stronger than that on asphaltene surface (2.96 ± 0.41 nN). QCM-D measurement suggests the adsorption amount of HMPAM on the silica surface (Δf of -21.5 Hz) was larger than that on the asphaltene surface (Δf of -14.6 Hz). And the adsorption layer was less dissipative on silica surface (ΔD of 5.0×10^{-6}), agreeing with the stronger adhesion force. On silica surface, the attraction and adhesion can be mainly induced by (1) hydrogen bonding between the C=O, NH$_2$ groups in HMPAM and the –OH group of silica surface; (2) electrostatic interaction between

HMPAM and silica surface. On asphaltene surface, the attraction and adhesion may be attributed to hydrophobic interactions between the long hydrocarbon chains of HMPAM and asphaltene. Furthermore, it was revealed that HMPAM performed continuous adsorption and formed multiple layers on both silica and asphaltene surfaces, which could be attributed to the hydrophobic chains of HMPAM polymers. This work has illustrated the interaction mechanism of HMPAM on hydrophilic silica and hydrophobic asphaltene surfaces, which provide insight into the development of polymers for applications in oil reservoir exploitation and oil sand tailings treatment.

Data Availability

The data used to support the findings of this study are available from the corresponding author upon request.

Conflicts of Interest

The authors declare that they have no conflicts of interest.

Acknowledgments

References

[1] W. Xue, I. W. Hamley, V. Castelletto, and P. D. Olmsted, "Synthesis and characterization of hydrophobically modified polyacrylamides and some observations on rheological properties," *European Polymer Journal*, vol. 40, no. 1, pp. 47–56, 2004.

[2] M. Pabon, J. M. Corpart, J. Selb, and F. Candau, "Synthesis in inverse emulsion and associating behavior of hydrophobically modified polyacrylamides," *Journal of Applied Polymer Science*, vol. 91, no. 2, pp. 916–924, 2004.

[3] Z. Zhu, O. Jian, S. Paillet, D. Jacques, and B. Grassl, "Hydrophobically modified associating polyacrylamide (HAPAM) synthesized by micellar copolymerization at high monomer concentration," *European Polymer Journal*, vol. 43, no. 3, pp. 824–834, 2007.

[4] B. Gao, L. Jiang, and K. Liu, "Microstructure and association property of hydrophobically modified polyacrylamide of a new family," *European Polymer Journal*, vol. 43, no. 10, pp. 4530–4540, 2007.

[5] K. E. Lee, B. T. Poh, N. Morad, and T. T. Teng, "Synthesis and characterization of hydrophobically modified cationic polyacrylamide with low concentration of cationic monomer," *Journal of Macromolecular Science, Part A: Pure and Applied Chemistry*, vol. 46, no. 3, pp. 240–249, 2009.

[6] L. M. Gouveia, B. Grassl, and A. J. Müller, "Synthesis and rheological properties of hydrophobically modified polyacrylamides with lateral chains of poly(propylene oxide)

oligomers," *Journal of Colloid and Interface Science*, vol. 333, no. 1, pp. 152–163, 2009.

[7] Q. B. Yang, C. L. Song, Q. Chen, P. P. Zhang, and P. X. Wang, "Synthesis and aqueous solution properties of hydrophobically modified anionic acrylamide copolymers," *Journal of Polymer Science Part B-Polymer Physics*, vol. 46, no. 22, pp. 2465–2474, 2010.

[8] Y. J. Che, Y. Tan, J. Cao, H. Xin, and G. Y. Xu, "Synthesis and properties of hydrophobically modified acrylamide-based polysulfobetaines," *Polymer Bulletin*, vol. 66, no. 1, pp. 17–35, 2011.

[9] C. Lu, W. Li, Y. Tan et al., "Synthesis and aqueous solution properties of hydrophobically modified polyacrylamide," *Journal of Applied Polymer Science*, vol. 131, no. 18, pp. 9162–9169, 2014.

[10] Q. Deng, H. Li, L. Ying, X. Cao, Y. Yong, and X. Song, "Rheological properties and salt resistance of a hydrophobically associating polyacrylamide," *Australian Journal of Chemistry*, vol. 67, no. 10, pp. 1396–1402, 2014.

[11] Y. Lu, H. Wu, Z. Meng et al., "Salt effect on hydrophobically modified polyacrylamide-containing crude oil emulsions: stability and rheology study," *Colloid and Polymer Science*, vol. 296, no. 3, pp. 515–527, 2018.

[12] G. Jiang, L. Huang, B. Li, C. Lv, R. Li, and F. Liu, "Synthesis characterization rheological behavior and shear response of hydrophobically modified polyacrylamide and network structure of its microhydrogel," *Journal of Applied Polymer Science*, vol. 123, no. 1, pp. 66–76, 2012.

[13] G. Dupuis, J. Rigolini, G. Clisson, D. Rousseau, R. Tabary, and B. Grassl, "Determination of the macromolecular dimensions of hydrophobically modified polymers by micellar size exclusion chromatography coupled with multiangle light scattering," *Analytical Chemistry*, vol. 81, no. 21, pp. 8993–9001, 2009.

[14] B. Sarsenbekuly, W. Kang, H. Fan et al., "Study of salt tolerance and temperature resistance of a hydrophobically modified polyacrylamide based novel functional polymer for EOR," *Colloids and Surfaces A-Physicochemical and Engineering Aspects*, vol. 514, pp. 91–97, 2017.

[15] L. M. Gouveia, S. Paillet, A. Khoukh, B. Grassl, and A. J. Müller, "The effect of the ionic strength on the rheological behavior of hydrophobically modified polyacrylamide aqueous solutions mixed with sodium dodecyl sulfate (SDS) or cetyltrimethylammonium p-toluenesulfonate (CTAT)," *Colloid Surface*, vol. 322, no. 1–3, pp. 211–218, 2008.

[16] H. Ren, L. I. Ye, S. Zhang, J. Wang, and Z. Luan, "Flocculation of kaolin suspension with the adsorption of *NN*-disubstituted hydrophobically modified polyacrylamide," *Colloids and Surfaces A: Physicochemical and Engineering Aspects*, vol. 317, no. 1–3, pp. 388–393, 2008.

[17] J. F. Argillier, A. Audibert, J. Lecourtier, M. Moan, and L. Rousseau, "Solution and adsorption properties of hydrophobically associating water-soluble polyacrylamides," *Colloids and Surfaces A-Physicochemical and Engineering Aspects*, vol. 113, no. 3, pp. 247–257, 1996.

[18] H. Lu and Z. Huang, "Solution and adsorption properties of hydrophobically associating polyacrylamide prepared in inverse microemulsion polymerization," *Journal of Macromolecular Science Part A-Pure and Applied Chemistry*, vol. 46, no. 4, pp. 412–418, 2009.

[19] Y.-J. Guo, J.-X. Liu, X.-M. Zhang et al., "Solution property investigation of combination flooding systems consisting of gemin-non-ionic mixed surfactant and hydrophobically associating polyacrylamide for enhanced oil recovery," *Energy & Fuels*, vol. 26, no. 4, pp. 2116–2123, 2012.

[20] Y. Guo, Y. Liang, M. Cao et al., "Flow behavior and viscous-oil-microdisplacement characteristics of hydrophobically modified partially hydrolyzed polyacrylamide in a repeatable quantitative visualization micromodel," *Society of Petroleum Engineers Journal*, vol. 22, no. 5, pp. 1448–1466, 2017.

[21] Y. Guo, J. Hu, X. Zhang, R. Feng, and H. Li, "Flow behavior through porous media and microdisplacement performances of hydrophobically modified partially hydrolyzed polyacrylamide," *Society of Petroleum Engineers Journal*, vol. 21, no. 3, pp. 688–705, 2016.

[22] A. M. S. Maia, R. Borsali, and R. C. Balaban, "Comparison between a polyacrylamide and a hydrophobically modified polyacrylamide flood in a sandstone core," *Materials Science and Engineering: C*, vol. 29, no. 2, pp. 505–509, 2009.

[23] C. Zou, T. Gu, P. Xiao, T. Ge, M. Wang, and K. Wang, "Experimental study of cucurbit uril derivatives modified acrylamide polymer for enhanced oil recovery," *Industrial & Engineering Chemistry Research*, vol. 53, no. 18, pp. 7570–7578, 2014.

[24] X.-M. Zhang, Y.-J. Guo, J.-X. Liu et al., "Adaptability of a hydrophobically associating polyacrylamide mixed-surfactant combination flooding system to the shengli chengdao oilfield," *Journal of Applied Polymer Science*, vol. 131, no. 12, 2014.

[25] N. Lai, D. Wan, Z. Ye et al., "Water-soluble acrylamide hydrophobically associating polymer: synthesis characterization and properties as EOR chemical," *Journal of Applied Polymer Science*, vol. 129, no. 4, pp. 1888–1896, 2013.

[26] H.-X. Chen, H.-M. Tang, X.-Y. Wu, Y.-G. Liu, J.-H. Bai, and F. Zhao, "Synthesis, characterization, and property evaluation of a hydrophobically modified polyacrylamide as enhanced oil recovery chemical," *Journal of Dispersion Science and Technology*, vol. 37, no. 4, pp. 486–495, 2016.

[27] J. Y. Ma, J. Shi, L. Ding et al., "Removal of emulsified oil from water using hydrophobic modified cationic polyacrylamide flocculants synthesized from low-pressure UV initiation," *Separation and Purification Technology*, vol. 197, no. 1, pp. 407–417, 2018.

[28] R. Hripko, V. Vajihinejad, F. LopesMotta, and J. B. P. Soares, "Enhanced flocculation of oil sands mature fine tailings using hydrophobically modified polyacrylamide copolymers," *Global Challenges*, vol. 2, no. 3, Article ID 1700135, 2018.

[29] S. Rellegadla, G. Prajapat, and A. Agrawal, "Polymers for enhanced oil recovery: fundamentals and selection criteria," *Applied Microbiology and Biotechnology*, vol. 101, no. 11, pp. 4387–4402, 2017.

[30] M. S. Kamal, A. S. Sultan, U. A. Al-Mubaiyedh, and I. A. Hussein, "Review on polymer flooding: rheology, adsorption, stability, and field applications of various polymer systems," *Polymer Reviews*, vol. 55, no. 3, pp. 491–530, 2015.

[31] W. Zou, L. Gong, J. Huang, Z. Zhang, C. Sun, and H. Zeng, "Adsorption of hydrophobically modified polyacrylamide P(AM-NAAA-C16DMAAC) on model Coal and clay surfaces and the effect on selective flocculation of fine coal," *Minerals Engineering*, vol. 142, p. 105887, 2019.

[32] H. J. Luo, L. Q. Zhao, J. L. Dai, and Z. J. Pan, "Synthesis of hydrophobically modified AM/NaAA/C16 DMAAC copolymer," *Advances in Fine Petrochemicals*, vol. 9, no. 2, pp. 12–14, 2008.

[33] L. Zhang, L. Xie, C. Shi, J. Huang, Q. Liu, and H. Zeng, "Mechanistic understanding of asphaltene surface interactions in aqueous media," *Energy & Fuels*, vol. 31, no. 4, pp. 3348–3357, 2017.

[34] C. Shi, L. Zhang, L. Xie et al., "Surface interaction of water-in-oil emulsion droplets with interfacially active asphaltenes," *Langmuir*, vol. 33, no. 5, pp. 1265–1274, 2017.

[35] J. Huang, X. Liu, X. Qiu et al., "Octadecyltrichlorosilane deposition on mica surfaces: insights into the interface interaction mechanism," *The Journal of Physical Chemistry B*, vol. 121, no. 14, pp. 3151–3161, 2017.

[36] W. Zou, L. Gong, J. Huang et al., "Probing the adsorption and interaction mechanisms of hydrophobically modified polyacrylamide P(AM-NaAA-C16DMAAC) on model coal surface: impact of salinity," *Minerals Engineering*, vol. 141, p. 105841, 2019.

[37] J. N. Israelachvili, *Intermolecular and Surface Forces*, Academic Press, 2011.

[38] H. Zeng, *Polymer Adhesion, Friction and Lubrication*, Wiley & Sons, 2013.

[39] A. Kanta, R. Sedev, and J. Ralston, "Thermally and photoinduced changes in the water wettability of low-surface-area silica and titania," *Langmuir*, vol. 21, no. 6, pp. 2400–2407, 2005.

[40] M. L. Gee, T. W. Healy, and L. R. White, "Hydrophobicity effects in the condensation of water films on quartz," *Journal of Colloid and Interface Science*, vol. 140, no. 2, pp. 450–465, 1990.

[41] C. J. Van Oss, R. J. Good, and M. K. Chaudhury, "The role of van der waals forces and hydrogen bonds in "hydrophobic interactions" between biopolymers and low energy surfaces," *Journal of Colloid and Interface Science*, vol. 111, pp. 378–390, 1986.

[42] C. J. Van Oss, R. J. Good, and M. K. Chaudhury, "Additive and nonadditive surface tension components and the interpretation of contact angles," *Langmuir*, vol. 4, no. 4, pp. 884–891, 1988.

[43] W. Zou, Y. Cao, J. Liu, W. Li, and C. Liu, "Wetting process and surface free energy components of two fine liberated middling bituminous coals and their flotation behaviors," *Powder Technology*, vol. 246, pp. 669–676, 2013.

[44] C. Zhang, L. Gong, L. Xiang et al., "Deposition and adhesion of polydopamine on the surfaces of varying wettability," *ACS Applied Materials & Interfaces*, vol. 9, no. 36, pp. 30943–30950, 2017.

[45] M. L. Gonzalez-Martin, B. Jańczuk, L. Labajos-Broncano, J. M. Bruque, and C. M. Gonzalez-Garcia, "Analysis of the silica surface free energy by the imbibition technique," *Journal of Colloid and Interface Science*, vol. 240, no. 2, pp. 467–472, 2001.

[46] C. J. Van Oss, "Acid-base interfacial interactions in aqueous media," *Colloids and Surfaces A-Physicochemical and Engineering Aspects*, vol. 78, pp. 1–49, 1993.

WILEY | Hindawi

Research Article

Effect of Temperature and Accelerator on Gel Time and Compressive Strength of Resin Anchoring Agent

Xiaohu Liu [iD],[1] **Zhishu Yao** [iD],[1] **Weipei Xue** [iD],[1,2] and **Xiang Li** [iD][1]

[1]*School of Civil Engineering and Architecture, Anhui University of Science and Technology, Huainan 232001, China*
[2]*Post-Doctoral Research Station of Safety Science and Engineering, Anhui University of Science and Technology, Huainan 232001, China*

Correspondence should be addressed to Zhishu Yao; zsyao@aust.edu.cn

In this study, we examined the effects of different temperatures and accelerators on the gelation (gel) time and compressive strength of a Polyethylene Terephthalate (PET)-type unsaturated polyester resin anchorage agent. First, the formation temperature of 20–70°C was simulated using self-made test equipment. N,N-Dimethylaniline (DMA), N,N-dimethylp-toluidine (DMT), and hydroquinone were selected as accelerators to determine gel time and heat release peak. The gel time of an anchorage agent is strongly influenced by accelerant and temperature. When DMT, DMA, and hydroquinone were added at the same temperature, the gelation time increased; with increasing ambient temperature, the gelation time of the anchorage agent decreased. The peak exothermic value of the curing reaction was less affected by the accelerator, and the peak exothermic value of the anchoring agent increased with the increase in ambient temperature. Then, the compressive strength of the anchorage agent, maintained at 20, 50, and 80°C for 1.5, 6, 12, and 24 h, was measured. We found that the compressive strength of resin anchorage agent decreased significantly with the increase in temperature, and the addition of DMT can improve the compressive strength of resin anchorage agent slightly at the same temperature conditions. Finally, through Fourier transform infrared scanning analysis, we determined the intrinsic causes of the influence of temperature and accelerator on the gelation time and compressive strength of the anchorage agent. Through SPSS fitting analysis, an empirical formula for predicting gelation time based on ambient temperature is proposed. Our findings provide a basis for reasonable mixing time and support design optimization of anchorage support in deep stratum in high-temperature geothermal environments.

1. Introduction

In mine roadways, bolt support is used for timely and active load bearing, which can significantly improve the self-supporting ability, and stability of the surrounding rock [1–3]. The resin anchorage agent is an important part of the bolt support system. These agents have the advantages of cure quickly at room temperature, high bonding strength, durability, and stability [4]. With increasing depths of coal mining, the average mining depth of most coal mines is about 650 m, and the formation temperature is 35.9–36.8°C. Some mines are now deeper than 1000 m, and the formation temperatures can be as high as 40–50°C. The spontaneous combustion of coal during coal mining also results in high-temperature geothermal environment [5–7]. The anchorage force on the bolt

support system is often lower than the designed value due to the high-temperature geothermal environment in deep stratum, thereby reducing the anchorage safety [8–10].

The anchorage agent commonly used for bolt support in coal mine roadways is composed of unsaturated polyester resin, curing agent, accelerator, and filler. Under the action of a curing agent, unsaturated polyester resin and monomers copolymerize to form bulk thermosetting polymer, as exemplified in Figure 1 [11]. Typical formulations are as follows: 100 copies of unsaturated polyester resin, 5 copies of curing agent, 1 part of accelerator, and 500–550 copies of stone powder. According to construction site requirements, the general anchoring agents are divided into four types: ultrafast, fast, medium, and slow speed according to gel time. Generally, the gel time of resin anchorage agent is adjusted using accelerants and curing agents.
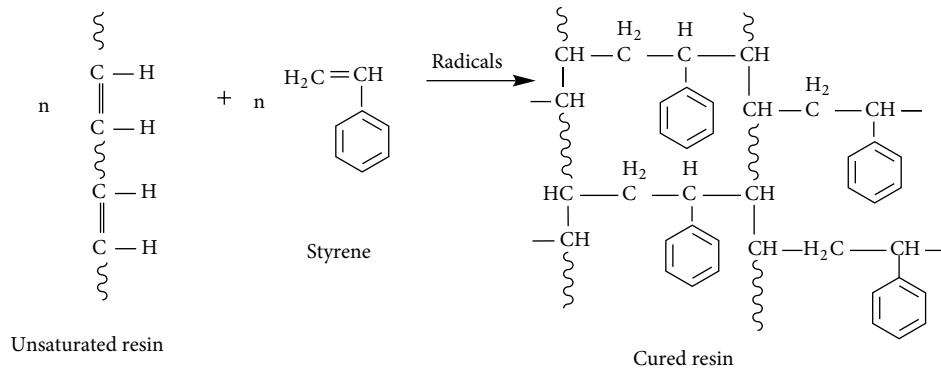
Figure 1: Anchoring agent curing reaction chemical equation.

According to China's MT 146.1-2011 standard [12], the gel time and mechanical properties of the anchorage agent are measured at $22 \pm 1°C$, and the high-temperature environment of deep mining is much higher than the standard temperature used when quantifying the properties of anchorage agents. Therefore, many scholars studied the influence of high-temperature geothermal environments on bolt support. Hu et al. [13] used the laboratory tests and numerical simulations to study the effect of temperature on the anchorage performance of resin bolts. Their conclusion was same as that obtained by Zhang et al. [14] at different temperatures: with increasing temperature, the anchorage force of resin bolt decreases. Wang et al. [15–16] studied the change in the gelation time of resin and resin anchorage agent at −10–30°C, finding that gelation time decreases significantly with increases in temperature. The maximum temperature studied was 30°C, which is not suitable for guiding deep high-temperature bolt support. Nan et al. [17] studied the effects of curing temperature and curing agent type on the compressive strength, flexural strength, and elastic modulus of bisphenol F epoxy concrete. The high temperature at greater depths and accelerant types considerably influence the gel time and mechanical properties of resin anchorage agents. Determining an accurate cementing time of an anchorage agent is important for the reasonable arrangement of construction mixing and pallet installation time. The change in the mechanical properties of anchorage agents directly impacts the anchorage effect and has a greater impact on the reliability of bolt support in deep strata. Therefore, it is important to study the effects of temperature and accelerant on the gel time and mechanical properties of resin anchorage.

Taking the commonly used PET (Polyethylene Terephthalate)-type unsaturated polyester resin anchorage agent as the research object, we systematically studied the effect of different temperatures and accelerant types on the gel time, the peak value of heat release, and the compressive strength of the resin anchorage, and explored the changing mechanism through Fourier transform infrared (FTIR) scanning. SPSS regression analysis was used to analyze the function relationship between gel time (t_{gel}) and environmental temperature (t) of different types of anchorage agents to provide scientific basis for safe and effective anchorage support systems in deep earth strata in high-temperature environments.

2. Materials

2.1. Resin.
Resin is one of the main components of anchorage agents. Unsaturated polyester resin is the least expensive and performs the best; therefore, it is widely used in the production of resin anchorage agents [18–20]. Among them, PET is a kind of unsaturated polyester resin, which has excellent mechanical properties, strong chemical stability, and low costs [21]. The chemical formula and properties of PET unsaturated polyester resin are shown in Figure 2 and Table 1.

2.2. Accelerator.
In this study, two accelerators, N,N-dimethylaniline (DMA) and N,N-dimethylp-toluidine (DMT), were used to accelerate the gelation of the anchorage agent. Their molecular formulas are shown in Figures 3 and 4, respectively. By adjusting DMA and DMT, different cementing speeds of anchorage agent can be prepared at a standard temperature. According to experience, the total dosage of DMA and DMT is 1% of the resin quality [22]. To achieve slow cementing of the anchorage agent, hydroquinone is usually added to the resin as an inhibitor. The amount of hydroquinone is usually added according to the time of cementing. In this study, 0.04% of the resin quality was added to the anchorage agent [23].

2.3. Curing Agent.
Unsaturated polyester resin is cured by radical-initiated polymerization, so it is necessary to use a redox initiator system. The curing agent (MeiYa Updated High-tech Material Industry Co., Ltd, Huainan, China) used in this study was a mixture of benzoyl peroxide (BPO), calcium carbonate, and ethylene glycol. The effective ingredient is benzoyl peroxide (BPO). Different contents of BPO change the gelling time of anchorage agent. In this experiment, a curing agent with 7% BPO content and 5% of the total weight of the anchoring agent cement was selected.

2.4. Aggregate.
In this test, the aggregate (MeiYa Updated High-tech Material Industry Co., Ltd, Huainan, China) of the resin anchorage agent was stone powder, and the main composition and particle size distribution of stone powder were selected as shown in Tables 2 and 3, respectively. Because wet aggregates destroy the bonding force between the binder and aggregate and reduce the strength of the anchorage agent, the aggregate must be dried to a water content of 0.1% or less water [24].
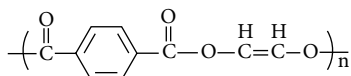
FIGURE 2: PET unsaturated polyester resin.

TABLE 1: Resin liquid index.

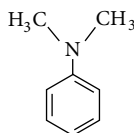| Type	Acid value (KOH mg/g)	Viscosity (25°C, mPa.s)	Heat distortion temperature (°C)
PET	10–20	550–650	50–55

FIGURE 3: N,N-Dimethylanilin (DMA).

3. Experimental Campaign

3.1. Test Apparatus

3.1.1. Anchorage Gel Time Test Facility.
To determine the gel time of the anchorage agent in different formation temperature environments, it was necessary to create a constant temperature environment with different formation temperatures. In this study, we reformed the DHG-9145A blast drying box (Yiheng Scientific Instrument Co., Ltd, Shanghai, China) to create this environment. The DHG-9145A type blast dryer is manufactured according to Chinese national standard GB/T 10586-2006 [25]. Its temperature control range is room temperature (RT) +10°C to 300°C, and its constant temperature fluctuation is ±1°C. The door of the blast drying box was removed here. The soft insulation, made of 4 mm thick Polyvinyl chloride (PVC) soft crystal board (commonly known as soft glass) and 15 mm thick rubber-plastic sponge, was bonded to the opening of the blast drying box with epoxy resin and adhesive tape, as shown in Figure 5(a). The soft insulation door (Figure 5(b)) was divided into three layers. The first and third layers are PVC soft crystal plates with rubber sponges in the middle. The three layers were bonded by epoxy and then fixed by bolts. The physical drawings of the reformed blast drying box are shown in Figure 5. The result was the creation of a constant temperature environment for the cementing test of anchorage agents, which was tested with an electronic digital thermometer, stopwatch, and electronic balance. The experimenters wore gloves of long barrel cloth, and their hands were inserted through holes in the soft heat insulation.

3.1.2. Anchorage Compressive Strength Test Equipment.
For the compressive strength test of the anchorage agent, we used a 101A-2 electric heating blast drying box to simulate the maintenance and growth of the anchorage agent in different temperature environments. We used a universal testing machine to conduct the compressive tests. Figures 6 and 7 show the universal testing machine and specimens for compressive strength test, respectively.
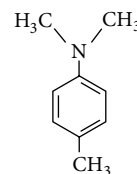

FIGURE 4: N,N-Ddimethylp-toluidine (DMT).

TABLE 2: Main components of stone powder.

Component	CaO	SiO$_2$	Al$_2$O$_3$	MgO	Fe$_2$O$_3$
Percentage (%)	57.7	25.9	5.6	2.5	0.6

3.2. Test Methods

3.2.1. Gel Time and the Peak of Heat Release Tests of Anchorage Agent.
The testing of the changing trend in the gel time of the resin anchorage under different temperatures and accelerators provides important reference information for reasonable mixing and tray installation time during the process of resin anchor installation. According to the Chinese coal industry standard MT146.1-2011 [12], the method used to measure the gel time of the resin anchorage agent is as follows: 100 g resin anchorage agent is placed in the center of the 150 mm polyester film; then the curing agent is fixed. Both are heated in a blast dryer for 20 min for the temperature to reach the test temperature and the test is verified using an electronic thermometer. Then, both hands are used to quickly and evenly mix the resin mortar and curing agent. Starting from the mixing resin paste, a stopwatch is used to record the gel time of the anchoring agent to the time when the cement thickens and the temperature begins to rise. The test block after the cementing of anchoring agent is shown in Figure 5(d). The measurement of the peak of heat release of resin anchorage agent was carried out after the gel time test and then the temperature of the test blocks was read to get its maximum value.

3.2.2. Compressive Strength Test of Anchorage Agent.
In the full-length anchorage support system, the anchorage agent acts as the bond between the bolt and the rock mass, and its own strength affects the stability of the anchorage. According to China Coal Industry Standard MT146.1-2011 [12], compressive strength test method involves using standard die to make 40 mm cubic blocks in groups of three, as shown in Figure 7. After cementing, the test block is immediately removed from the mold and maintained in a 101A-2 electric heating blast drying box at different temperatures. The compressive strength test is conducted on the universal material testing machine. To control the temperature change of the test block to ±3°C, only one piece is removed in each test, and then the compressive strength test is conducted immediately. The temperature of the test piece is simultaneously measured using a F8380 type infrared thermometer [26].

3.2.3. Test Scheme.
Four kinds of resin anchoring agent cements with different accelerator content were selected, and the resin anchoring agent cements were matched as shown in

TABLE 3: Screening table for stone powder particles.

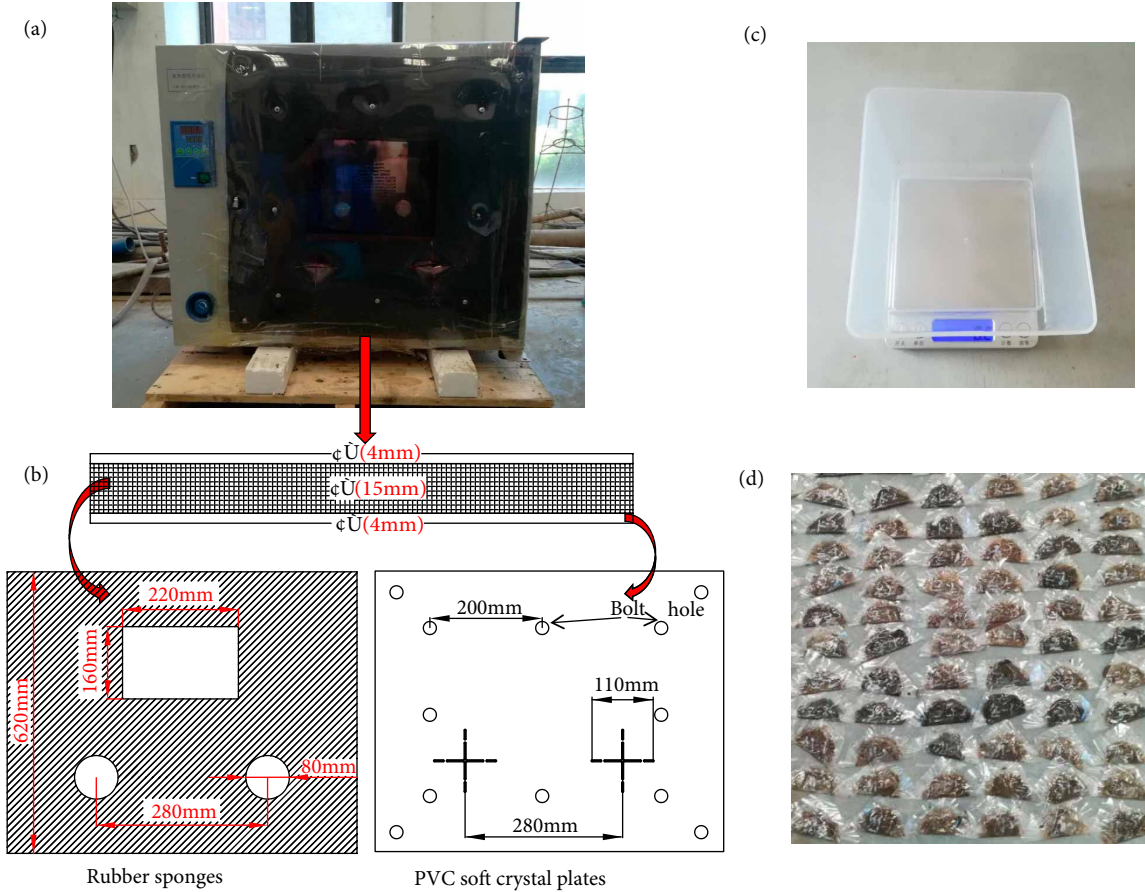| Type of stone powder	10–50 mesh	50–100 mesh	100–150 mesh	150–200 mesh	200–325 mesh
Coarse (%)	95.1	2.53	1.83	0.48	0.06
Fine (%)	10.7	17.2	10.6	44.1	17.4

FIGURE 5: Gel time test device for resin anchorage agent. (a) The photo of blast drying oven after transformation, (b) soft insulation door sectional view, (c) electronic balance, and (d) anchoring agent gel time test sample.

Table 4. In the test, the amount of curing agent was 5% of the quality of the resin anchoring agent cement. The gelation times of different types of resin anchorage were measured at 20, 30, 40, 50, 60, and 70°C. Secondly, the compressive strength of the anchorage agent maintained at 20, 50, and 80°C for 1.5 h, 6 h, 12 h, and 24 h was measured. To reduce the accidental error in the two tests, each group of tests was conducted three times and the average value was recorded.

TABLE 4: Proportion table of resin anchorage cement.

Type	PET	Stone power	Curing agent	DMA	DMT	Hydro-quinone
A	100	500	30	0.6	0.4	0
B	100	500	30	0.7	0.3	0
C	100	500	30	1	0	0
D	100	500	30	1	0	0.04

4. Experimental Results and Analysis

4.1. Effect of Temperature and Accelerant on Gelation Time of Resin Anchorage Agent.

Figure 8 depicts the influence of different accelerators on the cementing time of anchorage agent at standard temperature (20 ± 1°C). For the A resin anchoring agent, we added 0.6% DMA and 0.4% DMT with resin quality, the gel time was 48.7 s. We added 0.7% DMA and 0.3% DMT of the resin to the B-type resin anchorage, the gel time was 58.7 s. For the C-type resin anchorage, we only added DMA. Compared with the A-type anchorage agent, with the decrease in the DMA content, the gel time of the B and C-type anchorage agents was 20.5% and 69%, respectively. The adjustment of DMT content considerably affected the gel time change, whereas the amount of DMA had a relatively
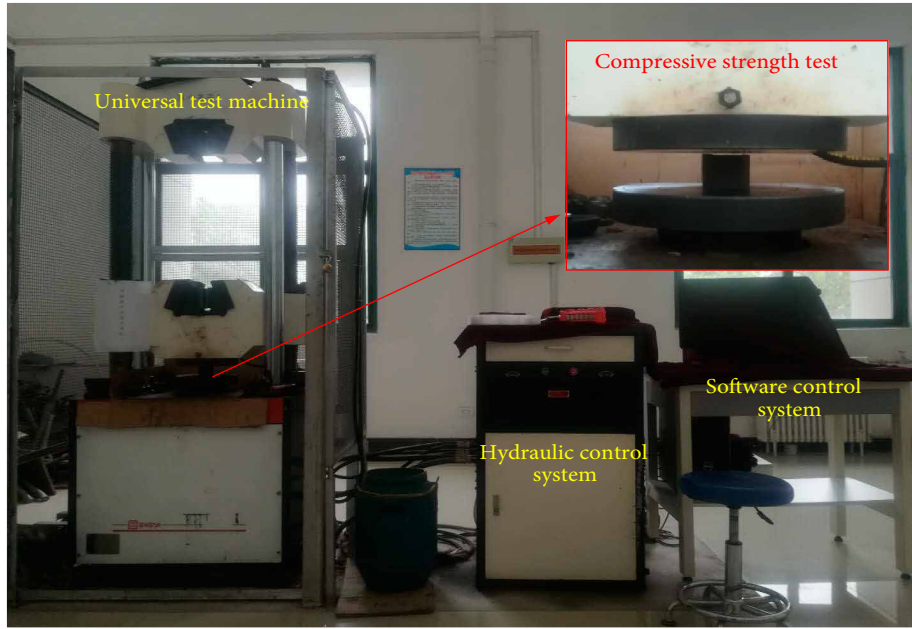
Figure 6: Diagram of compressive strength device used for testing the resin anchorage agent.
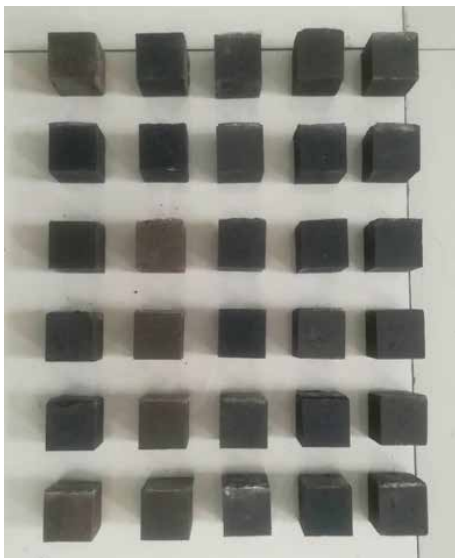

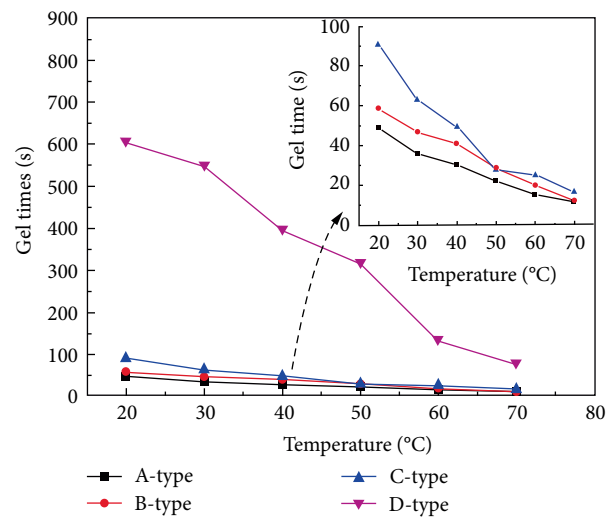Figure 7: Specimens for compressive strength test.

Figure 8: Gel time curve of resin anchorage at different temperatures.

stable effect on the gel time. By adding 0.03% inhibitor to D resin anchorage, the gel time increased to 605.6 s. The addition of a micro inhibitor can greatly delay the gelation time. The cementing time of the anchorage agent can be adjusted by adding different accelerating doses to meet the different field construction technology requirements.

Figure 8 also shows the effect of different temperatures on the gel time of anchorage agent. As the temperature of the abscissa increases, the gel time of different types of resin anchorage decreases. The gelation times of the A-, B-, and C-type anchorage agents at 70°C were 11.7 s, 12.3 s, and 16.6 s, respectively, which is 76.0%, 79.0%, and 81.6% lower than that

at $20 \pm 1°C$, respectively. The D-type anchorage agent is a slow anchorage agent. With the change in temperature, the gel time changes sharply. The gelation times were 547.6 s, 396.2 s, 315.2 s, and 132.9 s at temperatures of 30, 40, 50, and 60°C, respectively. The gelation time was 77.3 s at 70°C, which is 87.2% lower than that at the standard temperature (20 ± 1 °C). As a kind of polymer, the gelling rate of resin anchorage agent is strongly influenced by temperature. Generally, the growth in polymer crystals depends on the speed of the diffusion and regular stacking of the segments toward the nucleus. With the increase in temperature, the viscosity of the polymer decreases, the activity of the segments increases, and the rate of crystal growth increases, so the gel rate increases [27].
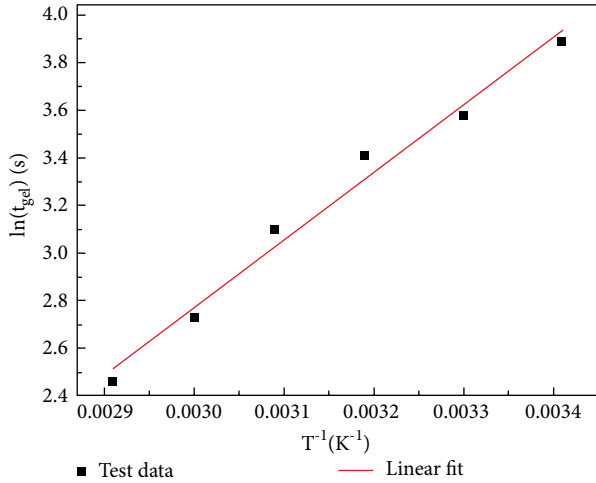
FIGURE 9: Arrhenius relationship of curing reaction of resin anchorage agent A.

TABLE 5: Activation energy of curing reaction for different types of resin anchors.

Resin type	A	B	C	D
Activation energies (kJ/mol)	25.16	29.19	31.50	43.02

FIGURE 10: Peak curves of exothermic reaction.

The gelation time of resin anchorage is dependent on the chemical reaction rate, and the rate of chemical reaction is related to the activation energy of the curing reaction. According to the Arrhenius equation, the relationship between gel time (t_{gel}) and curing reaction activation energy (E_a) is obtained [28]:

$$\ln(t_{gel}) = \frac{E_a}{RT} + B \tag{1}$$

where E_a is the activation energy of curing reaction, the molar gas constant R is 8.3144 J/(mol·K), T represents the thermodynamic temperature, t_{gel} is the gel time, and B is a constant term.

According to the experimental data of the anchorage gel time under different temperatures, a straight line about lnK ~ 1/T was obtained. The slope is the activation energy of the curing reaction. Taking the type A anchorage agent as an example, the Arrhenius relationship is shown in Figure 9.

The slope of the straight line in Figure 9 is 3026.566. From equation (1), the activation energy of curing reaction of the type A resin anchorage agent was calculated to be 25.16 kJ/mol. Similarly, the activation energy of curing reaction of several other anchorage agents can be calculated, as shown in Table 5.

The inference from the integral equation of the Arrhenius equation is that in the same temperature range, the smaller the activation energy, the smaller the reaction rate. Therefore, the gel time of the anchorage agent is least affected by temperature. From Table 5, the activation energy of the curing reaction of A, B, C, and D anchorage increases gradually. The longer the gel time of an anchorage agent, the greater the temperature. Anchorage cementing is a kind of polymerization reaction. The reaction rate has a limit, so the effect of the anchorage temperature on the faster the cementing rate is relatively small. Generally, the type and temperature of the accelerator have a large influence on the gelling time of the anchorage agent. According to the specific technical requirements and the influence of temperature and environment at the construction site, a suitable type of anchorage agent should be selected and the optimum mixing time of the anchorage agent should be determined.
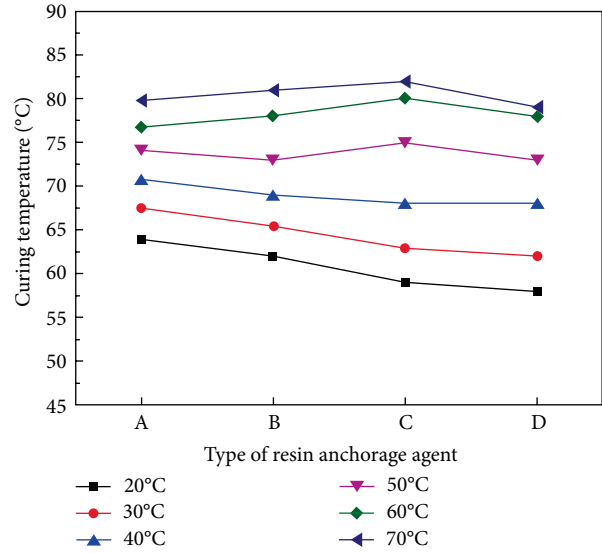
4.2. Influence of Temperature and Accelerant on the Peak of Heat Release of the Resin Anchorage Gel.

The exothermic peak is an important index in the polymer gelation reaction in addition to the gelation time. Figure 10 shows that the exothermic peak of different types of resin anchorage agent change little at the same temperature. Generally, the exothermic peak decreases slightly with increasing gelation time. Compared with type A, the exothermic peaks of the type D anchorage agent at 20°C and 30°C decreased by 9.38% and 8.28%, respectively. With the increase in the ambient temperature, the exothermic peak temperatures of different types of anchorage agent increase and the differences in the exothermic peak temperatures between different types decrease gradually.

For the same resin anchorage agent, the exothermic peak temperatures vary greatly under different temperature environments. The thermal peak values of A, B, C, and D resin anchorage agents increased by 24.69%, 30.65%, 38.98%, and 36.21% at 70°C, respectively. The curing exothermic peak of resin anchorage agent is less affected by the type of accelerator and more affected by environmental temperature.

4.3. Effect of Temperature and Accelerator on the Compressive Strength of Resin Anchor.

The test results of the compressive strength at different temperatures are shown in Figure 11. At 20°C, the compressive strength increases with the increase in curing time. Compared with the D-type anchorage agent, the A-, B-, and C-type anchorage agents have faster curing rates and faster increases in compressive strength. The 24-h
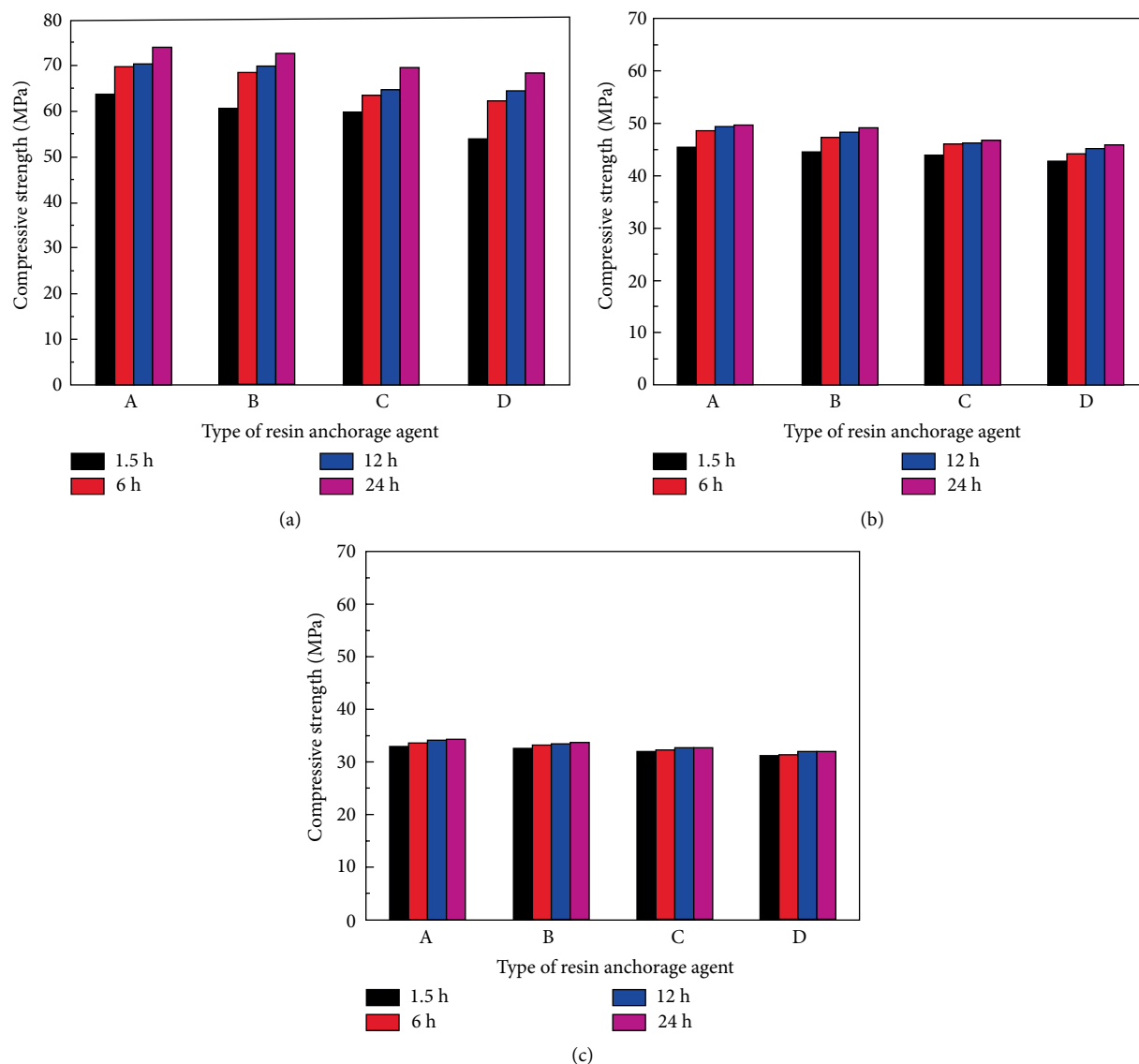
(a)

(b)

(c)

FIGURE 11: Column diagram of compressive strength of resin anchorage agent at different temperatures: (a) 20°C, (b) 50°C, and (c) 80°C.

compressive strengths of A-, B-, C-, and D-type anchorage agents are 73.75 MPa, 73 MPa, 69.38 MPa, and 68.5 MPa, respectively. The compressive strength of the anchorage agent improved slightly by adding accelerator DMT. The compressive strength of the type A anchorage agent increased by 5.93% compared with type C, to which only DMA was added. With the increase in temperature, the influence of the accelerator on the compressive strength of the anchorage agent weakened at 50°C and 80°C, and the growth rate of curing accelerated. In the 80°C environment, the anchorage agent reaches its maximum strength in 6–12 h. In addition, with the increase in temperature, the compressive strength of different types of resin anchorage agent decreased gradually. Taking the type A anchorage agent as an example, compared with 20°C, the compressive strength of the anchorage agent decreased by 32.88% and 53.38% at 50°C and 80°C, respectively. These results show that the effect of the accelerator on the compressive strength of the anchoring agent gradually decreases with the

increase in the ambient temperature, and the overall impact is small. The ambient temperature strongly influences the compressive strength of the anchoring agent. Therefore, when designing the anchorage support for deep high-temperature mining roadways, the influence of the formation temperature on compressive strength should be considered, and the support parameters should be rationally optimized.

5. FTIR Scanning Analysis

The curing products of type A and C resin anchoring agents at 20°C, 40°C, 60°C, and 70°C were selected and analyzed using a Nicolet 460 infrared spectroscope (Nicolet Instrument Corporation Madison, WI, USA). The FTIR spectra of the reaction products are shown in Figure 12. The stretching vibrations of hydroxyl O–H, C–H and carbonyl C=O are at $3420\,cm^{-1}$, 2870^{-1}, and $1790\,cm^{-1}$, respectively, while the

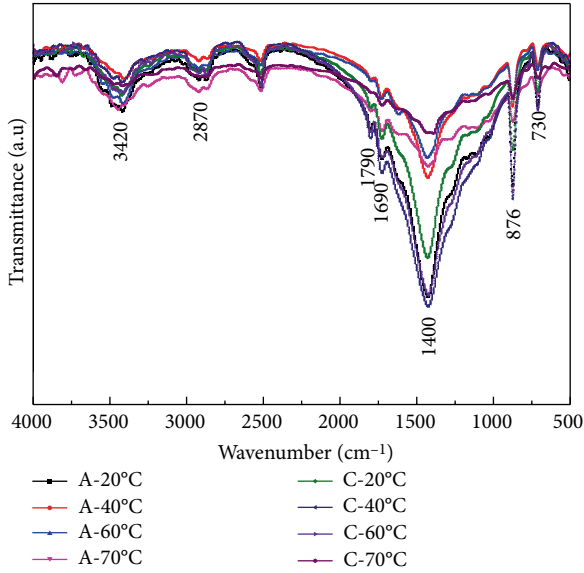Figure 12: Fourier transform infrared (FTIR) scanning analysis of anchorage at different temperatures.

Table 6: Gelation time of the anchorage of different types of resin in different temperature environments.

Environment temperature (°C)	A (s)	B (s)	C (s)	D (s)
20	48.7	58.7	90.3	605.6
30	35.7	46.8	62.9	547.6
40	30.2	41.1	49.2	396.2
50	22.1	28.7	27.8	315.2
60	15.3	20.1	25.0	132.9
70	11.7	12.3	16.6	77.3

resin in different temperature environments in the testing results is as shown in Table 6.

From Table 6, it can be seen that different types of resin anchorage agents have different change rates of gelation time at different temperatures. As shown in Figure 13, by comparing linear function, logarithmic function, exponential function, power function, and quadratic polynomial of curve fitting coefficient, the quadratic polynomial was used to describe the relationship between gelation time and temperature of resin anchoring agent.

The functional relations between gel time (t_{gel}) and temperature (t) of A, B, C, and D types were shown in (2), (3), (4), and (5), respectively.

$$A \text{ type} : t_{gel} = 72.917 - 1.398t + 0.007t^2 \tag{2}$$

$$B \text{ type} : t_{gel} = 79.093 - 1.07t + 0.002t^2 \tag{3}$$

$$C \text{ type} : t_{gel} = 152.949 - 3.666t + 0.025t^2 \tag{4}$$

$$D \text{ type} : t_{gel} = 821.249 - 0.954t - 0.02t^2 \tag{5}$$

Through the above research, we found that the gel time of the resin anchorage agent can be calculated under known formation temperature, and a reasonable mixing time and time of pallet installation can be determined for use during the construction of the anchoring process to avoid excessive agitation in anchorage support to reduce anchorage force. The testing confirmed that the compressive strength of the anchorage agent itself decreases with the increase in ambient temperature, and the ultimate bearing capacity of the anchorage agent usually decreases. To improve the reliability of the bolt support system in high-temperature geothermal environment, the strength of bolt support is usually increased by increasing the length and support density of the bolt support [30]. However, when the local temperature of the anchorage agent is too high, the compressive strength of the PET resin anchorage agent decreases too much, which could easily cause support failure. Given this situation, we developed a new type of anchorage agent, anchorage agent l, based on the existing PET anchorage agent mixed with FX-470 resin to modify the mixing of PET and KH-570, and obtained a resin anchorage agent with high strength and excellent heat resistance to solve the problem of anchorage loss in high-temperature ground [31].

stretching vibration of the unsaturated double bond C=C in polyester is at $1690\,\text{cm}^{-1}$, and the peak at $1400\,\text{cm}^{-1}$ can be ascribed to the symmetric stretching vibration of ethereal groups C–O–C. The peaks at $876\,\text{cm}^{-1}$ and $730\,\text{cm}^{-1}$ are derived from C–H group in benzene ring of p-phenyl-type [29].

Comparing the FTIR spectra of cured products of type A and C, it can be seen that the functional groups of the products of resin anchorage polymerization under different temperatures and accelerators are the same, and no new functional groups are produced. The polymerization reaction occurs between the unsaturated polyester resin and styrene in the resin anchorage. With the increase in crosslinking degree of the polymer products, the number of C–H on the saturated alkyl group at $2870\,\text{cm}^{-1}$ in the polymer will increase. The ratio of the number of C–H at $2870\,\text{cm}^{-1}$ to that of ethereal group at $1400\,\text{cm}^{-1}$ in type A anchorage agent is larger than that of type C anchorage agent. It can be seen that the crosslinking degree of cured products of type A anchorage agent is relatively high. Therefore, the addition of accelerator DMT increases both the curing rate and the degree of polymerization of resin anchorage agent. This conclusion reveals the intrinsic reason why the addition of DMT in the compressive strength test of resin anchorage agent can improve the compressive strength of anchorage agent by a small margin.

6. Regression Analysis of Gel Time Law of Anchorage Agent

To better guide field production practice, statistical analysis software SPSS (IBM, NY, USA) was used to complete the regression analysis on the gel time test data. Taking temperature as an independent variable, the functional relationship between gel time and the independent variables of the resin anchoring agent with different accelerant contents was determined. Gelation time of the anchorage of different types of
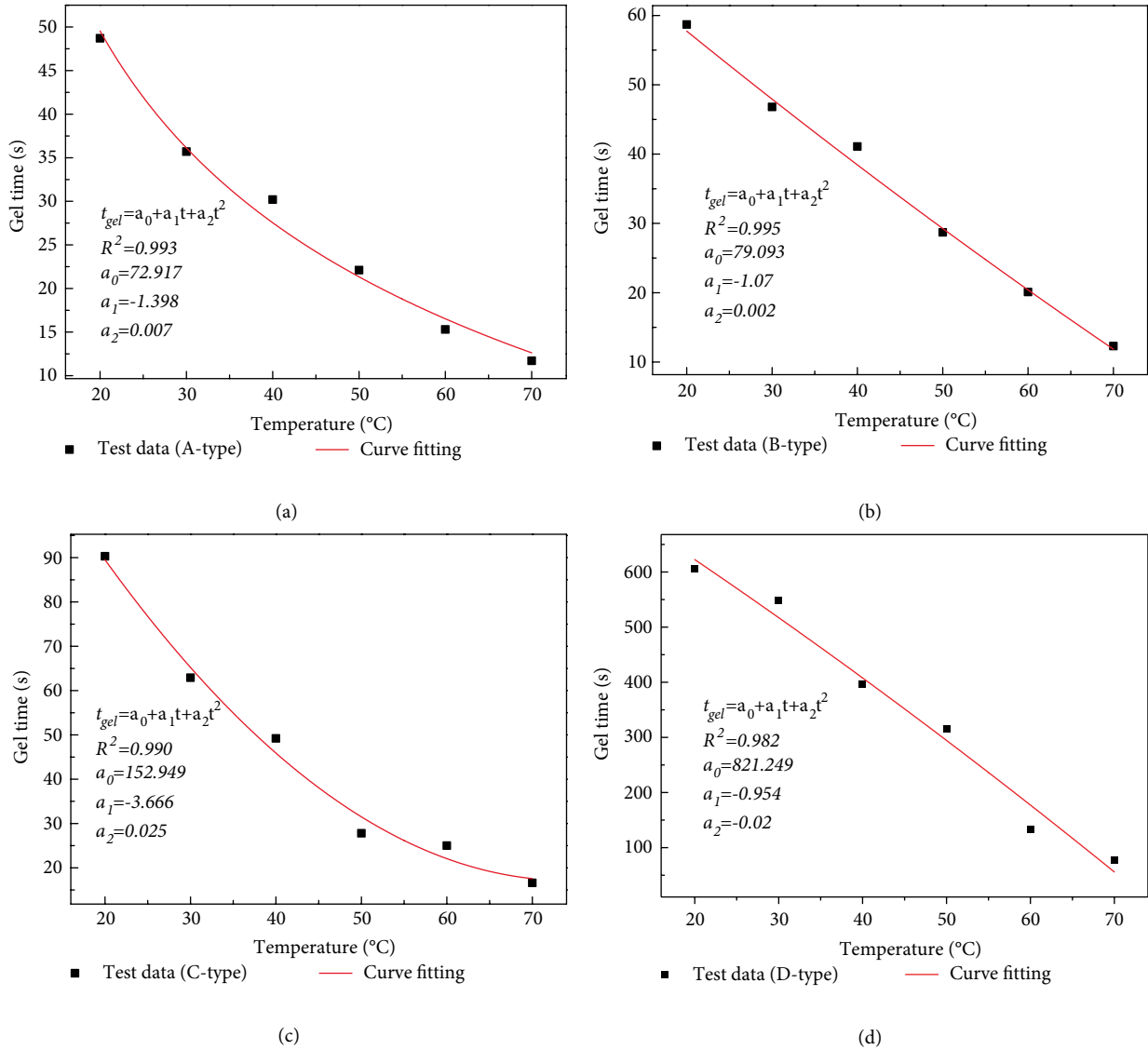
FIGURE 13: The regression function curve of the relationship between gelation time and temperature: (a) A-type, (b) B-type, (c) C-type, and (d) D-type.

7. Conclusions

The effects of different temperatures and accelerators on gelation time and compressive strength of PET resin anchorage were studied. The results are summarized as follows:

(1) Through the cementing time test of the anchorage agents, we found that the accelerator DMT is more active than DMA, and the trace hydroquinone inhibitor has a strong influence on the gel time. The environmental temperature of 20–70°C was simulated using a designed test chamber, and the gelation time of the anchorage decreased with the increase in ambient temperature. According to the gel time and environmental temperature test data, the activation energies of curing reactions of the A–D anchorages were deduced to be 25.16 kJ/mol, 29.19 kJ/mol, 31.50 kJ/mol, and 43.02 kJ/mol, respectively.

(2) Different accelerators have little effect on the peak value of the heat release of the resin anchorage. The faster the gel speed at the same temperature, the greater the exothermic peak. With the increase in ambient temperature, the peak value of the curing heat release for all kinds of resin anchorage increases. The curing products of the anchorage agent at different temperatures and accelerators were analyzed by FTIR scanning, and the internal causes of the changes in gelation time and exothermic peak value were revealed at the micro level.

(3) Compressive strength tests under different temperature environments showed that the type of accelerator has little influence on the compressive strength of the anchorage agent. Compared with the C-type anchorage agent, the compressive strength of the A-type anchorage agent increases by 5.93% when adding DMT, whereas the temperature change has a

greater impact on the compressive strength of anchorage agent, which decreased by 35.36% and 50.14% at 50°C and 80°C, respectively.

(4) Regression analysis based on the experimental data of the gel time and temperatures of different types of resin anchorages, completed using SPSS analysis software, showed that the relationship between gel time and ambient temperature obeys the quadratic polynomial function, providing a basis for determining reasonable mixing and tray installation time.

Data Availability

The data used to support the findings of this study are available from the corresponding author upon request.

Conflicts of Interest

The authors declare that they have no conflicts of interest.

Authors' Contributions

Conceptualization, Xiaohu Liu and Zhishu Yao; Formal analysis, Weipei Xue; Methodology, Xiaohu Liu; Resources, Xiang Li; Writing—original draft, Xiaohu Liu.

Acknowledgments

References

[1] H. Kang, "Sixty years development and prospects of rock bolting technology for underground coal mine roadways in China," *Journal of China University of Mining & Technology*, vol. 45, no. 6, pp. 1071–1081, 2016.

[2] B. Navid and H. John, "Explicit reinforcement models for fully-grouted rebar rock bolts," *Journal of Rock Mechanics and Geotechnical Engineering*, vol. 9, no. 2, pp. 267–280, 2017.

[3] K. Zhang, G. Zhang, R. Hou, Y. Wu, and H. Zhou, "Stress evolution in roadway rock bolts during mining in a fully mechanized longwall face, and an evaluation of rock bolt support design," *Rock Mechanics and Rock Engineering*, vol. 48, no. 1, pp. 333–344, 2015.

[4] J.Y. Lv, "The appliance of resin anchor in mine," *Waterpower Excavating Coal and Pipeline Transport*, vol. 3, pp. 33–36, 1996.

[5] W. J. Yao and J. Y. Pang, "The status and progress of the research on thermal environment of deep mine in China," *Mining Safety & Environmental Protection*, vol. 45, no. 1, pp. 107–111, 2018.

[6] H. Lan, D. K. Chen, and D. B. Mao, "Current status of deep mining and disaster prevention in China," *Coal Science and Technology*, vol. 44, no. 1, pp. 39–46, 2016.

[7] Y. Lu, "Laboratory study on the rising temperature of spontaneous combustion in coal stockpiles and a paste foam suppression technique," *Energy & Fuels*, vol. 31, no. 7, pp. 7290–7298, 2017.

[8] S. Xue-gui, D. Xian-jie, Y. Hong-hu, and L. Ben-kui, "Research of the thermal stability of structure of resin anchoring material based on 3D CT," *International Journal of Adhesion & Adhesives*, vol. 68, pp. 161–168, 2016.

[9] C. H. Kang, "Study on the influence of temperature on the mechanical properties of resin anchor," *AnHui University of Science and Technology*, 2017.

[10] Y. Lu, S. Shi, H. Wang, Z. Tian, Q. Ye, and H. Niu, "Thermal characteristics of cement microparticle-stabilized aqueous foam for sealing high-temperature mining fractures," *International Journal of Heat and Mass Transfer*, vol. 131, pp. 594–603, 2019.

[11] C. Y. Zheng and N. J. Huang, *Resin Anchor and Anchoring Agent*, China Coal Industry Publishing Home, 1983.

[12] China Standards Publication, *Resin Anchor Bolts-Part 1: Capsules, MT 146.1-2011*, Standard Press of China, Beijing China, 2011.

[13] B. Hu, H. P. Kang, J. Lin, J.-F. Cai, and P.-F. Jiang, "Study on influence of temperature on anchorage performance of resin anchored bolt," *Journal of Mining & Safety Engineering*, vol. 29, no. 5, pp. 644–649, 2012.

[14] S. Zhang, P. F. Gou, and H. Fan, "Influence of water and temperature on resin anchor-hold," *Journal of Southeast University (Natural Science Edition)*, vol. 35, no. 1, pp. 50–54, 2005.

[15] J.-Y. Wang, J.-M. Guo, J.-F. Mi, Y. Zhang, and A.-R Shi, "Influence of the temperature on the gel time of the capsules in rock bolting system," *Journal of China Coal Society*, vol. 33, no. 6, pp. 619–622, 2008.

[16] J.-Y. Wang, "Quantity of accelerant affected to gel time of anchoring agent for resin bolt," *Coal Science and Technology*, vol. 36, no. 11, pp. 23–25, 2008.

[17] J. J. Nan, Y. Jaeheum, S. Inbae, and Y. Kyu-Seok, "Effects of curing temperature and hardener type on the mechanical properties of bisphenol F-type epoxy resin concrete," *Construction and Building Materials*, vol. 156, pp. 933–943, 2017.

[18] Z. R. Wang, "Resin anchoring agent," *Chemical Building Materials*, vol. 1, pp. 24–27, 2001.

[19] S. M. Wang, Z. J. Zhu, and X. H. Lu, "Synthesis and application of unsaturated polyester resin for glycerol modified anchoring agent," *China High-Tech*, vol. 1, no. 4, pp. 14–16, 2017.

[20] J. Zhao, "Talking about the factors affecting the reduction of anchorage force of coal mine underground bolt," *Scientific Management*, vol. 10, pp. 260–261, 2017.

[21] Z. Y. Hu and S. M. Wang, "Systematic study on influencing factors of main performance indexes of resin anchoring agent," *Science and Technology Economic Guide*, vol. 19, pp. 78–79, 2017.

[22] X. H. Lu, "Development of quick repairing clay," *Science and Technology Economic Guide*, vol. 19, pp. 81–82, 2017.

[23] F. F. Liu, X. H. Yuan, and Q. N. Feng, "Study on a curing system of unsaturated polyester resin," *Fiber Reinforced Plastics/ Composites*, vol. 3, pp. 70–73, 2015.

[24] O. Elalaoui, E. Ghorbel, V. Mignot, and O. M. Ben, "Mechanical and physical properties of epoxy polymer concrete after exposure to temperatures up to 250°C," *Construction and Building Materials*, vol. 27, no. 1, pp. 415–424, 2012.

[25] China Standards Publication, *Specification for Damp Heat test chambers, GB/T 10586–2006*, Standard Press of China, Beijing, China, 2006.

[26] Y. Lu, S. Shi, F. Yang, T. Zhang, H. Niu, and T. Wang, "Mo-doping for improving the ZrF_4 coated-Li[$Li_{0.20}Mn_{0.54}Ni_{0.13}Co_{0.13}$]$O_2$ as high performance cathode materials in lithium-ion batteries," *Journal of Alloys and Compounds*, vol. 767, pp. 23–33, 2018.

[27] N. Naofumi, M. Ryo, K. Shuntaro et al., "Synthesis of joint-linker type gels and porous polymers by addition reactions of multi-functional thiol and alkyl diacrylate, diisocyanate compounds," *Materials Today Communications*, vol. 18, pp. 153–162, 2019.

[28] D.-B. Guan, Z.-Y. Cai, X.-C. Liu et al., "Rheological study on the cure kinetics of two-component addition cured silicone rubber," *Chinese Journal of Polymer Science*, vol. 34, no. 10, pp. 1290–1300, 2016.

[29] J. X. Zhou and B. X. Dong, "A study on the infra-red spectrometry of unsaturated polyesters," *Thermosetting Resin*, vol. 18, no. 4, pp. 22–24, 2003.

[30] M. Zhao, "Study on impact of anchorage length on anchorage effect," *China University of Mining and Technology*, 2016.

[31] X. Liu, Z. Yao, W. Xue, and X. Li, "Development, performance, and microscopic analysis of new anchorage agent with heat resistance, high strength, and full length," *Advances in Materials Science and Engineering*, vol. 2019, Article ID 4239486, 9 pages, 2019.